Volume 50
Number 7
7 April 2021
Pages 4223–4792

Chem Soc Rev

Chemical Society Reviews

rsc.li/chem-soc-rev

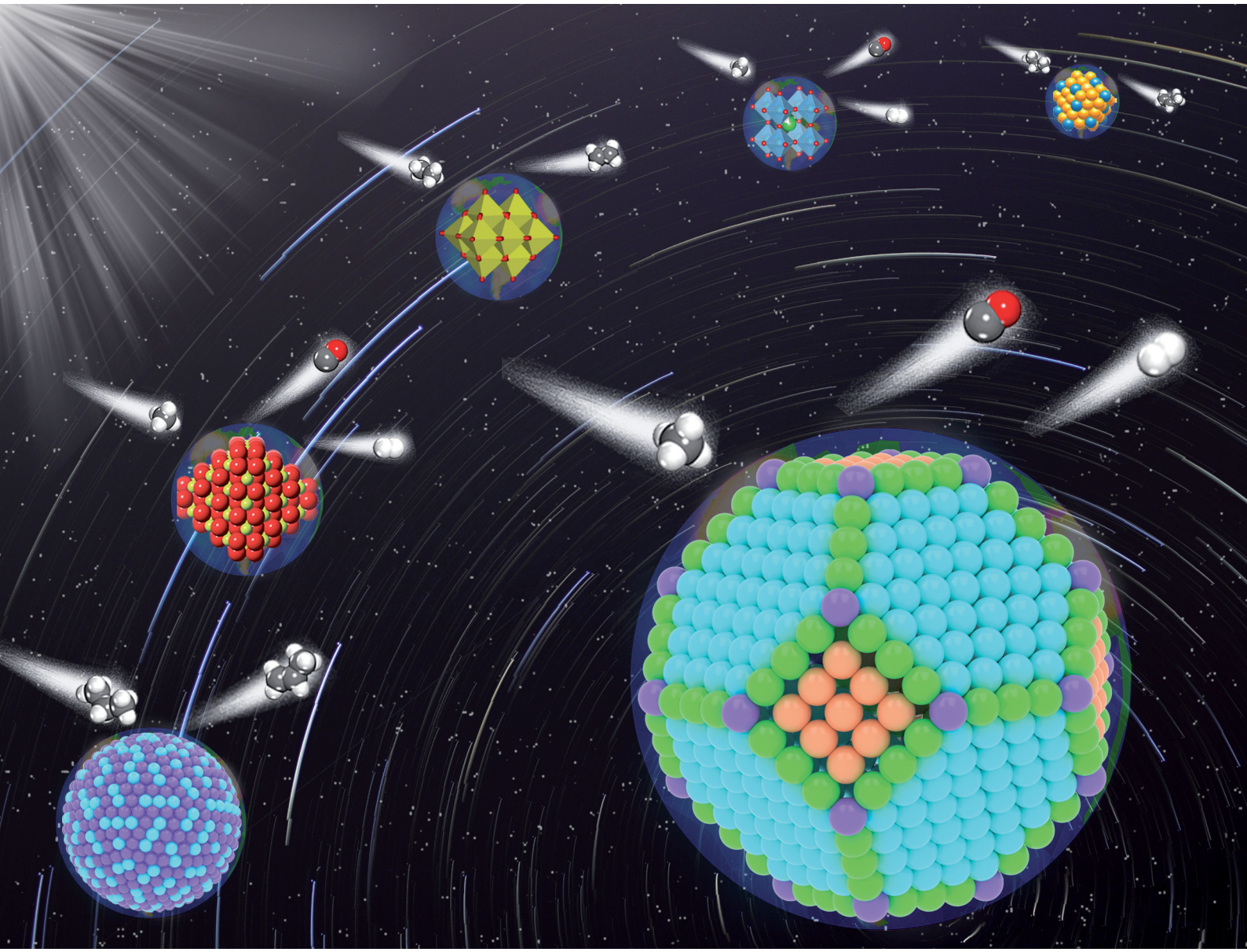

ISSN 0306-0012

ROYAL SOCIETY OF CHEMISTRY

REVIEW ARTICLE

Yi-An Zhu, De Chen *et al.*

C–H bond activation in light alkanes: a theoretical perspective

Chem Soc Rev

REVIEW ARTICLE

View Article Online
View Journal | View Issue

Cite this: *Chem. Soc. Rev.*, 2021, **50**, 4299

C–H bond activation in light alkanes: a theoretical perspective

Yalan Wang,[a] Ping Hu,[b] Jia Yang,[a] Yi-An Zhu *[b] and De Chen *[a]

Alkanes are the major constituents of natural gas and crude oil, the feedstocks for the chemical industry. The efficient and selective activation of C–H bonds can convert abundant and low-cost hydrocarbon feedstocks into value-added products. Due to the increasing global demand for light alkenes and their corresponding polymers as well as synthesis gas and hydrogen production, C–H bond activation of light alkanes has attracted widespread attention. A theoretical understanding of C–H bond activation in light hydrocarbons *via* density functional theory (DFT) and microkinetic modeling provides a feasible approach to gain insight into the process and guidelines for designing more efficient catalysts to promote light alkane transformation. This review describes the recent progress in computational catalysis that has addressed the C–H bond activation of light alkanes. We start with direct and oxidative C–H bond activation of methane, with emphasis placed on kinetic and mechanistic insights obtained from DFT assisted microkinetic analysis into steam and dry reforming, and the partial oxidation dependence on metal/oxide surfaces and nanoparticle size. Direct and oxidative activation of the C–H bond of ethane and propane on various metal and oxide surfaces are subsequently reviewed, including the elucidation of active sites, intriguing mechanisms, microkinetic modeling, and electronic features of the ethane and propane conversion processes with a focus on suppressing the side reaction and coke formation. The main target of this review is to give fundamental insight into C–H bond activation of light alkanes, which can provide useful guidance for the optimization of catalysts in future research.

Received 1st October 2020

DOI: 10.1039/d0cs01262a

rsc.li/chem-soc-rev

1. Introduction

Alkanes or paraffins (C_nH_{2n+2}) are acyclic saturated hydrocarbons and are the major constituents of natural gas and crude oil. Alkanes have the simplest structure among organic

[a] *Department of Chemical Engineering, Norwegian University of Science and Technology, Trondheim, 7491, Norway. E-mail: de.chen@ntnu.no*
[b] *UNILAB, State Key Laboratory of Chemical Engineering, School of Chemical Engineering, East China University of Science and Technology, Shanghai, 200237, China. E-mail: yanzhu@ecust.edu.cn*

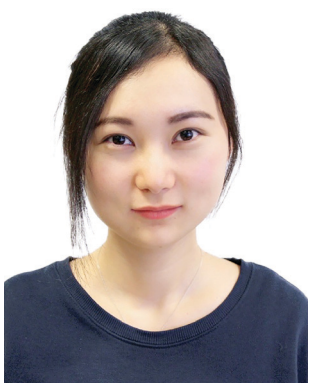

Yalan Wang

Yalan Wang obtained her bachelor's degree (2011) and master's degree (2014) from East China University of Science and Technology (ECUST). She received her PhD from the Norwegian University of Science and Technology (NTNU) in 2019, where she is currently working as a postdoctoral fellow. Her main research interests include methane activation, CO hydrogenation, electrochemical CO_2 reduction, and redox reaction cycles. She has strong expertise in density functional theory calculations and descriptor-based microkinetic modeling for rational design of catalysts in heterogenous catalysis.

Ping Hu

Ping Hu is currently a PhD student in the School of Chemical Engineering at East China University of Science and Technology (ECUST). She studied Chemical Engineering at Shanghai Normal University (SHNU) and graduated with an MSc in 2015. Her current research interest is to combine density functional theory calculations and microkinetic analysis to examine the kinetics of propane dehydrogenation and search for better catalysts.

molecules, where each carbon atom is sp^3-hybridized with four sigma bonds (either C–C or C–H), and each hydrogen atom joins to one of the carbon atoms (in a C–H bond). The efficient and selective activation of C–H bonds can directly convert abundant and low-cost hydrocarbon feedstocks into value-added products as commodity, intermediate, and fine chemicals, which have the potential to have a substantial economic impact. However, there is a formidable challenge for the sufficient activation of C–H bonds in alkanes into more sophisticated value-added architectures due to the thermodynamically strong C–H bonds and thus a high energy barrier to break the bonds. The bond strength of C–H bonds depends slightly on the structure, and the bond dissociation energies (BDEs) of the primary (1°), secondary (2°), and tertiary (3°) C sp^3–H bonds of alkanes fall in the range of 4.16 to 4.38 eV, with the 1° C–H bonds being stronger than the 2° and 3° bonds.[1] Methane molecules, as the main constituent of natural gas, have four primary C–H bonds which are highly stable and thus are the most difficult to activate. Moreover, the C–H bonds of alkanes functionalized products (such as alkenes and oxygenates) are not as stable as alkanes, which presents a challenge for gaining a high selectivity in alkane conversions.

Catalysts play a privileged role in selective C–H bond activation and controlling the reaction pathways to improve the selectivity and lower the carbon footprint. Many catalytic routes have been developed to convert alkanes to high value-added chemicals, which form the technological foundation of the modern chemical industry and meet the demand of certain substances in a transition from petroleum to natural gas and shale gas and liquids. The global demand for light alkenes has increased due to the increasing demand of their corresponding polymers. The light olefin market across the globe is expected to reach USD 475.8 million at a compound annual growth rate of 5.85% by the end of 2027. Besides, with a shift of the feedstock from naphtha to natural gas feedstocks, the supply of certain chemicals such as propylene, butadiene, and BTX has become constrained. Their shortage in the market is the main driving force for the renewed interest in producing them from alkanes, as low-cost feedstocks for chemical production. Synthesis gas and hydrogen production *via* steam reforming, dry reforming, and partial oxidation from methane, and dehydrogenation reactions have been often used by industry for the on-purpose production of hydrogen and light alkenes like ethylene, propylene, and butylene. Catalytic dehydrogenation of light alkanes is becoming increasingly important with the exploitation of shale gas, which provides a significant amount of ethane and propane feedstocks. The dehydrogenation is one of the major routes to fill the lower olefin gap in terms of future production and demands.

Jia Yang

Jia Yang (born in 1983) is associate professor in the Department of Chemical Engineering, Norwegian University of Science and Technology (NTNU). She received her PhD in Heterogeneous Catalysts from NTNU in 2011. She carried out postdoctoral research in the same field and then worked as a research scientist in SINTEF for three years before joining the Department in 2016. Her main research interests include Fischer–Tropsch synthesis, biomass conversion to fuels and chemicals, electrochemical CO_2 reduction, fuel cell catalysts, and photocatalytic H_2 generation. She has strong expertise in mechanistic investigation with Steady-State Isotopic Transient Kinetic Analysis (SSITKA) and isotopically labelled gases.

Yi-An Zhu

Yi-An Zhu received his PhD from East China University of Science and Technology (ECUST) in 2007, where he is now Professor of Chemical Engineering. His research interest is focused on the kinetics and mechanisms of heterogeneous catalytic reactions over solid-state catalysts. His current research projects include descriptor-based microkinetic analysis combined with results from density functional theory calculations for rational catalyst design and molecular simulations based on classical and reactive force fields for determination of structures of complex solids.

De Chen

De Chen (born in 1962) has been a Full Professor in catalysis in the Department of Chemical Engineering, Norwegian University of Science and Technology (NTNU), since 2001. He holds a PhD in industrial catalysis at NTNU (1998). His scientific activity is mainly devoted to mechanistic and kinetic studies of heterogenous catalysis, multiscale modeling of catalytic processes for the conversion of various resources such as natural gas, biomass and plastic waste, and CO_2 capture technologies. He developed new research methods to study dynamic redox reaction cycles in industrial catalytic processes by combining first-principles calculation and operando kinetic study.

Catalytic dehydrogenation reaction is an endothermic reaction, and high equilibrium conversion is favored by high temperature and low alkane pressure.[2] However, hydrogenolysis also occurs at the high temperature, forming methane and other lower carbon number species leading to low olefin selectivity. Both transition metals (TMs) and metal oxides are active for the dehydrogenation of light alkanes. Oxidative dehydrogenation (ODH) is an alternative process to break down the thermodynamic limitation. The main challenge is to control the consecutive oxidation of alkanes/alkenes to carbon oxides due to the much higher reactivity of products than the reactants. The critical issue in the development of catalysts is, therefore, how to selectively activate the C–H bonds of alkane molecules.[3]

During the last few decades, great progress has been made in developing catalysts and catalytic processes of alkane conversion to value-added chemicals. Amounts of reviews have been reported for homogeneous catalysis regarding C–H bond activation of alkanes on organometallic and/or inorganic complexes,[4–10] which are not covered in this review. In contrast, we focus on heterogeneous catalysis. So far, many comprehensive reviews on methane conversion[11–13] and ethane and propane conversion on metal,[2,14] oxide,[2,3,15–18] metal-free,[19,20] and bifunctional catalysts[21] have been reported towards heterogeneous systems, covered mainly catalysts,[2,12,17,21,22] kinetics,[3,15] and processes.[2,17] These reviews deal with progress in the experimental studies of chemistry and catalysis, focusing on key challenges related to light alkane activation in terms of activity, selectivity, and carbon formation. Despite their successful applications at an industrial scale, several central questions remain unanswered, such as active sites effectively activating C–H bonds, the detailed reaction mechanism of catalytic cycles, rate-determining steps (RDSs), and factors governing the selectivity and carbon formation in activation and conversion processes of methane and light alkanes.

A better understanding of the factors governing the fundamental aspects mentioned above is important to design more efficient catalyst systems to promote selective C–H activation. The design of new effective catalysts and/or improvement of industrial catalysts rely on a better understanding of the surface reactions at a molecular level. Great efforts have been devoted to assessing the structure–property–performance relationship. However, it is still challenging because the experimental approach can severely restrict the range of catalyst structures and compositions to be examined. An effective strategy for developing useful catalysts should involve simultaneous consideration of all structure–function relationships that are related to stability, activity, and selectivity in the design of catalyst and reaction systems.[23]

Theoretical heterogeneous catalysis and surface science have witnessed significant development toward a molecular-level understanding of the working catalysts. Electronic structure calculations based primarily on *ab initio* density functional theory (DFT) calculations have been widely applied in heterogeneous catalysis.[24] Over the past decade, DFT combined with microkinetic modeling is widely used to provide vital fundamental data regarding the properties of the active sites, mechanisms of surface reactions, RDSs, trends in reactivity, *etc.*[25–28] The development and application of DFT in heterogeneous catalysis[29,30] as well as microkinetic modeling for catalyst design[31,32] have been reported in several excellent reviews. Generally, microkinetic models are constructed based on DFT estimated energetics of elementary steps involved in reaction mechanisms for targeted reactions. Particularly, in recent years, the rapidly developed scaling relationships[27,33–36] make the combination of microkinetic modeling with DFT more convenient due to much addressed computational complexity. That is, based on the DFT calculated energetics, the scaling relationships are obtained and used to predict the energetics of other adsorbates or on other catalyst surfaces, which are further employed as input parameters of the microkinetic model. DFT calculations have shown that the energetics of crucial reaction intermediates are linked by linear scaling relationships that have been applied for rationalizing trends in C–H bond activation of light alkanes across different catalyst surfaces. Gong and coworkers[29] reviewed the mechanistic insights into heterogeneous catalytic dehydrogenation of light alkanes obtained from DFT calculations in 2015. Owing to the rapid development of scaling relationship-based microkinetic modeling, the molecular level understanding of surface catalyzed reactions involved in C–H activation of light alkanes has been dramatically improved across metal, alloy, oxide, and metal–oxide hybrid catalysts. A comprehensive review of the theoretical heterogeneous catalysis of C–H activation of methane, ethane, and propane on various catalysts is highly desired to provide fundamental insights into industrial catalytic processes and guidelines for the rational design of new catalysts and/or improvement of industrial catalysts.

The purpose of this review is to describe the recent progress in computational catalysis that has addressed the C–H bond activation of light alkanes, such as methane, ethane, and propane by heterogeneous transition metal, oxide, and metal/oxide catalysts, with emphasis on activity, selectivity and coke formation in light alkane conversion. This review describes the detailed understanding of kinetic and mechanistic insights into catalytic dehydrogenation of light alkanes at atomic and molecular levels obtained from DFT calculations and microkinetic modeling across various catalyst surfaces. It unravels the basic electronic features of the C–H cleavage process to the targeted products. The results of the mechanistic studies depend on temperature, pressure, and reactant composition. Finally, the design of new catalysts and improvement of the catalysts are reviewed and proposed based on the fundamental understanding and theory-driven catalyst design.

The first part of the review addresses direct and oxidative C–H bond activation of methane *via* σ–d interaction on metals and oxides. The mechanistic insights obtained from DFT assisted microkinetic analysis into steam and dry reforming, and the partial oxidation dependence on metal/oxide surfaces and nanoparticle (NP) size are summarized and analyzed. The theory-driven catalyst design is reviewed and discussed. The second and third parts describe direct and oxidative activation

of the C–H bonds of ethane and propane towards light alkene formation on various metal and oxide surfaces. The emphasis is on the elucidation of active sites, intriguing mechanisms, microkinetic modeling, and electronic features of the ethane and propane conversion processes with a focus on suppressing the side reaction and coke formation.

2. C–H bond activation in methane

Methane is the simplest hydrocarbon, which is the predominant constituent (approximately 70–90%) of natural gas.[37] Recent advances in hydraulic fracturing have led to the effective extraction of natural gas from shale rock and triggered the so-called 'shale gas revolution'.[29,38,39] This increased supply of natural gas makes methane very attractive as both an energy source and feedstock to produce fuels and chemicals. Apart from natural gas reserves, methane is also a central component of biogas produced by the anaerobic digestion of organic materials.[38,40,41] Moreover, methane can be found in crystalline hydrates existing in permafrost areas as well as the continental slopes of many oceans.[38] In view of its abundant reserves and resources, and with the depletion of oil reserves, methane activation will play a key role in ensuring the supply of energy, fuels, and chemicals in the future.

Methane activation can be carried out through both direct and indirect conversion routes. To date, the industrial direct conversion routes of methane into fuels and chemicals have been limited. The challenges associated with these routes arise from the phenomenon that methane is very stable and requires very aggressive operating conditions to activate its C–H bonds, which facilitates undesirable reactions, thus resulting in a loss in activity, selectivity, and yields of desired products.[39] Moreover, the products are more reactive than methane, which necessitates the selective separation of the products and brings more challenges in the chemical process.[42] Despite the great challenges, significant progress has been made in the direct conversion of methane to chemicals, especially in the production of hydrocarbons, such as olefins and aromatics. Direct conversion to olefins can be realized *via* oxidative coupling of methane (OCM),[43–45] and to aromatics can be realized *via* methane dehydroaromatization (MDA).[46] Since recently Schwach *et al.*[12] published an excellent review on direct conversion of methane into value-added chemicals, we will not include this in our review. They gave the fundamentals of C–H activation, analyzed the reaction pathways regarding selective routes of OCM, MDA, and MTOAH (methane conversion to olefins, aromatics, and hydrogen),[47] and provided insights into the reaction mechanisms. Readers who are specifically interested in direct conversion of methane are directed to this review article.

The indirect conversion routes of methane into more valuable chemicals *via* synthesis gas are economically feasible and currently industrially applied. The production of synthesis gas from methane can be realized through three reactions,[42,48,49] namely steam reforming (SRM, eqn (1)), dry reforming (DRM, eqn (2)), and partial oxidation (POM, eqn (3)), which are summarized as follows:

$$\text{SRM: } CH_4 + H_2O \rightarrow CO + 3H_2 \quad \Delta H_{298\,K} = 2.14 \text{ eV} \tag{1}$$

$$\text{DRM: } CH_4 + CO_2 \rightarrow 2CO + 2H_2 \quad \Delta H_{298\,K} = 2.56 \text{ eV} \tag{2}$$

$$\text{POM: } CH_4 + 0.5O_2 \rightarrow CO + 2H_2 \quad \Delta H_{298\,K} = -0.37 \text{ eV} \tag{3}$$

The differences between the three processes are based on the oxidant used, the energetics and kinetics of the reaction, and the synthesis gas produced with different H_2/CO ratios.[40,50] Among the three indirect processes, SRM is the conventional technology for methane conversion due to the highest hydrogen yield, from which approximately 75% of hydrogen is produced.[50] DRM and POM are not industrially mature processes. However, the considerable environmental benefit of DRM[49,51] and the thermodynamic advantage of POM[38] make them have great potential in the future. In view of the importance of these indirect processes in methane conversion, the development of effective catalysts to achieve high activity, selectivity, and stability has a great significance for further methane utilization.

All three processes are found to be active over noble metal catalysts such as Rh, Ru, Ir, Pt, and Pd, and over non-noble metal catalysts like Ni and Co. Moreover, the oxide is one of the crucial types of catalysts to promote methane conversion. So far, the catalyst performance, support effect, promoter effect, deactivation, and kinetics and mechanisms of SRM,[38,39,52–58] DRM,[40,49–51,59–65] and POM[48,66–71] over both noble and non-noble metal catalysts as well as oxide catalysts[16,18,72–74] have been summarized in many reviews. However, these reviews are mostly introduced from experimental points of view, and a systematic understanding of these reactions from a theoretical perspective is still missing. Herein, we mainly review these reactions based on DFT calculations and microkinetic modeling, with the kinetic studies briefly introduced. C–H bond activation in methane is first elucidated.

2.1 Activation of C–H bonds in methane on metal and oxide surfaces

A methane molecule has four H atoms bonded to a single C atom in a tetrahedral orientation. The CH_4 molecule is geometrically highly symmetrical and nonpolar, and it is neither an electron donor nor acceptor. The unique structural and electronic features of the methane molecule make it weakly interact with catalytic surfaces. A high bond dissociation energy of the C–H bond makes methane a relatively unreactive starting material. The first C–H bond activation is the critical step in methane conversion, which has been reported to be the RDS for methane decomposition, oxidation, and steam and dry reforming on different catalysts (Ni, Pd, Ru, and Rh), according to the kinetic studies by Wei and Iglesia[75–80] and other researchers.[81–90] Therefore, understanding the mechanism for

C–H bond activation is essential for further comprehending SRM, DRM, and POM reactions.

2.1.1 C–H bond activation on metal surfaces. On metal catalysts, the first C–H bond activation might take place *via* three pathways, namely direct CH_4 dissociation, O*-assisted CH_4 dissociation, and OH*-assisted CH_4 dissociation. Hibbitts *et al.*[91] carried out DFT calculations to systematically explore the activation of the C–H bond in methane over group 8–10 (Ru, Rh, Pt, Pd, Os, and Ir) and group 11 (Cu, Ag, and Au) TMs. The three methane activation pathways, namely the direct C–H activation, and O* and OH*-assisted activation, were considered, where the transition-state structures on the Pd(111) surface are shown in Fig. 1(a).

Fig. 1(b) gives the activation barrier differences between the three routes as a function of O* binding energy. The respective activation barriers as a function of reaction energy for the three routes are shown as Fig. 1(c–e), respectively. The data of Ru, Rh, Pd, Os, Ir, Pt, Cu, Ag, and Au were reported by Hibbitts *et al.*,[91] and those of Ni, Co, and Fe were obtained from our previous work.[36,87,89,92] For group 8–10 metals (Ru, Rh, Pd, Os, and Ir), the DFT calculated activation barriers of O*-assisted CH_4 dissociation were much higher than those of OH*-assisted CH_4 dissociation, both higher than those of direct CH_4 dissociation. Hibbitts *et al.*[91] also compared the activation barriers for CH_3* dissociation of the three pathways, where the direct route exhibited the lowest activation barrier for the above group 8–10 metals.

Similarly, Niu *et al.*[92] also found that the first C–H bond activation *via* direct CH_4 dissociation (activation energy E_a: 1.21 eV) was more energetically favorable than O-assisted (E_a: 1.66 eV) and OH-assisted CH_4 dissociation (E_a: 3.39 eV) on a Ni(111) surface (Fig. 1c–e). Moreover, the C–H bond activation of CH_3* and CH_2* *via* direct dissociation was energetically preferred over the other two pathways. The observation is in good agreement with those reported by Zhu *et al.*[93] on a Ni(111) surface, by Fan *et al.*[94] on Ni(111), Ni(211), and Ni(100) surfaces, by Wang *et al.*[87,89] on Ni, Rh, Pd, and Pt(111), (211), and (100) surfaces, by Jørgensen *et al.*[86] on Pd(111) and Pd(100) surfaces, by Yoo *et al.*[95] on a Pd(111) surface, and by Wang *et al.*[88] on a Pt(111) surface. Like on Ni, the activation barriers of direct CH_4 dissociation on Co and Fe were also much lower than those of the other two pathways (Fig. 1c–e), and extremely high activation barriers of OH*-assisted CH_4 dissociation (3–4 eV) were observed (Fig. 1e).[36,89] It is worth mentioning that even

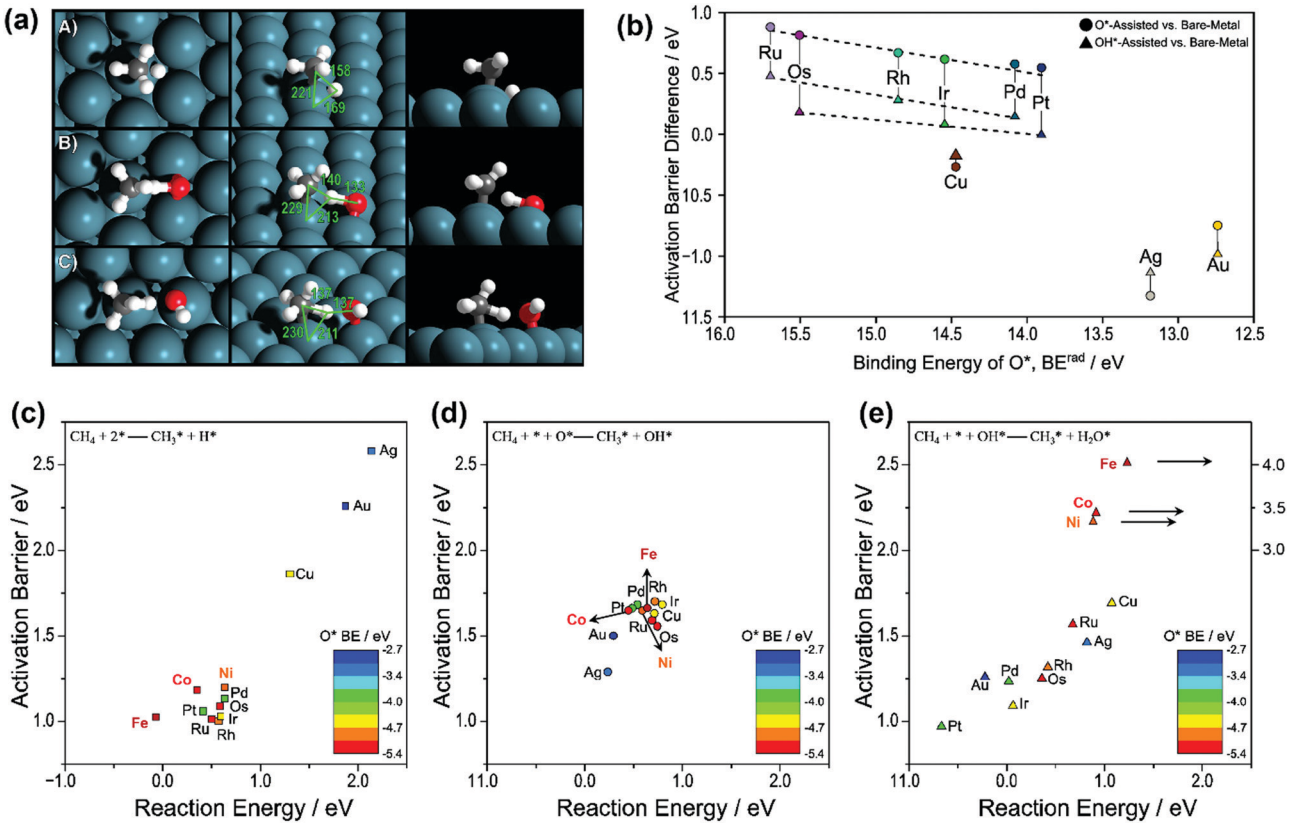

Fig. 1 (a) Transition-state structures for the activation of the C–H bond in CH_4 over (A) metal–metal site pairs (direct), (B) metal–O* site pairs (O*-assisted), and (C) metal–OH* (OH*-assisted) on the Pd(111) surface. Reported bond lengths are given in pm. (b) Difference between the O*-assisted and direct CH_4 activation barriers (●) and the difference between OH*-assisted and direct CH_4 activation (▲) compared to the binding energy of O*. Activation barriers and reaction energies for the CH_4 activation *via* (c) direct CH_4 activation (■), (d) O*-assisted CH_4 activation (●), and (e) OH*-assisted CH_4 activation (▲). Points are colored by the trends in O* binding energy, where red refers to the most strongly bound O* and blue refers to the most weakly bound O* (BE^{rad}, eV). The data of Ni, Co, and Fe in (c), (d), and (e) were obtained from our previous work.[36,87,89,92] The others were reported by Hibbitts *et al.*[91] Adapted from ref. 91 with permission from Elsevier, copyright 2016.

though the direct CH_4 dissociation was also calculated as the energetically most favorable pathway on Co catalysts, Tu *et al.*[96] suggested that the O*-assisted route dominated CH_4 activation on Co and Ni–Co clusters because of their high oxophilicities, resulting in their surfaces covered with oxygen adatoms.

For group 11 metals, the O*- and OH*-assisted routes were energetically preferred over the direct CH_4 dissociation route for both CH_4 and CH_3* dissociation. However, the activation energies of O*- and OH*-assisted C–H activation are still higher than that of the direct dissociation of methane on other groups of metals (8–10). The promotional effects of O* and OH* in activating C–H bonds on the group 11 metals were related to the M–O/M–OH binding energy and their basicity when binding with metal. The weakly bound O* and OH* often participate and assist in C–H bond activation. As such, enhanced promotional effects were observed on the group 11 metal surfaces by O*/OH* over direct metal activation due to their weak M–O/M–OH bonding. Moreover, the O* and OH* are more negatively charged when binding with the group 11 metals, thus increasing their basicity and ability to promote C–H activation. In contrast, the basicity of O* and OH* over the group 8–10 metal surfaces is not strong enough to aid C–H bond activation. As a result, the presence of O* or OH* will reduce the overall reaction rate since they will block active surface sites.

The Pt(111) surface is an exception, where the activation barrier for OH*-assisted CH_4 dissociation was lower than those for the direct dissociation and the O*-assisted route.[91,92,97] On the Pt(211) surface, the direct CH_4 dissociation was the energetically most favorable pathway.[97] However, the preferred reaction pathways need to be determined based on the whole catalytic cycle. Chen and Vlachos[97] proposed that the reactions involving OH*-assisted C–H bond activation and addition were most probably the minor reaction pathways, because the OH coverage was low in methane reforming and oxidation and the direct CH_4 dissociation was suggested as a dominant pathway on both the Pt(211) and Pt(111) surfaces. Similarly, the recent DFT study of Niu *et al.*[92] indicated that the OH*-assisted CH_4 activation was considered as an attractive alternative route for SRM on a Pt(111) surface. However, taking the coverage effect of OH* into account could reasonably lead to the direct CH_4 dissociation route being dominant.

C–H bond activation *via* direct CH_4 dissociation dominates methane activation on group 8–10 metals, which are active catalysts for SRM, DRM, and POM reactions. Gong and coworkers[29] gave a detailed review of the theoretical study of methane dehydrogenation over various transition-metal surfaces, including fcc(111), hcp(0001), fcc(100), and fcc(211). The difference in activation energy between different elementary steps was found to be related to electronic and geometric effects, and the difference between other metals could be associated with the metal d-band center. Therefore, we only give a brief overview here. For instance, the geometries of the transition states (TSs) for CH_4 dehydrogenation on close-packed Ni(111) and stepped Ni(211) surfaces are shown in Fig. 2(a and b), with the corresponding activation energies listed.[94] Among the four elementary steps, the step CH → C + H showed the highest activation barrier for both Ni(111) and Ni(211) surfaces, consistent with that summarized by Gong and coworkers.[29] The high barrier of CH → C + H results mainly from the stability of CH* (electronic effect) coupled with the perpendicular nature of CH* (geometrical effect). As shown in Fig. 2(c), CH* is perpendicular to the Ni(211) surface, where an energy penalty is required to bend the structure parallel to the metal surface in the transition state, and therefore geometrically not favorable for further dehydrogenation. The Ni(211) surface exhibits lower activation energies than the Ni(111) surface due to the existence of under-coordinated atoms on the stepped (211) surface, leading to higher binding strengths of surface intermediates and more stabilization of transition states and final states. Moreover, the geometric effect also influences the activation barriers between stepped and terrace surfaces. The partial charge densities projected onto the bonding states in Fig. 2(c and d) show that the CH species forms bonds with 4 Ni atoms, while 5-coordinated bonding is achieved between the C atom and Ni(211), demonstrating the strong binding of C on the stepped Ni(211) surface.[98]

The activation energy of the C–H activation depends on the metal surfaces (Fig. 1) and the metal dependence follows the Brønsted–Evans–Polanyi (BEP) relationship that the activation energy of the elementary step scales linearly with reaction heat. Nørskov and co-workers found that the C binding energy can be used as a descriptor for the linear scaling relations (LSRs) of CH_x (x = 1, 2, 3) adsorption energies and transition-state energies with respect to their gas-phase energies over various transition-metal surfaces.[33,99,100] The linear relation could also be established between the activation energies and C adsorption energies, as shown in Fig. 3(a), based on our data.[36] CH* dissociation shows the highest activation energy among the dehydrogenation steps, with the energy barriers for CH_4, CH_3, and CH_2 dissociation gradually reduced on the close-packed surfaces. The C–metal binding energy can be simply characterized by the metal d-band center, as shown in Fig. 3(b). This underlines the theory that the binding energy of an adsorbate to a metal surface is strongly dependent on the electronic structure of the surface itself. When the C–H σ bond interacts with the metal d bond, the metal d-band hybridizes with the C–H bonding (σ) orbital to form bonding (d–σ) and antibonding (d–σ)* states. The metal–adsorbate interaction depends on the extent of filling of the (d–σ)* or the location of the d-band center. The energetically higher d-band center results in a higher C binding energy. The higher C binding energy leads to more negative CH_x adsorption energy and its transition-state energy and a lower CH_x dissociation barrier.

2.1.2 C–H bond activation on oxide surfaces. Apart from metal surfaces, metal oxides are one of the important classes of catalysts for C–H bond activation in oxidative methane C–C coupling,[13,101] low-temperature oxidation,[12] solid fuel cells,[102] and chemical looping reforming. A physically adsorbed methane molecule on an oxide surface has a binding energy of only about 0.10 to 0.15 eV.[16] Methane activation could occur *via* either the radical-like transition state (Fig. 4a) or the surface-stabilized transition state (Fig. 4b) on metal

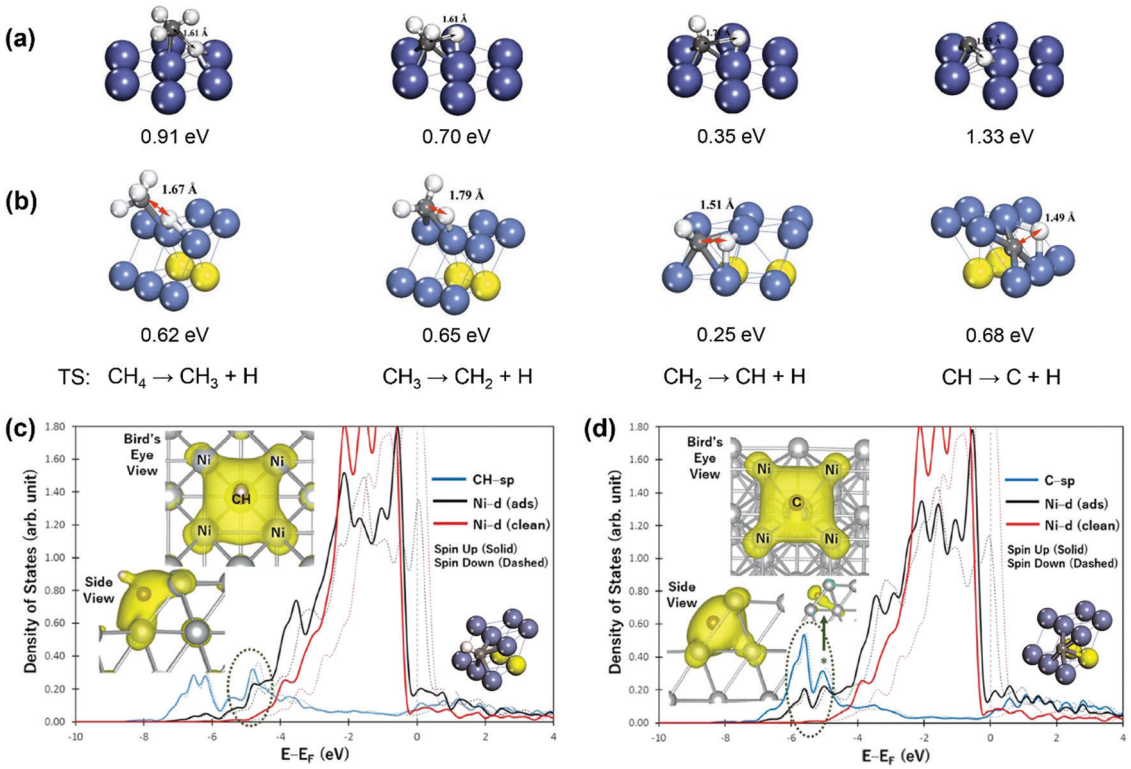

Fig. 2 Geometries of the transition states (TS) for CH_4 dehydrogenation on (a) Ni(111) and (b) Ni(211) surfaces. The values below the geometries are the activation energies of the corresponding elementary steps reported by Zhu *et al.*[93] and Fan *et al.*[94] Reproduced from ref. 93 with permission from Elsevier, copyright 2009. Reproduced from ref. 94 with permission from the American Chemical Society, copyright 2015. The densities of states (DOS) projected onto the sp states of CH (c) and C (d) and the d-band of stepped Ni(211) surfaces. "ads" and "clean" denote the surface with and without an adsorbate, respectively. The left inset figures show the side and bird's eye views of the partial charge density projected onto bonding states within an energy range bound by a dashed ellipse. The right inset figures show the geometries of CH and C on Ni(211) surfaces.[98] Adapted from ref. 98 with permission from Springer Nature, copyright 2017.

oxides.[103–105] The major difference between the two transition states is the distance between C (in CH_4) and the interacted surface metal atom, which illustrates the distinct interaction between CH_4 and the metal surface.[104] Many of the most promising catalysts stimulate alkane activation *via* radical-like TS, due to the energetically unfavorable interaction of the CH_3 with the surface. However, regardless of the transition states, the nucleophilic surface oxygen attacks the electrophilic H in the C–H bond to form an OH bond in C–H bond activation. The hydrogen affinity (E_H) has been shown to be a suitable

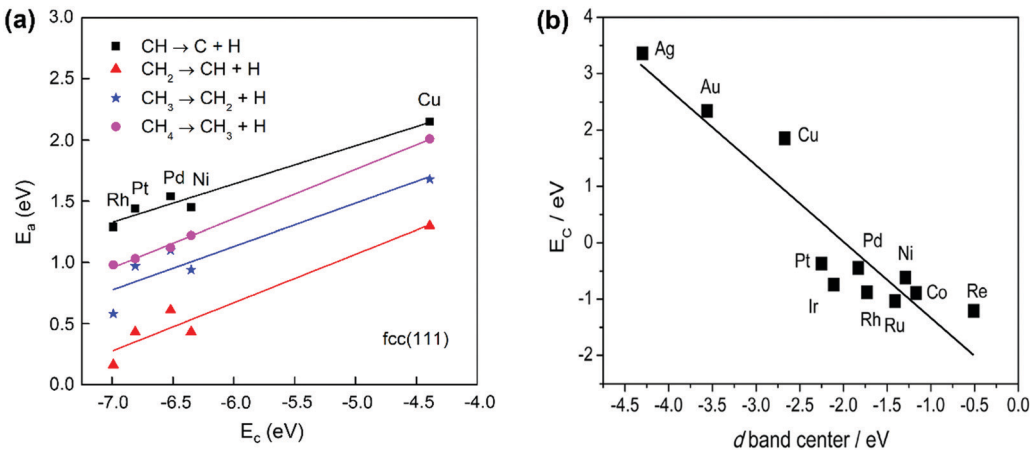

Fig. 3 (a) Activation energies of CH_4 dehydrogenation steps as a function of carbon adsorption energies on an fcc(111) surface, with the data obtained from our previous work.[36] (b) Relationship between C binding energy and the metal d-band center.[29] Published by the Royal Society of Chemistry, copyright 2015.

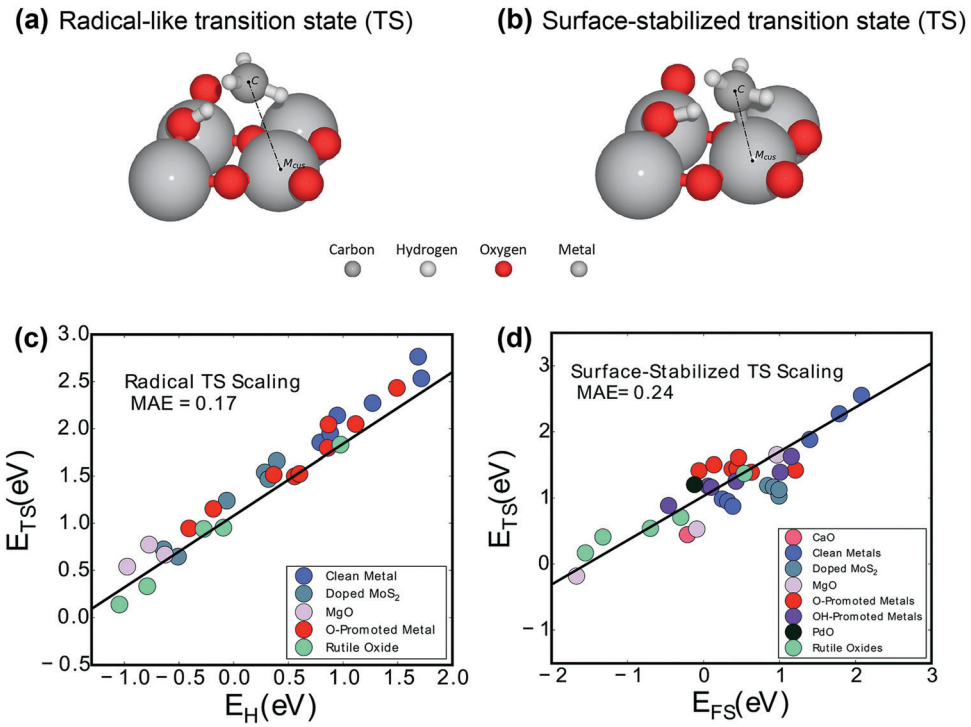

Fig. 4 Two activation mechanisms on rutile-type metal oxide (110) surfaces are exhibited: (a) the radical-like transition state (TS) and (b) the surface-stabilized transition state (TS).[104] Reproduced from ref. 104 with permission from the American Chemical Society, copyright 2019. Universal scaling relations for (c) the radical pathway ($0.75E_H + 1.09$) and (d) the surface-stabilized pathway ($0.67E_{FS} + 1.04$).[103] Reproduced from ref. 103 with permission from the PCCP Owner Societies, copyright 2017.

descriptor of reactivity for radical-like hydrocarbon activation. Latimer *et al.*[103,106] presented a universal scaling relation to predict C–H activation barriers on heterogeneous catalysts, where a transition-state (TS) energy can be correlated with a single universal descriptor for various catalysts that proceed *via* a radical-like TS, as shown in Fig. 4(c). The TS energy is linearly correlated with H binding energy. In addition, all materials they explored that occurred through the surface-stabilized pathway seem to follow the TS scaling relationship which is linearly related to the final state energy, as shown in Fig. 4(d). The authors demonstrated that these scaling relations were valid for several reducible and irreducible oxides, sulfides, and promoted metals.

More interestingly, Latimer *et al.*[103,106] proposed a universal scaling relationship for C–H bond activation (E_{TS}) across reactants and catalysts that depends only on the hydrogen affinity of the catalyst (E_H) and the C–H bond energy of the reactant (E_{C-H}):

$$E_{TS} = 0.75E_H - 1.26E_{C-H} - 4.93 \quad (4)$$

The relationship predicts well the C–H bond activation energies compared to the DFT-calculated ones across a wide variety of reactants and catalysts. The C–H activation energy of methane is the highest due to the more negative C–H bond energy.

Aljama *et al.* studied the role of alkaline metal oxides (MgO, CaO, and SrO)[107] and alkaline earth metal oxides (AEMOs) with an alkaline earth metal (AEM) or a TM as a dopant[108] in breaking the C–H bond in methane. The dopant can change the TS structure. Microkinetic modeling and analysis were performed using the binding energies of H and CH_3 as two descriptors, and a volcano plot was obtained. Even for the surface-stabilized TS on pure alkaline metal oxides, the hydrogen binding energy was found to be a more appropriate descriptor. This suggested that at weak H binding strength, the reaction was limited by C–H bond activation. However, at strong H binding strength, the reaction was limited by poisoning of the active site.

Perovskite oxides with the formula ABO_3 have gained increasing attention in applications in energy-related processes, such as solid fuel cells and chemical looping reforming of methane due to the massive family of combinations of A and B, well-defined structures, and excellent tunability of properties. Fung *et al.*[109] investigated a broad set of perovskite compositions *via* descriptors of O reactivity such as the H adsorption energy, vacancy formation energy, and first C–H activation energy of methane using DFT calculations. The cubic perovskite (001) surface has both 'A' and 'B' terminations, as shown in Fig. 5(a). On each model termination, one possible lattice O site exists for catalysis. On the 'A' termination surface, the O is fourfold-coordinated to the surface A cation and onefold-coordinated to the subsurface B cation. On the 'B' termination surface, the O is twofold-coordinated to both the surface B cation and subsurface A cation. The reactive lattice O activates the methane molecule *via* a homolytic C–H bond

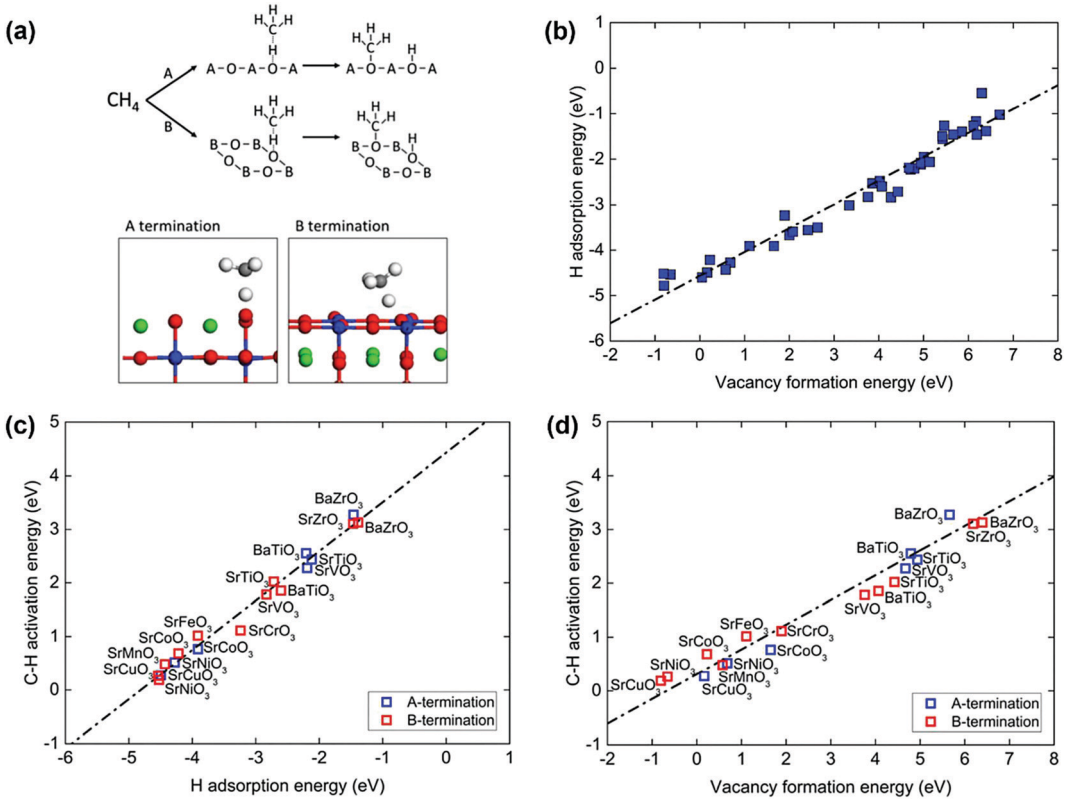

Fig. 5 (a) Top: CH_4 activation on the perovskite (001) A and B terminations. Bottom: The homolytic C–H pathway and the typical transition states (A, green; B, blue; O, red; C, grey; H, white). (b) Correlation between the hydrogen adsorption and vacancy formation energy of the lattice oxygen. Correlations between the homolytic C–H activation energy of CH_4 and (c) hydrogen adsorption energy and (d) oxygen vacancy formation energy. The black dotted line represents the linear best fit.[109] Reproduced from ref. 109 with permission from the Royal Society of Chemistry, copyright 2018.

cleavage, as illustrated in the upper part of Fig. 5(a). The typical geometries of C–H activation transition states over the perovskite(001) surface A and B terminations can be found in the lower part of Fig. 5(a). A strong linear relationship between the H adsorption energy or hydrogen affinity and the O vacancy formation energy was observed, as shown in Fig. 5(b). Both parameters can be used as descriptors for C–H bond activation of methane, as shown in Fig. 5(c) and (d), in good agreement with the universal scaling relationship.[103,106] The stronger the hydrogen adsorption on the lattice O or the easier the O vacancy formation at the lattice-O site, the lower the C–H activation barrier of methane. The oxygen vacancy formation energy has been widely used as a descriptor of the C–H activation energy of methane on CeO_2(111) doped with TMs, TbO_x(111), ZnO, doped TiO_2, and doped MgO;[101] on pure CeO_2(111), (100) and (110) surfaces and surfaces with Pd or Zr substituted in Ce lattice positions;[110] on lanthanum oxides doped with Fe, Mg, Zn, Cu, Nb, Ti, Zr, and Ta; and on undoped catalysts.[111] Oxides doped with low-valence atoms decreased the oxygen vacancy formation energy, which enhanced C–H bond activation. The lowered methane activation barrier was also observed for La_2O_3 catalyst doped with Cu, Zn, or Mg[112] and for CeO_2 doped with Pt.[113] It can be generally proposed that oxides doped with low-valence metals are better methane activation catalysts than the undoped oxides.

2.2 Methane conversion on metal surfaces

Great efforts have been devoted to the first-principles study of the C–H bond-breaking step of methane in a multistep process,[91,98,103,106,114–120] because the C–H bond activation is often the RDS of the methane conversion. However, studying only the C–H activation step is insufficient to gain insight into the reaction mechanism, carbon formation, and RDSs, which can change with catalysts and operating conditions. Calculating the energy profile for the entire catalytic cycle is a demanding task, but it provides the activation barriers for the elementary steps. Microkinetic modeling and analysis of the whole cycle allow us to assess the preferential reaction pathways, RDSs, and dominating surface intermediates. Besides, the scaling relationships related to the binding energies of a wide variety of catalytic intermediates across a range of catalyst surfaces enable us to conduct theory-driven catalyst design. In the next sections, we will review the progress in the first-principles study and descriptor-based microkinetic modeling and analysis of the entire catalytic cycles in steam and dry methane reforming and partial oxidation of methane across a range of catalyst surfaces and catalyst nanoparticles.

2.2.1 Steam reforming of methane

Metal dependence of activity. Steam reforming of methane is one of the main processes for hydrogen production.[121] To date, many efforts have been devoted to investigating the

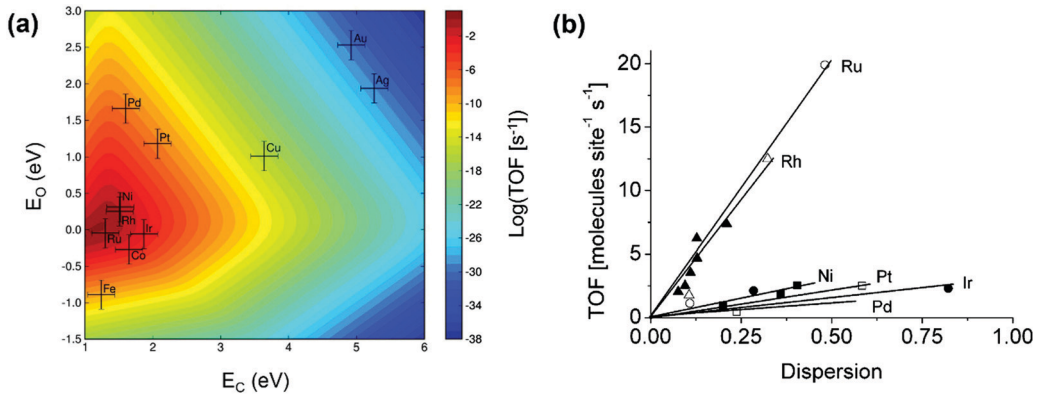

Fig. 6 (a) Microkinetic modeling predicted $\log_{10}$(TOF) as a function of C and O binding energies for SRM. Reaction conditions: T = 773 K, P = 1 bar, 10% conversion. (b) Experimentally measured TOF as a function of dispersion for SRM across Ru (○), 5 wt% Rh (▲), 1 wt% Rh (Δ), Ni (■), Pt (□), Ir (●) and Pd (♦) catalysts. Reaction conditions: T = 773 K, P_{CH_4} = 0.19 bar, P_{H_2O} = 0.74 bar, P_{H_2} = 0.07 bar.[127] Reproduced from ref. 127 with permission from Elsevier, copyright 2008.

SRM reaction from both experimental[75,76,78,122–129] and theoretical[87,89,97,126–128,130–135] points of view. The reaction is active over various transition-metal catalysts. For these metals, most studies demonstrated an activity trend of Ru, Rh > Ni, Ir > Pt, Pd > Co, Fe with a temperature range of 673–1173 K and atmospheric pressure.[87,123,124,127,136] Fig. 6(a) gives the microkinetic modeling results of SRM, reported by Jones *et al.*,[127] and plots $\log_{10}$(TOF) as a function of C and O binding energies as two descriptors. The microkinetic model was built based on the energetics estimated by the linear scaling relationships and BEP relationships over the fcc(211) and bcc(210) surfaces. The descriptor-based microkinetic modeling provided a volcano curve as a function of C and O binding energies as descriptors. Ru, Rh and Ni(211) were found to be active for SRM and the activity is near the predicted optimum activity. It can be explored to design new catalysts with high performance.

At 773 K, 1 bar, and 10% conversion, the model-predicted activity trend is Ru > Rh > Ni > Ir > Pt ∼ Pd. In addition to theoretical calculations, the authors also investigated the activity employing experimental measurements. By assuming that support effects were negligible, the obtained experimental activity trend at 773 K was Ru ∼ Rh > Ni ∼ Ir ∼ Pt ∼ Pd (Fig. 6b). Although the modeling results are not exactly the same as the experimental results, the general trends are consistent. The difference between the theoretical and experimental results might be caused by some sources of errors both in the modeling and in the experiments. The combined DFT, scaling relationship, and descriptor-based microkinetic modeling can effectively describe catalytic reactions at surfaces with the detail and accuracy required for the predicted activity tendency comparable to experiments.

It seems that among these pure metals, Ru and Rh are the most active catalysts, Ni and Ir are moderately active, and Pd and Pt are less active. However, the kinetic studies of Wei and Iglesia[75–80] illustrated a different result, with the activity order as Pt > Ir > Rh > Ru, Ni at 873 K. In their studies, Pt is the most active catalyst. Despite the controversy about the metal activity, Ni, Rh, Ru, Pt and Pd are among the focuses of research for SRM. Ni is the most studied catalyst due to its low cost, abundance, and relatively high activity, and is a commercial and mature industrial SRM catalyst.[58,137] Rh and Ru are normally studied because of their high reforming activity and coke-resistant performance.[133] Pt is also a potential SRM catalyst with high activity, according to Wei and Iglesia's work.[75] A better understanding of the SRM mechanism on these metal surfaces serves as an important step in revealing the nature of this reaction and in aiding the rational design of catalysts.

Metal dependence of the reaction mechanism. The reaction mechanism of steam methane reforming has been long studied both experimentally and theoretically, due to its industrial importance. The reaction mechanism of SRM typically involves methane activation (three C–H activation pathways as discussed above), and CH*/C* oxidation by OH* or O* to form CO. As a result, the mechanism involves many elementary steps, leading to many reaction pathways to form synthesis gas, as shown in Fig. 7.

The activation of C–H bonds in methane generates surface CH_x (x = 1–3), and CH* and C* have been identified as the critical intermediates for CO formation. The CH*/C* may follow five routes to form CO by using O*/OH* as an oxidant (Fig. 7). They are (1) the direct C* and O* combination route (C–O route: CH* → C* → CO*), (2) hydrogen insertion *via* HCO* (CH–O route: CH* → HCO* → CO*) and (3) COH* (C–OH route: CH* → C* → COH* → CO*), and routes that involve the HCOH* intermediate like (4) the HCO–H route (CH* → HCOH* → HCO* → CO*) and (5) the H–COH route (CH* → HCOH* → COH* → CO*). The O* and OH* are provided by the dissociation of H_2O.

DFT calculations and microkinetic modeling are powerful tools for elucidating the reaction pathways for syngas formation *via* the complex reaction mechanism and identifying the RDS, as it is difficult or almost impossible to gain a full picture on the basis of only experimental work. However, due to the coverage or surface concentration effect, it is difficult to determine the dominating reaction mechanisms purely based

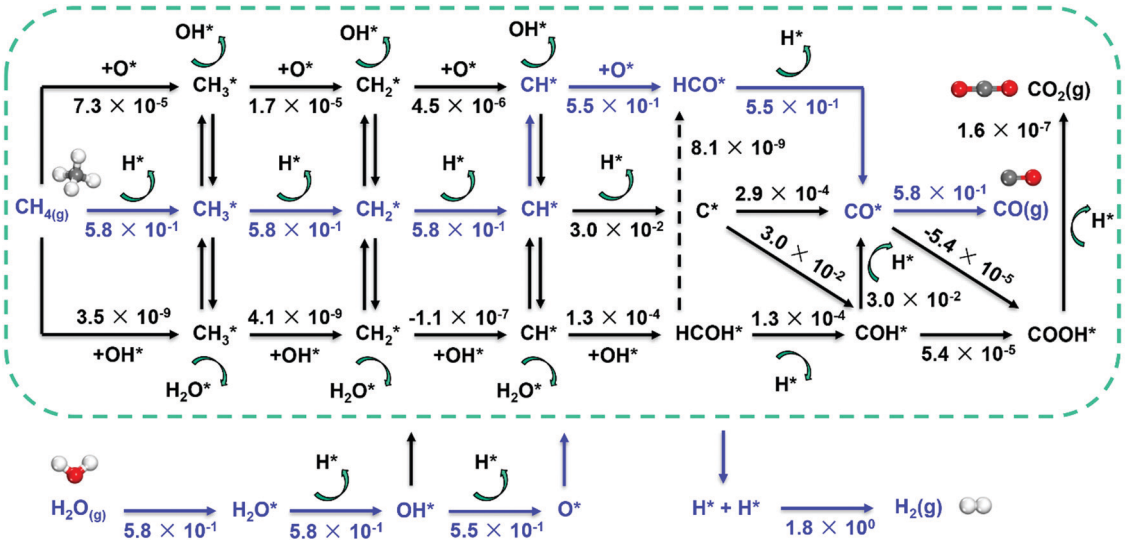

Fig. 7 Reaction network for SRM over Ni catalyst and estimated net turnover frequency (TOF_{Net}) for elementary steps involved in the microkinetic model over the Ni(211) surface. The dominant reaction pathway is colored blue. Reaction conditions: 773 K, 1 bar, S/C = 3.5, and CH_4/H_2 = 1.0.[87] Reproduced from ref. 87 with permission from Elsevier, copyright 2019.

on DFT-calculated barriers under reaction conditions.[29] The microkinetic modeling is therefore employed to clarify further the mechanistic scenario, which provides opportunities to directly acquire the reaction rate by taking into account both energy and coverage.[87,94,130,132,138] Recently, Wang *et al.*[89] conducted comprehensive microkinetic modeling to gain unified insight into the SRM mechanism on different metal surfaces with energetics estimated by combining a DFT-modified UBI-QEP (unity bond index-quadratic exponential potential) method and BEP relationships. The unified 2D mapping of the dominant reaction pathway and the RDS as a function of C and O formation energies is shown in Fig. 8 at 773 K (a) and 1073 K (b). The lower formation energy corresponds to a higher binding energy. The map can be divided into three areas in terms of the dominant reaction pathways. The O*-assisted C–H activation can only be for the catalysts with high C formation energy and low O formation energy. For most of the catalysts, the direct C–H dissociation is the preferred pathway for methane activation. RDSs such as H–CH_3, H–CH_2, C–OH, and CH–O were observed. This clearly shows that the RDS can change with catalysts or conditions. Based on the 2D map, the dominant reaction pathway and the RDS on transition metals Ni, Pt, Pd, and Rh with different surfaces such as (111), (100) and (211) were analyzed. It was found that the direct CH_4 dissociation was the dominant pathway for methane activation for all the metal surfaces concerned, independent of temperature. CO formation mainly takes place *via* the C–OH route on the (100) surface due to the strong C binding strength

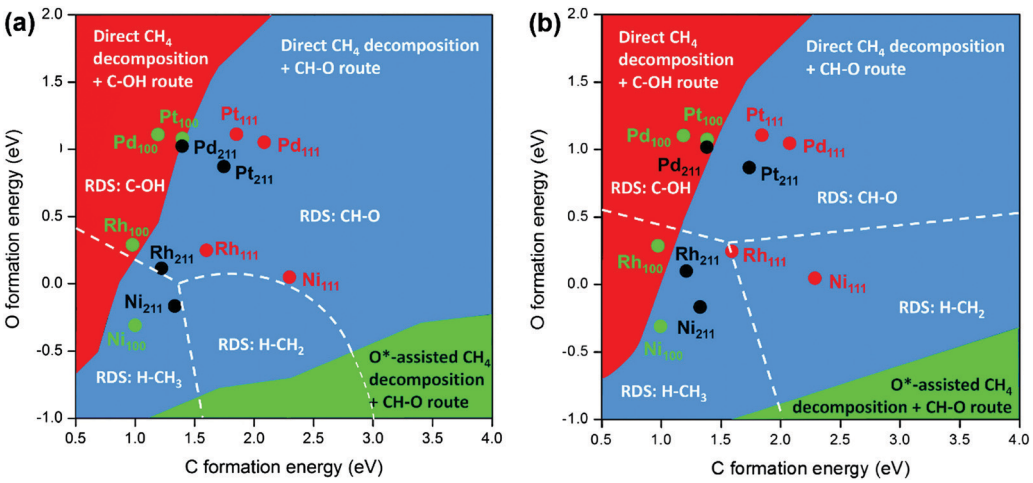

Fig. 8 Schematic diagrams of the dominant reaction pathways (divided by colors) and rate-determining steps (divided by the dashed lines) as functions of C and O formation energies on different metal surfaces for SRM (a) at 773 K, 1 bar, with 18.2% CH_4, 63.6% H_2O, 18.2% H_2, and (b) at 1073 K, 10 bar, with 18.2% CH_4, 63.6% H_2O, 18.2% H_2.[89] Adapted from ref. 89 with permission from the American Chemical Society, copyright 2020.

and relatively weak binding of O, except for Ni(100) with H–CH_3 activation as the RDS. On Pt(111) and (211), CH–O (HCO* formation) is the RDS, while on Ni(211), H–CH_3 activation is the RDS. On Ni(111) and Rh surfaces, with increasing temperature, the RDS changes from HCO* formation to CH_4 dissociation. The change in RDS with temperature agrees with the microkinetic modeling results reported by Jones *et al.*[127]

The reaction mechanism and microkinetics have been intensively studied on Ni, Rh, Ru, Pt, and Pd catalysts. We will review the recent progress in the understanding of the mechanism and RDS on these catalysts.

Ni catalysts. Ni catalyst is the most widely studied catalyst due to its importance in industry where the Ni(111) surface is the most studied surface. In 1997, Aparicio[125] carried out transient isotopic and microkinetic modeling to investigate the SRM mechanism over Ni catalysts. Direct dissociation of methane was experimentally demonstrated to be the main C–H bond activation pathway. The results suggested that there was no unified RDS for SRM. Both the first C–H activation and CO formation could all be kinetically relevant steps depending on the reaction conditions. In some cases, one of them can be the RDS, but in most cases, a combination of them determines the reaction rate. Later, Wei and Iglesia[75–80] conducted a series of kinetic investigations for SRM on a range of metal catalysts (including Ni), which indicated that the first C–H bond activation was the RDS at high temperature (823–1023 K). However, at relatively low temperatures (<773 K), CO formation was expected as the RDS for most metals (including Ni), according to the thermodynamic analysis reported by Jones *et al.*[127] The change in the RDS from CO formation to methane dissociation is caused by the increased reaction barrier of methane dissociation (related to entropy contribution) as the temperature increases.

More detailed theoretical studies relevant to SRM on Ni catalysts have been extensively carried out on Ni(211), Ni(111), and Ni(100) surfaces. In 2002, Bengaard *et al.*[126] combined DFT calculations, microkinetic and Monte Carlo simulations, kinetic measurements, thermogravimetric analysis (TGA), and extended X-ray absorption spectroscopy (EXAFS) to present a comprehensive mechanistic picture of the SRM process on a Ni catalyst. DFT calculations were performed on step Ni(211) and flat Ni(111) surfaces, based on which potential energy diagrams of the full reaction were obtained. The methane activation was considered to be among the RDSs on the Ni(211) surface,[125] which is consistent with the general RDS mapping in Fig. 8. Although Ni(111) exhibited a higher barrier, it has more available active sites because of more facet sites than step sites in a normal particle (except for extremely small particles). Therefore, the authors concluded that there are at least two types of active sites on a Ni catalyst: one is very active, related to certain step and surface defect sites; and the other is less active, related to the close-packed surfaces.

It is generally agreed that the CH–O route was energetically the most preferred pathway on the Ni(111) surface for CO formation.[81,92,93,130,139–141] Wang *et al.*[87] also confirmed the CH–O route as an energetically favorable pathway on Ni(211) as well as Ni(100) and Ni(111) surfaces from 773 to 848 K by microkinetic modeling. However, Blaylock *et al.*[132] illustrated by multi-facet microkinetic modeling of Ni NPs consisting of Ni(111), Ni(211), and Ni(100) that the favorable reaction pathway depends on the reaction temperature. The C–O route was the most preferred pathway at high temperatures; however, at low temperatures, CH–O and C–OH routes were predicted to be more important. Dissociative chemisorption of methane and CO*/HCO*/COH* formation were the RDSs. Xu *et al.*[133] compared the C–O route, CH–O route, and C–OH route on twelve TM stepped (211) surfaces by means of microkinetic modeling and demonstrated that the C–O route was the most favorable pathway owing to the highest estimated rates. CO formation was the RDS at 773 K. In summary, for Ni catalysts, direct CH_4 dissociation is accepted as a dominant route for methane activation, although the exact reaction mechanism for CO formation is still under debate. The RDS can change with temperature and with Ni surfaces.

Rh, Ru, Pt, and Pd catalysts. Mei *et al.*[128] obtained a lower activation barrier for the CH–O route (1.37 eV) than the C–O route (1.59 eV) on a Rh(111) surface. van Grootel *et al.*[131] reported competition between the CH–O route and C–O route on a Rh(111) surface and that the CH–O route was slightly more favorable on a Rh(211) surface through a comparison of DFT calculated activation barriers. Inderwildi *et al.*[142] observed a much lower activation barrier for the CH–O route (0.99 eV) than the C–O route (2.23 eV) on a Ru(0001) surface. Chen *et al.*[97] suggested a dominant pathway of the C–O route on Pt(111) and Pt(211) surfaces. Wang *et al.*[88] demonstrated a primary reaction pathway of the CH–O route involving HCOO* on a Pt(111) surface, while the route involving a CHOH* intermediate turned to be dominant in a moist environment, based on the DFT-calculated activation barrier. Since the SRM mechanism is controversial on different metal surfaces, and it is insufficient to determine the dominant pathway solely based on the activation barrier; microkinetic modeling was employed to further elucidate the mechanism by taking into account both energy and coverage effects.

The microkinetic modeling of steam and dry reforming by Maestri *et al.*[83] predicted that the direct dissociation of the C–H bond was the main pathway of methane activation on Rh catalyst. The microkinetic can describe well the experimental results over a wide range. The microkinetic analysis showed that the CO formation took place by oxidation of the surface C* *via* C* + OH* → CO* + H*, and the CH_3* dehydrogenation (CH_3* + * → CH_2* + H*) was the RDS for both steam and dry reforming.

Towards CO formation, the DFT calculations and microkinetic modeling study of Zhu *et al.*[134] showed that the C–O route was the dominant pathway on Rh(211), Rh(111), Pt(533), and Pt(111) surfaces. The microkinetic modeling of Xu *et al.*[133] indicated that the C–O route was more favorable on Ru and Rh(211) surfaces and that the C–OH route was more preferred on a Pt(211) surface. The DFT-based microkinetic modeling of

Jørgensen *et al.*[86] illustrated that the C–O route was more favorable at high temperatures and the C–OH route involving COH* and OCOH* intermediates was more preferred at low temperatures on Pd(111) and Pd(100) surfaces. The DFT and microkinetic study of Yoo *et al.*[95] revealed that the HCO–H route dominated the reaction on a Pd(111) surface under mildly oxidizing conditions. Trinchero *et al.*[84] reported a C–O route on (111), (100), (211), and (321) surfaces of Pt and Pd using DFT and microkinetic modeling. All the analyses point out that C–H bond activation in methane is among the RDSs, although there is a difference in the exact RDS. As shown in Fig. 8, the RDSs on Rh surfaces change with operating temperature. At relatively high temperatures, the H–CH_3 could be the RDS, in accord with the microkinetic analysis by Maestri *et al.*[83] The microkinetic analysis results agree with the experimental observation reported in the literature.[77,123,143,144]

To sum up, it seems that direct CH_4 dissociation dominates methane activation for Ni, Rh, Ru, Pt, and Pd. The OH-assisted CH_4 dissociation is limited by low OH* surface coverage, although sometimes it is energetically favorable. At the same time, the dominant routes for CO formation are dependent on the catalysts and the metal surfaces. The RDS of the total SRM reaction can change with temperature and with catalysts. The change in RDS with temperature is mainly caused by the large entropy loss of methane, which raises the reaction barrier of methane dissociation as the temperature increases. The change in the RDS with catalysts results from the distinct C–metal and O–metal binding energies on different metal surfaces, which are descriptors to probe the catalyst activity.

Size dependence of activity. In addition to mechanistic research, the metal particle size-dependent activity of SRM also attracted much attention in the previous study. The early work concerning the particle size effect on metal activity for SRM was mainly carried out through experimental measurements. Wei and Iglesia[75–78,80] investigated the effects of metal dispersion on CH_4 reforming turnover rates for Pt, Ir, Rh, Ru, and Ni catalysts. The forward CH_4 turnover rates were observed to increase monotonically with the metal dispersions. Similarly, Jones *et al.*[127] observed a linear relationship between the TOF and dispersion for Ru, Rh, Ni, Pt, Pd, and Ir catalysts, as shown in Fig. 6(b). Since dispersion is inversely proportional to particle size for not too small particles, the particle size effect on activity could be easily obtained; that is, the smaller the particle size, the higher the activity (turnover number) for the investigated metals. The activity was therefore considered to depend on the surface structure of the NPs, and the under-coordination sites (edges, kinks, and defects) were expected to be the active sites for SRM because of the larger fraction of under-coordinated surface sites exposed on small particles than larger particles.[127,145,146] The DFT-based microkinetic modeling was subsequently employed to investigate the size-dependent activity. DFT calculations provide the reaction mechanism and kinetic parameters on specific surfaces such as Ni(111), Ni(100), and Ni(211). The multifaceted microkinetic model brings the bridge between the DFT calculation and the kinetics of nanoparticles.[87,89,123]

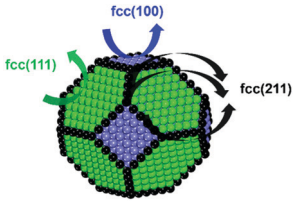

Fig. 9 A truncated octahedron model consisting of fcc(111), fcc(100), and fcc(211) surfaces.[89] Adapted from ref. 89 with permission from the American Chemical Society, copyright 2020.

To gain insight into the size-dependent activity, Wang *et al.*[87,89] reported an approach that combined microkinetic modeling with a truncated octahedron model to calculate the total activity based on the surface fraction and individual surface activity. The schematic diagram of a truncated octahedron model is shown in Fig. 9, which consists of fcc(111) and fcc(100) surfaces, where steps, edges, and corners are treated as an fcc(211) surface. The total reaction rate ($TOF_{CH_4}^{Cal}$) can be estimated by the sum of surface fraction (f_i) times individual reaction rate (TOF_i):

$$TOF_{CH_4}^{Cal} = \sum_{i=1}^{3} f_i * TOF_i = f_{111} * TOF_{111} + f_{100} * TOF_{100} + f_{211} * TOF_{211} \quad (5)$$

where f_{111}, f_{100}, and f_{211} are the surface fractions of (111), (100), and (211), respectively, estimated by a statistical truncated octahedron model. TOF_{111}, TOF_{100}, and TOF_{211} are individual turnover frequencies on the (111), (100), and (211) surfaces, predicted by microkinetic modeling.

For Ni catalyst, the modeling well reproduced the size-dependent activity observed from the kinetic study, namely lower activity on larger sized Ni particles (Fig. 10b).[87] The size-dependent activity was found to result from the surface-dependent activity. Ni(211) was the most active surface for SRM (Fig. 10a), and the decreased Ni(211) surface fraction with increasing particle size resulted in reduced Ni activity (Fig. 10b). The Ni(111) activity was limited by a high energy barrier, and the Ni(100) activity was limited by surface blockage related to C* and CH* deposition (Fig. 11a). The study also demonstrated that stabilizing Ni catalysts with particle sizes $\leq$6 nm (Fig. 10b) could be a good strategy to achieve high activity for SRM reaction. The apparent activation energies calculated from the modeling were 1.13–1.21 eV with the Ni particle size in the range of 8 nm to 12 nm, which was in good agreement with the results measured by experiments, 1.06–1.17 eV for 8–12 nm. These values were also close to the experimental data reported by Wei and Iglesia (1.06 eV),[80] Nikolla *et al.* (1.05 $\pm$ 0.04 eV),[147] Zeppieri *et al.* (1.00 $\pm$ 0.02 eV),[148] and Niu *et al.* (1.08 eV).[92] Moreover, the combined model predicted well the change in the apparent activation energy with Ni

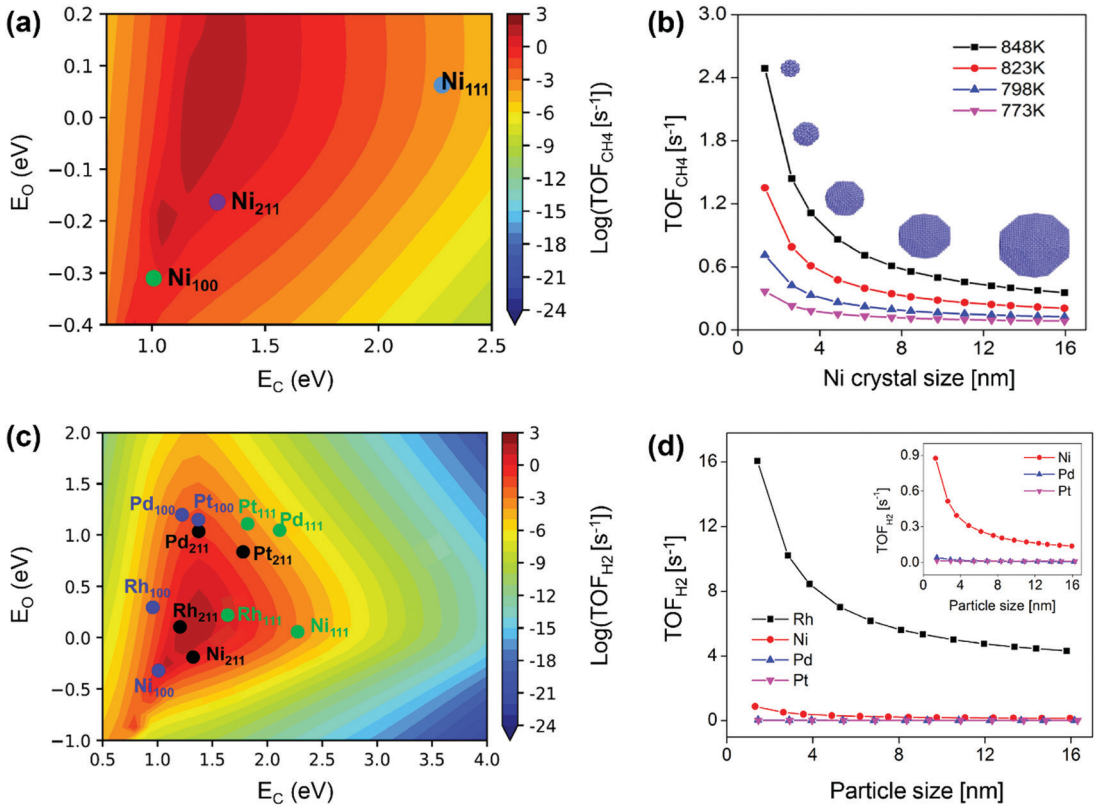

Fig. 10 Modeling predicted forward CH_4 turnover frequency as a function of (a) C and O formation energies in SRM on Ni(111), Ni(211), and Ni(100) surfaces at 773 K, and (b) Ni particle size (1.3–16 nm) at 773, 798, 823, and 848 K.[87] Reproduced from ref. 87 with permission from Elsevier, copyright 2019. (c) Predicted activity for H_2 production over M(111) (green), M(211) (black), and M(100) (blue) surfaces. M denotes Ni, Pd, Pt, and Rh. (d) TOF_{H2} as a function of particle size for Ni, Pd, Pt, and Rh NPs. Reaction conditions: 773 K, 1 bar, S/C = 3.5, and CH_4/H_2 = 1.0.[89] Reproduced from ref. 89 with permission from the American Chemical Society, copyright 2020.

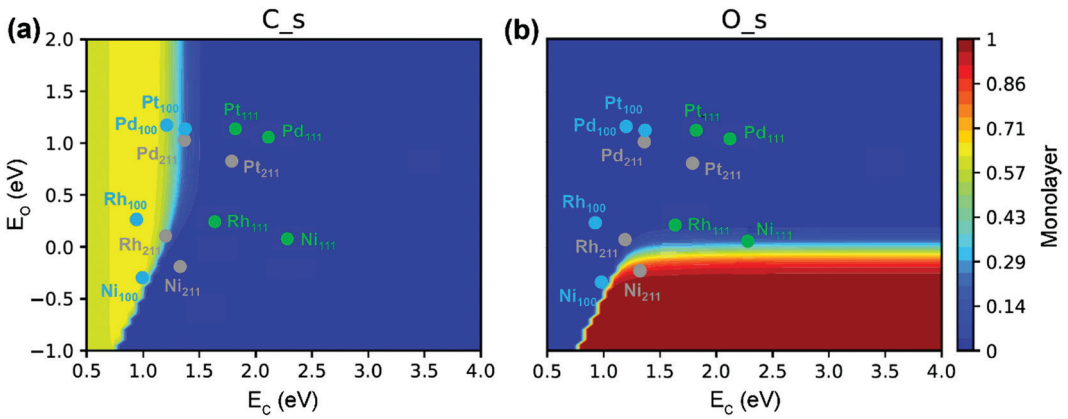

Fig. 11 (a) O* and (b) C* site coverages as functions of C- and O-metal formation energies in SRM. Reaction conditions: 773 K, 1 bar, 18.2% CH_4, 63.6% H_2O, 18.2% H_2.[89] Adapted from ref. 89 with permission from the American Chemical Society, copyright 2020.

particle size, *i.e.*, lower activation energy on larger sized Ni particles. Niu *et al.*[92] reported an effective activation energy of 1.12 eV based on a DFT calculated G plot, also consistent with the experimental values on Ni catalysts. This demonstrated that microkinetic modeling and/or DFT are feasible approaches to characterize the real kinetic properties.

The size-dependent activity of SRM on Rh, Ru and Pt catalysts follows the same trend as that on Ni, namely, the smaller the particle size, the higher the activity.[75–77,80,127,149] Wang *et al.*[89] also provided a systematic and in-depth understanding of the size-dependent activity on Rh, Ni, Pd, and Pt catalysts by combining microkinetic modeling with a truncated

octahedron model. The modeling predicted activity of H_2 production in SRM on each metal surface is shown in Fig. 10(c). It was found that the M(211) surface is most active for Rh, Ni, and Pd catalysts, while for Pt, the M(100) surface is most active. The total activity was estimated by the sum of individual TOF on each surface multiplied by the surface fraction, based on that, the total TOF against particle size is plotted in Fig. 10(d). The TOFs were observed to be inversely proportional to particle size and linearly related to dispersion, in good agreement with reported experimental results.[75–77,80,127,149] The linear scaling between TOFs and dispersion was associated with a linear relationship between surface fractions and dispersion. M(211) was the active surface, and the increased M(211) surface fraction along with increased dispersion led to enhanced NP activity at smaller NP size. As for metal-dependent activity, the catalytic activity of SRM followed Rh $>$ Ni $>$ Pd $\sim$ Pt for both small and large particles. Compared to Rh, the activity of Ni was limited by surface blocking, and the activities of Pt and Pd were limited by high free energy barriers. Although Rh exhibits very high activity, other noble metals such as Ru, Pt, Pd, and Ir are also active for SRM, but these metals are usually too expensive to be applied in conventional industrial reformers. Developing appropriate methods to combine Ni-based catalysts with these noble metals to achieve both enhanced activity and catalyst resistance to carbon deposition seems like a cost-effective way and a promising subject of SRM study in the future.

Catalysts improving carbon formation resistance. Although the use of Ni-based catalysts for SRM is a relatively mature technology, catalyst deactivation through carbon formation, poisoning and sintering tends to occur on the Ni surface, which is an important challenge and is among the subjects of active research.[133] Among them, carbon formation is the most common and significant challenge for Ni-based catalysts. Several types of carbon have been reported on the catalysts towards methane reforming and decomposition,[150] with atomic carbon, encapsulating carbon, and filamentous carbon being the most important.[151] It is generally accepted that the growth of filamentous carbon involves decomposition of the carbon-containing gas to carbon adsorbed on the metal surface, dissolution/segregation of carbon into the bulk, diffusion of carbon through Ni particles to surfaces that are suitable for filament growth, and precipitation of filaments.[152] Chen *et al.*[151] performed a microkinetic analysis of deactivation during DRM over Ni catalyst, where both filamentous carbon and encapsulating carbon were assumed to generate from a surface carbon (C*) precursor. The carbon formation was dependent on the concentration of surface C*, and different operating conditions affected the coking rate through changes in *C site coverage. It was suggested that the formation of monolayer encapsulating carbon blocked the active sites and hence deactivated the methane reforming, the filamentous carbon formation and the encapsulating carbon formation itself.

The C* site coverage is an important parameter to characterize carbon formation. Both experimental and DFT studies of Nørskov and co-workers[126,153] suggested that the nucleation of graphene on Ni catalysts was initiated at the stepped Ni(211) sites. If the surfaces or step edges are too small, the nucleation cannot proceed, thereby further inhibiting the graphene formation. This explains why very small particles cannot grow filamentous carbon under normal conditions. However, the recent microkinetic modeling of Wang *et al.*[89] demonstrated carbon deposition on a Ni(100) surface (Fig. 11a). The absence of graphene formation on very small particles is related to the very low surface fraction of Ni(100), which is an energetically preferred facet of Ni for the formation of carbon. The carbon deposition phenomenon on Ni(100) has also been reported by Schouten *et al.* towards methane decomposition reaction.[154,155] Moreover, Eizenberg and Blakely observed the formation of monolayer graphene on a Ni(100) surface in experiments.[156,157] According to Fig. 11(a), in addition to Ni(100), the Rh(100), Pt(100) and Pd(100) surfaces as well as Rh(211) and Pd(211) surfaces could also suffer from carbon deposition because of the strong carbon binding energy. In contrast, the Ni(211) surface is poisoned primarily by surface O* due to relatively strong O binding energy (Fig. 11b). The active surface for carbon formation is, therefore, still under debate.

High temperature and pressure are beneficial to the removal of carbon formation, based on the thermodynamic analysis.[158,159] It was found that for temperatures above 1100 K there is no possibility of carbon formation for the steam-to-methane ratios above unity. For temperatures below 1100 K, carbon formation removal could be done by increasing the pressure. Therefore, for large-scale hydrogen production through SRM, the pressure is above 10 bar.

Ni-based bimetallic catalysts by alloying Ni (the active metal) with another metal (e.g. Au,[160] Ru,[161] Rh,[55] Co,[162] Pt,[163,164] Ag,[165] and Sn[166]) are generally used to reduce methane dissociation and enhance the surface reaction of carbon removal, which could effectively increase catalyst resistance to deactivation and improve catalyst stability. Besenbacher *et al.*[160] combined molecular beam scattering experiments, scanning tunneling microscopy (STM), and DFT calculations to design a surface alloy for steam reforming. It was demonstrated that alloying Au into the surface layer of Ni could effectively improve the catalyst performance, achieving high resistance to carbon formation, which was confirmed by experimental results. Nikolla *et al.*[166] conducted a DFT study to investigate the effect of a Ni-containing alloy on C deposition relative to monometallic Ni and indicated that the growth of carbon deposits was inhibited by Sn alloying of Ni.

Ni-Based bimetallic catalysts with alloy metals such as Ru, Rh, Pd, Ag, Pt, Cu, and Au were investigated by Fan *et al.*[167] for methane dissociation. The DFT-calculated potential energy diagrams are shown in Fig. 12. They demonstrated that the Cu- and Ag-modified surfaces were energetically more favorable than the bare Ni surface for dissociation reactions. For CH_4* dissociation, the activation barriers on Ru/Ni(111) (0.65 eV), Rh/Ni(111) (0.77 eV), and Cu/Ni(111) (0.88 eV) were lower than that on Ni(111) (0.92 eV). On the other hand, the DFT-calculated C adsorption energies on Pt/Ni(111), Pd/Ni(111), Au/Ni(111), and Rh/Ni(111) were less negative than that on Ni(111), indicating that coke formation was suppressed to a certain extent on these bimetallic catalysts. The Ni–Rh bimetallic catalyst was therefore

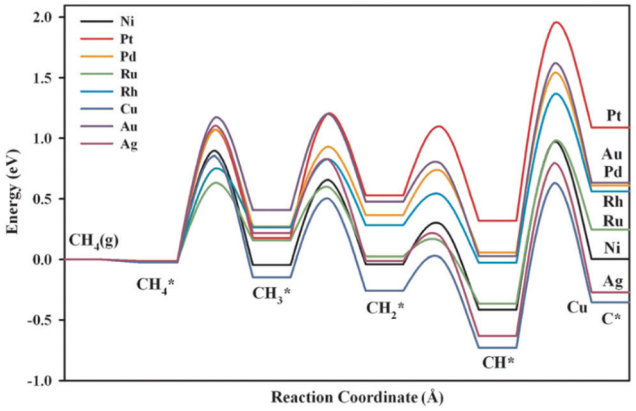

Fig. 12 Potential energy diagrams for methane dissociation on Ni-based bimetallic surfaces. The chemisorbed H atoms required to balance adsorption states have been omitted to simplify the notation.[167] Reproduced from ref. 167 with permission from AIP Publishing, copyright 2012.

suggested as a good candidate for methane dissociation due to improvement in both activity and stability, which has been verified by experimental observations.[168,169]

Xu *et al.*[170] studied the effect of Ag on the control of Ni-catalyzed carbon formation by DFT calculations. The addition of Ag into Ni catalysts reduced the catalytic activity towards SRM but enhanced coke formation resistance. Liu *et al.*[171] reported that segregated NiCu was a good SRM catalyst to suppress coke formation, which displayed the highest carbon deposition resistance among Ni, Fe, Co, Cu, NiFe, NiCo, NiCu, and segregated NiCu catalysts *via* DFT study. Yoon *et al.*[135] compared Ni, Ni–Ru, and Ni–Rh bimetallic catalysts for SRM through DFT calculations, which demonstrated that alloying Ni with Ru could be an effective way to greatly enhance the catalytic efficiency and reduce carbon deposition. Niu *et al.*[92] performed DFT studies on Ni, Pt, and Ni@Pt catalysts for SRM reaction, which revealed that core–shell structured Ni@Pt showed a lower activation barrier for CH and C oxidation but a higher activation barrier for CH dissociation to form C. The Ni@Pt catalyst was found to significantly inhibit carbon formation without sacrificing much activity. To summarize, the Ni–Rh, Ni–Ru, and Ni–Pt alloys are promising bimetallic catalysts to effectively increase catalyst resistance to carbon deposition without sacrificing much activity or even with enhanced activity for SRM reaction.

2.2.2 Dry reforming of methane. Dry reforming of methane is a promising technology to covert greenhouse gases (CH_4 and CO_2) to synthesis gas (H_2 and CO) for the manufacture of value-added products.[49,51,172] Dry reforming of methane has not been an industrially mature process so far. It is an extremely highly endothermic reaction (2.56 eV). Therefore, very high reaction temperatures (as high as 1173 K) are required to attain high synthesis gas yields. The high temperature leads to rapid carbon formation, and thus catalyst deactivation. Moreover, the requirement for pure CO_2 and the long reaction time make DRM still need further development.[62] Ni-Based catalysts are commonly used for this reaction. However, these catalysts tend to undergo carbon deposition and sintering and lose their activity. To overcome this problem, the use of different supports, promoters, and Ni-based bimetallic catalysts has been investigated by many researchers. Here, we summarize the DRM mechanism from kinetic, DFT and microkinetic modeling points of view, with emphasis put on Ni-based catalysts.

Reaction mechanism of DRM. The mechanism of DRM over Ni catalysts has been extensively investigated experimentally. The isotopic kinetics study of Wei and Iglesia[80] indicated that the initial C–H bond activation of methane was the sole kinetically-relevant step for DRM on Ni catalysts. However, some other researchers argued that carbon oxidation,[173–175] the surface reaction between CH_x* and O*,[176] or CH_xO decomposition[177,178] could be the RDS for Ni-based catalysts. The controversial observation could be related to the factor that the mechanism is a function of operating conditions. Using transient isotopic approaches and microkinetic modeling, Aparicio[125] suggested that there was no single RDS in methane reforming over Ni catalysts. Under certain conditions, the availability of surface oxygen may play a key role in determining the rate. Bradford and Vannice[179] proposed a reaction model for DRM, where CH_4 dissociation and CH_xO decomposition were assumed as RDSs, which correlates experimental data successfully. The same RDSs were obtained by Nandini *et al.*[180] over the Ni–K/CeO_2–Al_2O_3 catalyst. The kinetic study of Cui *et al.*[181] indicated that CH_4 dissociation was the RDS at low temperature, while the reaction between CO_2 and CH_x became the RDS at high temperature. Zhang *et al.*[182] developed a Langmuir–Hinshelwood (L–H) model, assuming CH_4 dissociation and the reaction between activated CO_2 and the C species as RDSs over a Ni–Co/Al–Mg–O catalyst, which agrees well with the experimental data. Despite the numerous experimental studies devoted to investigating the mechanism of DRM, there are still arguments between different researchers. The theoretical studies were therefore employed to further elucidate the reaction mechanism of DRM.

The theoretical DRM mechanism is usually interpreted in terms of CH_4 activation, CO_2 activation, and CO formation. CH_4 activation was generally believed to take place *via* the direct dissociation route, which has been reviewed in detail in Section 2.1.1. CO formation pathways are the same as those in SRM reaction. CH* and C* are the critical intermediates for surface oxidation by O* or OH*. CO_2 activation is the key step that is different from SRM.

CO_2 activation. Concerning CO_2 activation, the direct decomposition ($CO_2 \rightarrow CO + O$) and H-induced CO_2 decomposition ($CO_2 + H \rightarrow COOH \rightarrow CO + OH$) were considered by Zhu *et al.*[93] on a Ni(111) surface. The geometries of the initial states, intermediates, and transition states for CO_2 decomposition obtained from DFT calculations are shown in Fig. 13(a–f). The total energy and free energy diagrams for the two routes on the Ni(111) surface are given in Fig. 13(g). It was observed that the CO_2 direct decomposition was energetically more favorable than H-induced CO_2 decomposition. The CO_2 direct decomposition was also supported by Jiao and co-workers on both Ni(111) and Ni(211) surfaces.[81,82,183,184]

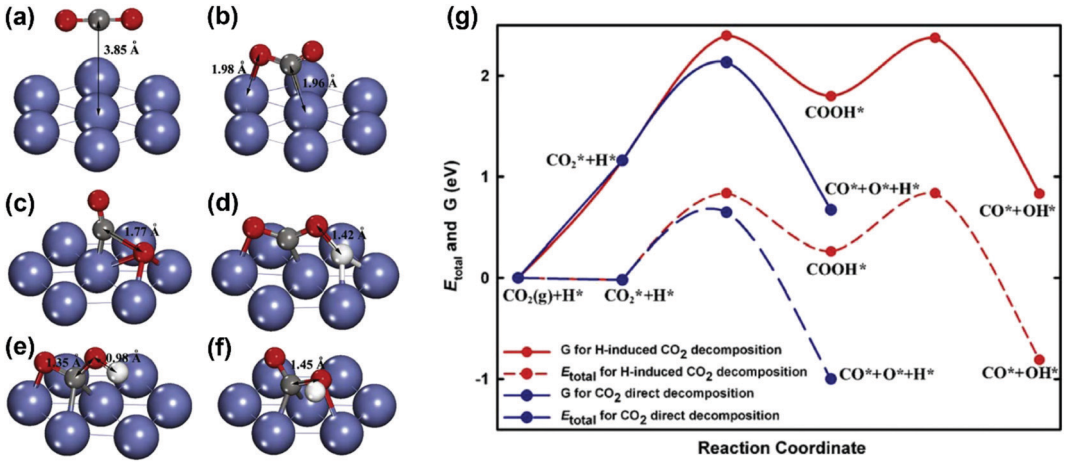

Fig. 13 Geometries of (a) the physisorbed CO_2 on Ni(111), (b) the chemisorbed CO_2 on Ni(111), (c) the transition state for CO_2 decomposition *via* the direct pathway, (d) the transition state for the H-inducted CO_2 decomposition, (e) the intermediate for the H-induced CO_2 decomposition, and (f) the transition state for COOH dissociation to generate CO and OH, and (g) total energy and Gibbs free energy diagrams for the CO_2 direct decomposition and H-induced CO_2 decomposition on Ni(111).[93] Reproduced from ref. 93 with permission from Elsevier, copyright 2009.

CO_2 activation on other metals has also attracted some attention.[185,186] Ko *et al.*[185] systematically investigated CO_2 activation and dissociation on a series of pure metal surfaces and bimetallic alloy surfaces by using DFT calculations. The scaling relations (Fig. 14a) were obtained, where the reaction heat $\Delta E(CO_2^{\delta-})$ of CO_2 dissociation scaled linearly with the

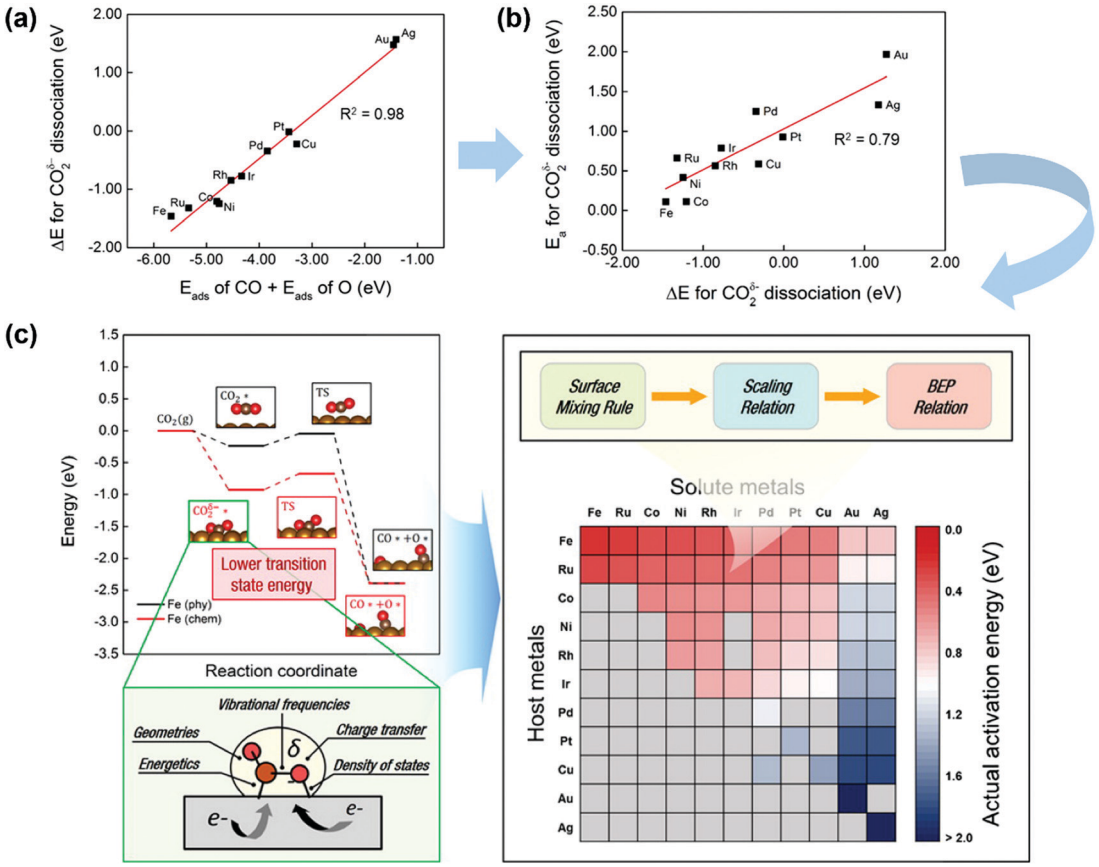

Fig. 14 (a) Scaling relations between E_{ads}(CO) + E_{ads}(O) and $\Delta E(CO_2^{\delta-})$ on TM surfaces. (b) BEP relationships for $CO_2^{\delta-}$ dissociation. (c) CO_2 activation pathways and screening for E_a^{act} for CO_2 dissociation on pure metals and bimetallic alloys. Gray cells indicate that the bimetallic alloys are not preferred for the surface segregation of solute atoms. Here, E_a^{act} is estimated by combining the BEP relation, scaling relation, and surface mixing rule.[185] Reproduced from ref. 185 with permission from the American Chemical Society, copyright 2016.

sum of the adsorption heats of CO and O over various pure metal surfaces. Meanwhile, the BEP relationships were suitable (see Fig. 14b), with the $CO_2^{\delta-}$ dissociation barrier linearly correlated with $\Delta E(CO_2^{\delta-})$. In light of this fact, the activation energies of CO_2 dissociation over pure metal and bimetallic surfaces could be rapidly predicted by combining the surface mixing rule, scaling relation, and BEP relationship, as illustrated in Fig. 14(c). The barrier increases from left to right and from top to bottom. Fe, Ru, Co, Ni, Rh, and Ir pure metals as well as Fe-, Ru-, Co-, Ni-, Rh-, and Ir-based bimetallic alloys exhibited relatively low E_a^{act} values ($\sim$0.75 eV). Pd, Pt, and Cu pure metals as well as Ru-, Co-, Ni-, Rh-, Ir-, and Cu-based bimetallic alloys showed moderate E_a^{act} values (0.76–1.50 eV). Au and Ag pure metals as well as Pd-, Pt-, and Cu-based bimetallic alloys were observed to take high E_a^{act} values (1.51 eV).

Support and promoter effects are important factors in facilitating CO_2 activation. Kattel *et al.*[187] combined DFT calculations, kinetic Monte Carlo (kMC) simulations, and experimental measurements to investigate CO_2 hydrogenation over Pt, Pt/SiO_2, and Pt/TiO_2 catalysts. It was found that Pt NPs alone were not able to catalyze CO_2 activation due to the weak bonding with CO_2. Once CO_2 was stabilized, for example by using SiO_2 or defected TiO_2 with O vacancy as the support for Pt NPs, the overall CO_2 conversion would be enhanced *via* increased CO_2 binding. Pt/TiO_2 exhibited more significant enhancement than Pt/SiO_2 and thus higher activity. Yang *et al.*[188] studied the reduction of CO_2 by hydrogen over Au/TiO_2 and Au/CeO_x/TiO_2 surfaces. On Au_3/TiO_2, the reaction was suppressed by the relatively large barrier (1.23 eV) for the activation of $*CO_2$ to $**CO_2$, which was significantly promoted in the presence of CeO_x (0.16 eV). On Au/CeO_x/TiO_2, an electronic metal–support interaction resulted in a charge redistribution in the metal around the Au–ceria interface. Such surface electronic polarization at the metal–oxide interface enhanced both CO_2 adsorption and activation. Niu *et al.*[189] employed both kinetic studies and DFT calculations to investigate the effect of oxide additives (CeO_2, ZrO_2, ZnO) on hydrotalcite-derived Ni catalysts for DRM reaction. Regarding CO_2 activation, the apparent activation energies obtained from the Arrhenius plot for CeO_2–Ni (0.62 eV) and ZrO_2–Ni (0.64 eV) were lower than that of Ni (0.68 eV). In contrast, ZnO–Ni exhibited a higher activation barrier (0.77 eV) than Ni. It was suggested that the addition of CeO_2 and ZrO_2 could lower the CO_2 activation energy on Ni catalyst, thus promoting CO_2 dissociation to CO and O. The authors also calculated the TOF based on Gibbs free energy, which was 5.92 s^{-1} at 1023 K for CO_2 activation on the support, very close to the experimental value (6.13 s^{-1} at 1023 K), but much higher than that on the Ni surface (4.42×10^{-6} s^{-1}). This demonstrated that the oxides played a significant role in CO_2 activation in DRM reaction.

For the overall DRM reaction, DFT-based microkinetic modeling was applied to explore the mechanism on various metal surfaces such as Ni(111),[85,94] Ni(100),[94] Ni(211),[94] Pt(111),[85,190] and Pd(111).[85] Regardless of the catalyst surface, direct dissociation was favored for C–H bond activation of methane. Direct dissociation is a preferred route for CO_2 activation on Ni,[85,94] but the H-assisted route *via* the COOH* intermediate is preferred for Pt and Pd catalysts.[85,190] However, different preferred routes for CO formation such as C* + O* on Ni,[94] CH* + O* on Ni(111), Pt(111) and Pt(111),[85] and CH* + OH* on Pt(111)[190] were proposed by different studies. The mechanism is very similar to the one of SRM. The RDS was dependent on operating conditions. At high CH_4 and CO_2 partial pressures, carbon oxidation was suggested as the RDS, while at low pressures, both CH_4 dissociative adsorption and C oxidation would jointly determine the overall reaction rate for the DRM reaction.[94] Since DRM has attracted more and more attention due to environmental effects, the DRM mechanism is still under debate, and more theoretical studies are essential to gain insight into the reaction, further aiding the rational design of catalysts.

Metal dependence of activity. Like SRM, the DRM reaction is active on metal catalysts, such as Ni, Ru, Rh, Pt, Pd, Ir, and Co.[123,191–193] As discussed above, the C–H activation and CH and/or C reaction with surface O* are kinetically relevant steps in DRM. Besides, the CO_2 activation leading to surface O* formation is a function of support. Therefore, the metal dependence of the dry reforming activity depends also on the support used. Rostrup–Nielsen and Bak Hansen obtained an activity tendency on a TOF basis as Ru > Rh > Ni > Ir > Pt > Pd on a MgO support[123] like SRM.[127] Solymosi *et al.* reported an activity (in terms of turnover number) trend in the order of Ru > Pd > Rh > Pt > Ir on an Al_2O_3 support for the DRM process.[193] Ferreira-Aparicio *et al.* observed a TOF tendency of Rh > Ni > Ir > Ru–Pt > Co on an Al_2O_3 support, and Ni > Ru > Rh–Ir > Co–Pt on a SiO_2 support.[191] Although the metal performances have some differences among different supports and different studies, Ni catalyst is of particular interest in DRM because it is less expensive than noble metals and exhibits relatively high activity.[63]

Size dependence of activity. The kinetic study of Wei and Iglesia[75,80] illustrated a positive size-dependent activity for DRM on Pt, Ir, Ni, Rh, and Ru catalysts, namely the smaller the metal NPs, the higher the activities. The size dependence of the activity of DRM is similar to the one of SRM, as discussed in Section 2.2.1. Similarly, Lustemberg *et al.*[194] reported that Ni–ceria systems involving the smallest highly dispersed Ni particles were more efficient for methane activation and reforming than larger particles. This is related to the strong metal–support interactions, which affect the charge transfer between Ni particles and ceria. Small Ni particles on stoichiometric ceria undergo large electronic perturbations, which lead to a relatively low activation barrier of the first C–H bond cleavage of methane, compared to extended Ni surfaces. However, recently, Vogt *et al.*[195] established a volcano behavior of size-dependent activity for SRM and DRM at 773 and 873 K, and 5 bar, where the optimal Ni particle size was approximately 2–3 nm. Ni particles smaller than 2.5 nm exhibited a different structure sensitivity from that expected from the above

literature. CH_4 activation, CO_2 activation, and CO formation were possibly important kinetically limiting steps for DRM.

Catalyst improvement. Carbon formation on Ni-based catalysts is the main obstacle to the commercialization of DRM.[140] To investigate the carbon formation scheme on Ni-based catalysts, Wang *et al.*[140] compared the whole reaction network of DRM over flat Ni(111) and step Ni(211) surfaces, as well as flat $Ni_3C(001)$ and step $Ni_3C(111)$ by DFT calculations. The kinetic analysis illustrated an activity order of Ni(111) > $Ni_3C(001)$ > Ni(211) > $Ni_3C(111)$ for DRM. That is, flat surfaces were more active than step surfaces, and metallic Ni catalysts were more active than nickel carbide. Therefore, the formation of nickel carbide would reduce the catalytic activity on both flat and step surfaces. With respect to carbon formation, the authors suggested that the rate ratio of the CH oxidation route to the C oxidation route (r_{CH}/r_C) coupled with the CO dissociation barrier could be used to measure the carbon formation probability. Ni(111) was found to exhibit both the highest activity and the best carbon resistance.

In addition to pure metal catalysts, a few theoretical studies have been employed to investigate the mechanism on Ni catalysts with supports, promoters, and Ni-based bimetallic catalysts for DRM reaction with improved performance. The experimental and computational studies of Akri *et al.* revealed that Ni atomically dispersed over Ce-doped hydroxyapatite (HAP-Ce) was highly active and intrinsically coke-resistant due to strong metal–support interactions, which favor only the first C–H bond activation in methane and stabilize Ni single atoms towards sintering.[196] The DFT studies of Rodriguez and coworkers[194,197,198] indicated that the effective barrier of methane activation decreased from 0.9 eV over a Ni(111) surface to only 0.15 eV over a $Ni/CeO_{2-x}(111)$ surface (Fig. 15). The electronic or chemical properties of Ni were modified with CeO_2 through strong metal–support interactions. The strong interactions enhanced the Ni reactivity for methane dissociation and probably prevented carbon deposition and deactivation during DRM.[197] Moreover, a decrease in the barrier of the first C–H bond activation of methane from 1.07 eV over the Co(0001) surface to 0.87 eV over the $Co^{2+}/CeO_2(111)$ surface, and to only 0.05 eV over the $Co^0/CeO_{2-x}(111)$ surface, was obtained by Liu *et al.*[198] through DFT calculations. This suggests that the reduction degree of the CeO_2 or oxygen vacancy is vital for the activity of Ni/Co sites. The Ni/Co cation on CeO_2 shows a much lower activity for C–H activation of methane compared to the Ni/Co cation on reduced CeO_2 (Ce_2O_3). CO_2 dissociation was observed to take place on the oxide surface at 700 K, under DRM conditions, and no coke deposition was found in the catalytic cycle. CeO_2 is an efficient support that can play an essential role in the DRM process. In contrast, single-site $Ni_1/Mg(100)$ was not active for CO_2 and CH_4 dissociation, while $Ni_4/MgO(100)$ enabled the formation of H_2, CO, and H_2O under DRM reaction, revealed by combined DFT, kMC simulation, and experimental studies.[199] The Ni cluster provided the active sites, and MgO offered the Mg_{vac} as an anchor for Ni clusters to prevent Ni aggregation. The study revealed

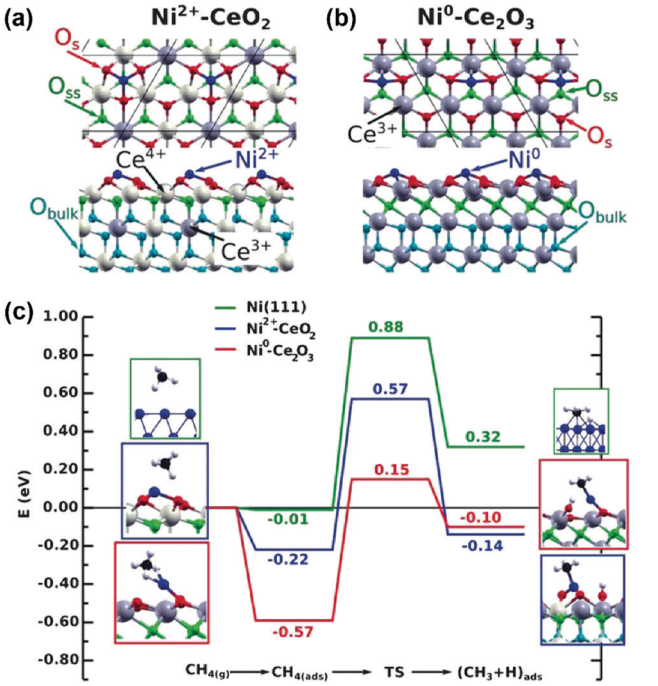

Fig. 15 Atomic structures of Ni adsorbed on (a) $CeO_2(111)$ and (b) $Ce_2O_3(0001)$. (c) Reaction energy profiles for the $CH_4 \rightarrow CH_3 + H$ reaction on Ni(111), $Ni^{2+}/CeO_2(111)$, and $Ni^0/Ce_2O_3(0001)$. The structures shown on the left and right of the reaction pathways correspond to the side views of the optimized initial (molecularly adsorbed) and final (dissociated) states used in search of the transition state. O_s = surface oxygen atoms, O_{ss} = subsurface oxygen atoms, and O_{bulk} = bulk oxygen atoms.[197] Reproduced from ref. 197 with permission from Wiley-VCH, copyright 2016.

that the oxygen vacancy enhanced the C–H activation of methane. However, the whole catalytic cycle involving the oxygen vacancy was not analyzed. It is highly desired to analyze the elementary reaction steps at the metal–oxide interface in the catalytic cycle to gain a better understanding of the role of the interface in DRM.

Foppa *et al.*[200] employed a multiscale (DFT and microkinetic) modeling approach to investigate the role of a Ni/Al_2O_3 interface in WGS (water–gas shift) and DRM. The Ni/Al_2O_3 interface provided the active site for WGS, while all Ni atoms were active for DRM, which was confirmed by the experimental measurements. Li *et al.*[201] combined DFT, CO_2-TPD, and *in situ* DRIFTS to investigate the interfacial synergism of Ni/La_2O_3 catalysts towards CO_2 activation in DRM. They proposed a mechanism that CH_4 activation occurred on the Ni surface to form H_2 and activated coke precursors. CO_2 activation took place at the Ni/La_2O_3 interface to generate bidentate carbonate. Then bidentate carbonate underwent a reaction with adjacent activated coke precursors to generate CO. Therefore, carbon deposition was avoided at the Ni/La_2O_3 interface. The more the Ni/La_2O_3 interface existed, the better the stability by inhibiting the coke deposition.

Li *et al.*[202] combined DFT and microkinetic modeling to investigate the DRM reaction mechanism on a Ni(111) surface with La and La_2O_3 as promoters. For La modified Ni(111), the dominant pathway was $CH_4 + CO_2 \rightarrow CH + 3H + CO + O \rightarrow CHO + 3H + CO \rightarrow 2CO + 2H_2$, with $CH + O \rightarrow CHO$ as the RDS.

For La_2O_3 modified Ni(111), $CH_4 + CO_2 + La_2O_3 \rightarrow CH + CO_2(La_2O_2{-}O) + 3H\ CHO + CO_2(La_2O_2) + 3H \rightarrow 2CO + 2H_2 + La_2O_3$ was the dominant reaction pathway, with $CH_4 \rightarrow CH_3 + H$ as the RDS. The modified catalysts improved the DRM reaction both thermodynamically and kinetically. Moreover, the carbon deposition was inhibited on La_2O_3 modified Ni(111) because of the lower reaction rate in $CH \rightarrow C + H$, compared to that on La modified Ni(111).

For Ni-based bimetallic catalysts, NiSn was observed to favor methane dissociation,[203] and reduce coke formation[204] more than pure Ni catalysts for DRM *via* both theoretical and experimental studies. NiFe bimetallic catalysts suppressed coke deposition due to the increased energy barrier of $CH \rightarrow C + H$, in comparison to that on a pure Ni(111) surface.[205] Furthermore, under DRM conditions, Fe was oxidized partially to FeO, leading to a partial dealloying. FeO could react with surface carbon deposits to form CO, where the reduced Fe returned to the original NiFe alloy.[205,206] The FeO/Ni(111) interface exhibited easier C–O bond cleavage of CO_2 and dehydrogenation of CH_x (x = 1–3). Therefore, both improved DRM reactivity and coke resistance were obtained on NiFe catalysts. The $Ni_2Cu(111)$ catalyst displayed superior carbon deposition resistance compared to Ni(111) and $Ni_2Fe(111)$ due to the higher energy barrier of CH dissociation. It could also improve carbon elimination by enhancing C* + O* reaction, resulting in improved catalyst stability.[207] NiPt bimetallic catalysts showed higher reaction barriers for CH cracking and lower carbon adsorption energy than that on pure Ni(111), which decreased the possibility of coke formation. It can be concluded that the use of supports, promoters, and Ni-based bimetallic catalysts can effectively suppress coke formation on Ni surfaces. Meanwhile, some supports, such as CeO_2, promoters such as La_2O_3, and Ni-based bimetallic catalysts such as NiSn and NiFe can improve the metal activity for DRM due to enhanced methane activation.

2.2.3 Partial oxidation of methane. Partial oxidation of methane is another process for synthesis gas production, which can also be used to produce methanol.[208,209] Herein, we only focus on the POM to synthesis gas. This process, like SRM, has a long history but has attracted much less attention until the 1990s.[48,69] Owing to its thermodynamic advantages and the produced H_2/CO ratio of 2, which is desired for downstream methanol and Fischer–Tropsch (FT) synthesis, POM may become increasingly important in methane conversion and as an attractive alternative to SRM which may applied in industry in the future.[38,210] Despite its exothermicity, high temperatures (1100–1200 K) are required to obtain H_2 and CO. The high temperatures make the reaction difficult to control. Moreover, the hot spots formed during this process are difficult to handle and might cause local overheating. These issues, coupled with the danger of a mixture of methane and oxygen, result in the main problems (safety issues) of POM. Additionally, catalyst stability is another factor that hinders this process from being industrialized.[42] In this review, the POM mechanisms on TMs are summarized, mainly from theoretical points of view based on DFT calculations, microkinetic modeling, and kinetic analysis.

Metal dependence of the reaction mechanism. Although many studies have been carried out to elucidate the mechanism of POM reaction, the mechanism of synthesis gas formation is not yet completely clarified. In the literature, two reaction mechanisms have been proposed for POM reaction: one is the ''direct partial oxidation'' (DPO) mechanism, in which CH_4 and O_2 react on the catalyst surface to generate CO and H_2 directly; and the other is the ''combustion and reforming reaction'' (CRR) mechanism, which involves total methane combustion to form H_2O and CO_2 first, followed by SRM and DRM to produce CO and H_2.[38,48,69,70,211,212] The latter mechanism was suggested by Prettre *et al.*[213] as early as 1945, but due to the highly desired direct selective route to produce synthesis gas, significant efforts have been made towards investigating whether this can be achieved in practice.[69]

Rh and Pt are two of the most widely used catalysts in POM reaction.[214] The first simulations on POM over Pt and Rh surfaces were reported by Hickmann and Schmidt,[69,215,216] using a model with 19 elementary steps containing adsorption, desorption, and surface reactions. The reaction parameters were obtained from the literature or from fitting to previous experiments. The model results demonstrated that at high temperatures with CH_4-rich conditions, CO and H_2 were primary products of direct methane oxidation *via* a pyrolysis mechanism. The superiority of Rh over Pt towards the direct oxidation of methane to CO and H_2 was due primarily to the much lower activation barrier of OH formation from O* and H* on Pt than that on Rh (0.11 eV for Pt *vs.* 0.87 eV for Rh).

Boucouvalas *et al.*[217] conducted a kinetic study of POM over supported Rh catalysts. The calculated apparent activation energy of CO_2 formation was around 0.35 eV, which was close to that of methane conversion ($\sim$0.39 eV). In contrast, the apparent activation energy of CO formation was 0.88–1.13 eV, close to those for CO production from SRM and DRM,[123,217–219] and much higher than that for CO_2 formation. It was suggested that the POM followed an indirect (CRR) mechanism; namely, the reaction initially involved total oxidation of methane to CO_2 and H_2O, followed by reforming reactions to synthesis gas. The kinetic study reported by Kondratenko *et al.*[210] also illustrated that CO and H_2 were mainly produced through SRM and DRM at least in the case of complete oxygen conversion. Donazzi *et al.*[143] carried out a kinetic study of POM over a $Rh/\alpha\text{-}Al_2O_3$ catalyst, with SRM, DRM, WGS, reverse-WGS, CO and H_2 combustion tests also conducted to refine the study. It was found that under the POM conditions the kinetic role of DRM is negligible; therefore SRM and CH_4 total combustion account for the consumption of methane.

Mallens *et al.*[220] employed a transient kinetic study to investigate the reaction mechanism of POM to synthesis gas over Pt. The methane decomposition took place on reduced platinum and resulted in surface C* and H*, which produced CO and CO_2 in parallel by the involvement of different oxygen species. In the presence of both CH_4 and O_2 at a stoichiometric feed ratio, the major reaction pathways were the direct formation of H_2 and CO followed by their consecutive oxidation. Based on the study, a Mars–van Krevelen (MVK) redox cycle[221]

was postulated for POM over Pt: the methane oxidation was accompanied by the reduction of platinum oxide, which was re-oxidized *via* incorporation of dioxygen into the catalyst.

In view of the controversy in the POM mechanism, it is of great significance to further elucidate the reaction from a microscopic perspective. Mhadeshwar and Vlachos[222] developed a thermodynamically consistent C1 microkinetic model for POM, SRM, DRM, and oxygenate decomposition on Rh using a hierarchical multiscale methodology with parameters obtained from combined UBI-QEP and DFT calculations. The model predicted distinct oxidation and reforming zones, where CO and H_2O were the primary products that existed in the oxidation zone. H_2 was produced from methane reforming by H_2O generated in the oxidation zone. Matteo *et al.*[223] integrated a microkinetic model[224] with detailed reactor models[225] to investigate the dominant reaction pathways for syngas production in POM on Rh. Three reaction zones were suggested: deep combustion of a methane zone (O* is the most abundant reactive intermediate), followed by a zone where both direct formation of synthesis gas and catalytic combustion occur, and, finally, a SRM and WGS zone (oxygen is no longer available). Zone II and zone III were supported by the microkinetic study of spatially resolved autothermal POM experiments reported by Donazzi *et al.*[226] over Rh-coated foams. Besides, the reaction pathway analysis of Donazzi *et al.*[226] showed that methane was activated *via* pyrolytic decomposition, and the main oxidizer was OH* rather than O*. In the oxidation zone (zone II), OH* was generated from O* and H* combination, while in the reforming zone (zone III), OH* was formed by H_2O dissociation.

Mhadeshwar and Vlachos[214] developed a predictive CH_4 (C1) mechanism on Pt by using a hierarchical multiscale approach. They concluded that POM on Pt was indirect, where total oxidation occurred first to form CO_2 and H_2O, followed by SRM and DRM to generate CO and H_2, consistent with modeled experimental data. The combined kinetic and DFT studies of CH_4 oxidation on Pt and Rh clusters by Chin *et al.*[227] confirmed that POM to CO and H_2 followed an indirect mechanism at the molecular scale. CO and H_2 were predominantly produced upon complete O_2 consumption from the sequential reforming steps. Based on the above kinetic and microkinetic studies, it is generally accepted that there is no unified mechanism of POM to synthesis gas and that even for the same catalyst the process might follow different reaction routes depending on the reaction conditions and the state of the catalyst.

Au *et al.*[228] gave a detailed theoretical study of POM to synthesis gas on Ni, Pd, Pt and Cu catalysts, where adsorption energies were calculated using the Amsterdam density functional (ADF) program system, and activation energies were estimated by the UBI-QEP method. These metals were simulated by Ni_7, Pd_{10}, Pt_{10}, and Cu_{10} clusters. The calculated total methane dissociation energies followed the trend of Ni < Pd ≈ Pt, corresponding to the experimental tendency in methane conversions as Ni > Pd ≈ Pt. The rather high activation energy of discrete dehydrogenation steps on Cu explains why Cu is not active for methane dissociation. C* + O* → CO* was the RDS on Ni due to the higher activation energy than those of dehydrogenations ($CH_{x,s} \rightarrow CH_{x-1,s}$). On the other hand, on Pd, Pt, and Cu, CH* dissociation (CH* → C* + H*) was the RDS because of the highest activation energies. The calculation also indicated that gas-phase CO could easily combine with O* to form CO_2. The CO_2 selectivity was, therefore, dependent on the amount of adsorbed O* present on the surface. High CO selectivity can be obtained in an oxygen-depleted environment.

Metal dependence of the activity. Like SRM, POM reaction is active on noble metals such as Rh, Ru, Ir, Pt, and Pd, with Rh and Ru being the most active, and on non-noble metals like Ni and Co.[38,42,70,210,211] For non-noble metal catalysts, Ni-based catalysts display the highest activity, which is even comparable to that of noble metal catalysts.[42] Nevertheless, rapid catalyst deactivation caused by carbon deposition as well as loss and sintering of Ni under POM reaction conditions is a major problem that occurred on Ni-based catalysts.[141] Consistent with the mechanism of POM with total oxidation followed with SRM, the activity order of POM on these metals is similar to that of SRM, namely Rh ≈ Ru > Ni ≥ Ir ≥ Pt, Pd,[48,127,210] which has been discussed in Section 2.2.1. The relative order of carbon formation was observed as Ni > Pd ≫ Rh, Ru, Ir, Pt, reported by Claridge and Battle *et al.*[48,229]

Yoo *et al.*[95] employed DFT and microkinetic modeling to investigate methane oxidation to CO, CO_2, CH_2O, and CH_3OH over a Pd(111) surface under mildly oxidizing conditions. CO and CH_2O were found to be the main products. The CO selectivity was greater than 0.5 and normally increased with increasing temperature, while the CH_2O selectivity was less than 0.4 with a maximum at 550 K. In addition to Pd(111), the authors also extended the study to other metal fcc(111) surfaces by employing linear scaling relations in the microkinetic model. The obtained volcano plots of the product reaction rates are given in Fig. 16. Pd, Pt, and Rh(111) surfaces were selective to CO and/or CH_2O productions, where the metallic site led to CO production, and the surface O* site led to CH_2O production. Ag, Au, and Cu(111) surfaces were selective to CH_2O and/or CH_3OH productions, with the O*-assisted mechanism preferred for all dehydrogenation steps.

Catalysts improving carbon formation resistance. Like SRM and DRM, carbon deposition is a commonly encountered phenomenon occurring in the POM process that results in catalyst deactivation, especially for Ni-based catalysts. The application of bimetallic catalysts could effectively reduce the carbon deposition problem and sometimes also improve the catalyst activity. For instance, the DFT calculations of He *et al.*[230] revealed an improved performance of Ni by alloying it with Co, which enhanced both catalyst activity and carbon formation resistance for methane oxidation. Alloying Ni with Cu could also improve the catalyst carbon formation resistance but with reduced activity as a cost.

Concerning direct partial oxidation to synthesis gas, theoretical studies mainly focus on single-atom alloy (SAA) catalysts rather than traditional bimetallic catalysts. Zhang *et al.*[141] investigated the effect of Ni(111) alloying with Pt on this

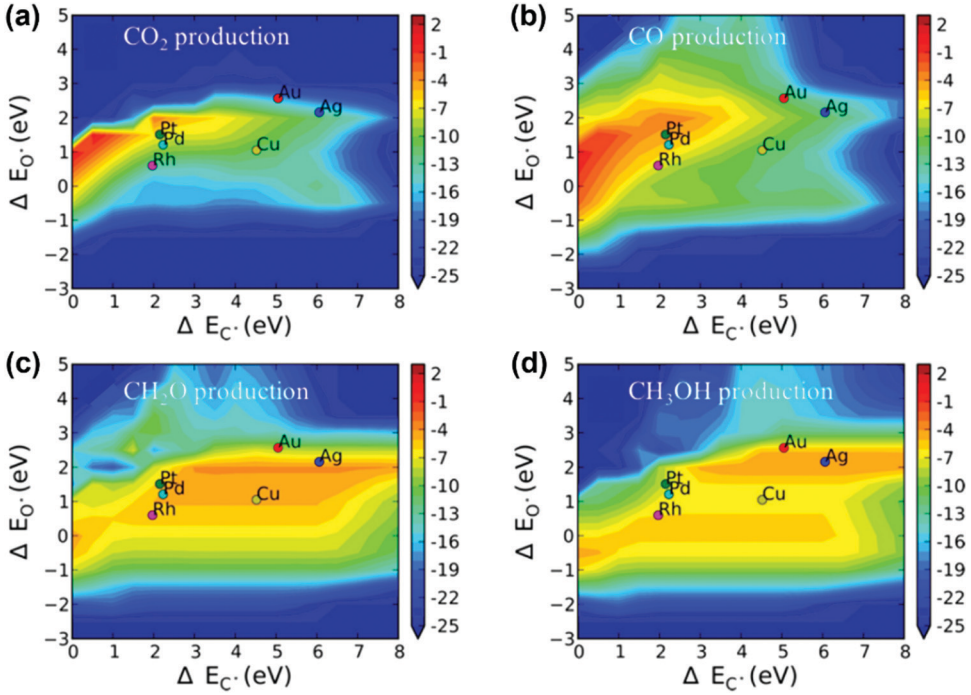

Fig. 16 Logarithms of the calculated production rates (s^{-1} per site) of (a) CO_2, (b) CO, (c) CH_2O, and (d) CH_3OH during CH_4 oxidation at T = 523 K, P_{CH_4} = 0.91 bar, P_{O_2} = 0.11 bar, P_{H_2O} = 0.02 bar, and P_{H_2}, P_{CH_3OH}, P_{CH_2O}, P_{CO}, and P_{CO_2} = 10^{-39} bar. ΔE_C and ΔE_O are taken relative to gas-phase CH_4, H_2O, and H_2.[95] Reproduced from ref. 95 with permission from the American Chemical Society, copyright 2018.

reaction *via* a DFT study. It was found that by doping Pt on Ni(111) methane dissociation was greatly promoted. However, the activation energy of CO formation (RDS: CH + O → CHO) and that of H_2 formation (H + H → H_2) were both observed to increase on the NiPt(111) surface, indicating that alloying Ni(111) with Pt might cause suppressed CO and H_2 production. The results demonstrated that NiPt bimetallic catalysts were beneficial to methane adsorption and dissociation and atomic C/H adsorption, but might be less favorable for synthesis gas formation.[71,141]

Meng *et al.*[90] investigated POM to synthesis gas over a D-Pd/Cu(111) (doped Pd/Cu(111)) catalyst and over an A-Pd/Cu(111) (adsorbed Pd/Cu(111)) catalyst *via* DFT calculations. Through comparison, the D-Pd/Cu(111) catalyst showed more thermodynamic stability and exhibited a higher capacity for sintering resistance. In their other study,[231] Pt was doped on Cu(111) and Ni(111) surfaces to understand the bimetallic catalyst activity and coke-resistance during POM using DFT calculations. Fig. 17 gives a comparison of methane dissociation reaction pathways on Cu(111), Ni(111), $Pt_1Cu(111)$ and $Pt_1Ni(111)$ surfaces. The activation barriers of CH_4 dissociation were largely reduced by the introduction of a single Pt atom on the Cu(111) surface. Compared to $Pt_1Ni(111)$ and Ni(111), $Pt_1Cu(111)$ displayed similar activation barriers of CH_4 dissociation to CH_3, but a higher barrier of CH dehydrogenation to C. These results indicated that $Pt_1Cu(111)$ can effectively promote methane activation, but not affect the excellent coke resistance. Towards CO formation, the dominant pathway was CH → CHO → CO on both $Pt_1Cu(111)$ and $Pt_1Ni(111)$, with CH + O → CHO as the RDS. The lower activation energy of CH + O → CHO on $Pt_1Cu(111)$ than on $Pt_1Ni(111)$ illustrated a higher potential of CO formation on $Pt_1Cu(111)$, which prevented C formation and resulted in a better coke-resistance. The performance of the Pt single-alloy Cu catalyst was significantly enhanced, compared with that of commercial Ni-based catalysts.

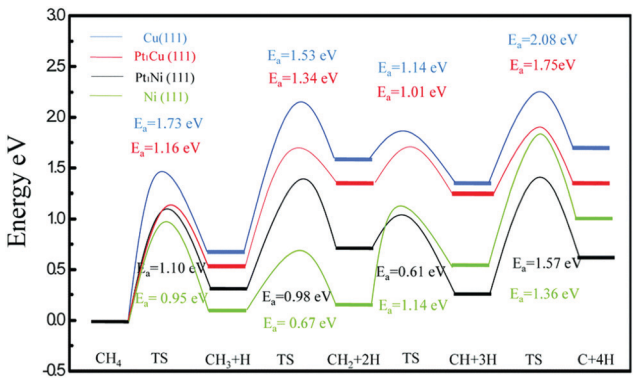

Fig. 17 Comparison of methane dissociation reaction pathways on $Pt_1Cu(111)$ and $Pt_1Ni(111)$ surfaces.[231] Reproduced from ref. 231 with permission from the Centre National de la Recherche Scientifique (CNRS) and the Royal Society of Chemistry, copyright 2020.

In addition to bimetallic catalysts, the employment of supports could also effectively improve the performance of the catalysts. Guo *et al.*[232] investigated methane dissociation and partial oxidation on Rh_4/Ana-Ov (oxygen-defective anatase TiO_2 supported Rh) and Rh_4/Rut-Ov (rutile TiO_2 supported Rh) by DFT, with emphasis put on carbon deposition resistance. Rh_4/Ana-Ov showed a higher activation barrier of C–H bond

breaking in methane decomposition and a lower energy barrier of $CH_2 + O \rightarrow CH_2O$ (RDS for CO formation) compared to that on Rh_4/Rut-Ov, implying a strong carbon deposition resistance and a high synthesis gas formation activity of the Rh_4/Ana-Ov catalyst. The microkinetic modeling of Rh_4/Ana-Ov illustrated a high (up to 90%) CO selectivity, which was increased with temperature. In another study of Guo *et al.*,[233] DFT calculations were used to analyze the size-dependent carbon deposition resistance of Rh-clusters supported on anatase (Rh_x/Ana-Ov) for POM. Rh_1/Ana-Ov, Rh_4/Ana-Ov, and Rh_{13}/Ana-Ov were applied to simulate different cluster sizes. It was found that Rh_1/Ana-Ov displayed a much higher apparent energy barrier of methane dissociation and lower energy barrier of $CH_2 + O \rightarrow CH_2O$ (RDS for CO formation) among the three models, which could be the one owing to the strong carbon deposition resistance and high catalytic activity. Therefore, SAA catalysts were suggested as candidates to reduce carbon deposition for POM processes.

Size dependence of activity. The kinetic study of Kondratenko *et al.*[210] investigated the size effect on activity and selectivity for POM to synthesis gas over γ-Al_2O_3 supported Rh NPs. As the particle size increased, the methane conversion and H_2/CO ratio were decreased. Meanwhile, the apparent TOF of CO formation and CO selectivity were strongly reduced, indicating a size-dependent kinetics of this process on the supported Rh NPs. However, the overall mechanism of POM was size-independent, which mainly followed an indirect (CRR) mechanism through methane combustion and reforming to form CO and H_2.

According to the above kinetic, DFT and microkinetic studies, the mechanism of POM to synthesis gas is still under debate. The exothermic property of POM reaction makes it a challenge to elucidate the reaction mechanism. Nevertheless, owing to the potential of POM in methane conversion, there is a great possibility to attract more attention to this process in the future.

2.3 Methane conversion on oxides

There are extensive pieces of literature on methane activation over various oxide catalysts, some of which have been reviewed previously[39,63,234–239] and among which methane oxidation was found to be the most studied reaction. Methane oxidation catalysis involves the introduction of methane and gaseous molecular oxygen into the reactor. Since both the adsorbed oxygen from the gas phase and lattice oxygen from the oxide catalyst can possibly participate in the reactions, it is essential to understand the relative role between them. It was earlier proposed that, instead of the adsorbed oxygen from the gas phase, the concentration of lattice oxygen controls the selectivity of the metal oxide catalyst for total oxidation.[239,240] This opinion is consistent with the MVK mechanism.

As early as 1993, Otsuka *et al.*[241] reported that CeO_2 could be used as an oxidant to transform methane into synthesis gas with a H_2/CO ratio of 2 at 873–1073 K. During the redox cycle of cerium oxide, methane was directly converted to CO and H_2, and CeO_2 was partially reduced to CeO_{2-n}, as shown in eqn (6):

$$CeO_2 + nCH_4 \rightarrow CeO_{2-n} + nCO + 2nH_2 \quad (6)$$

The reduced CeO_{2-n} could be used to convert CO_2 into CO, with oxygen recovery to CeO_2, as shown in eqn (7):

$$CeO_{2-n} + nCO_2 \rightarrow CeO_2 + nCO \quad (7)$$

The addition of Pt to CeO_2 accelerated the formation of synthesis gas, while the H_2/CO ratio became higher than 2 when the reduction of the Pt-doped CeO_2 catalyst was over 60 min, which implied coke formation on the cerium oxide surface after a period of reduction.

Encouraged by experimental results on CeO_2 oxides, methane oxidation has been studied by DFT calculations on CeO_2,[110,242] and CeO_2 doped with Zr or Pd,[110,242,243] and Pt.[113] As discussed in Section 2.1.2, the C–H bond activation of methane is well correlated with the surface reducibility of CeO_2 measured by the formation energy of O vacancy. A comparative study of methane oxidation was performed by a DFT+U on $Pd_xCe_{1-x}O_2(111)$, $CeO_2(111)$ and PdO(100) surfaces.[242] The reaction mechanism is similar to that on transition-metal surfaces, where methane oxidation took place *via* $CH_4 \rightarrow CH_3^* \rightarrow CH_2^* \rightarrow CH^* \rightarrow HCO^* \rightarrow CO^* \rightarrow CO_2$ at low coverage as shown in the free energy diagrams in Fig. 18. C–H bond activation in methane is the RDS on all three surfaces. Carbon formation was not favored over any surface, and the formation of POM products was also not thermodynamically favorable, which, however, was different from the results obtained by Otsuka *et al.*[241] that synthesis gas was the primary product on the CeO_2 surface.

Importantly, doping CeO_2 with Zr or Pd,[110,242,243] and Pt[113] decreased the formation energy of O vacancy of the neighboring oxygen atoms and thus reduced the C–H activation energy barrier. Doping with metals is an effective method to increase the activity of C–H bond activation. The methane activation barrier was the lowest on the $Pd_xCe_{1-x}O_2(111)$ surface, lower than those on $CeO_2(111)$, PdO(100), and Pd*/$CeO_2(111)$, and even lower than those on Pd(111) and stepped and kinked Pd(211) surfaces.[243]

Jin *et al.*[244] conducted experimental and theoretical studies of oxidation of ventilation air methane on Fe_2O_3 and CuO catalysts. The mechanism schematics of CH_4 oxidation on the two surfaces are given in Fig. 19(a), together with calculated reaction energies. They implied that CH_4 dissociation was the RDS, with reaction energies as 2.76 eV for $Fe_2O_3(0001)$ and 0.47 eV for CuO(110), due to the strong C–H bonding. It also revealed that the oxygen vacancy (OV) could recover quickly when additional O_2 molecules reached the metal oxide surface conducting adsorption and dissociation. Therefore, the reduction of Fe_2O_3 and CuO could rarely occur, which remained stable without transition to the reduced phase. The schematic configurations of surface bonding for methane oxidation on the O-terminated $Fe_2O_3(0001)$ are presented in Fig. 19(b). An OV was generated when H_2O was released

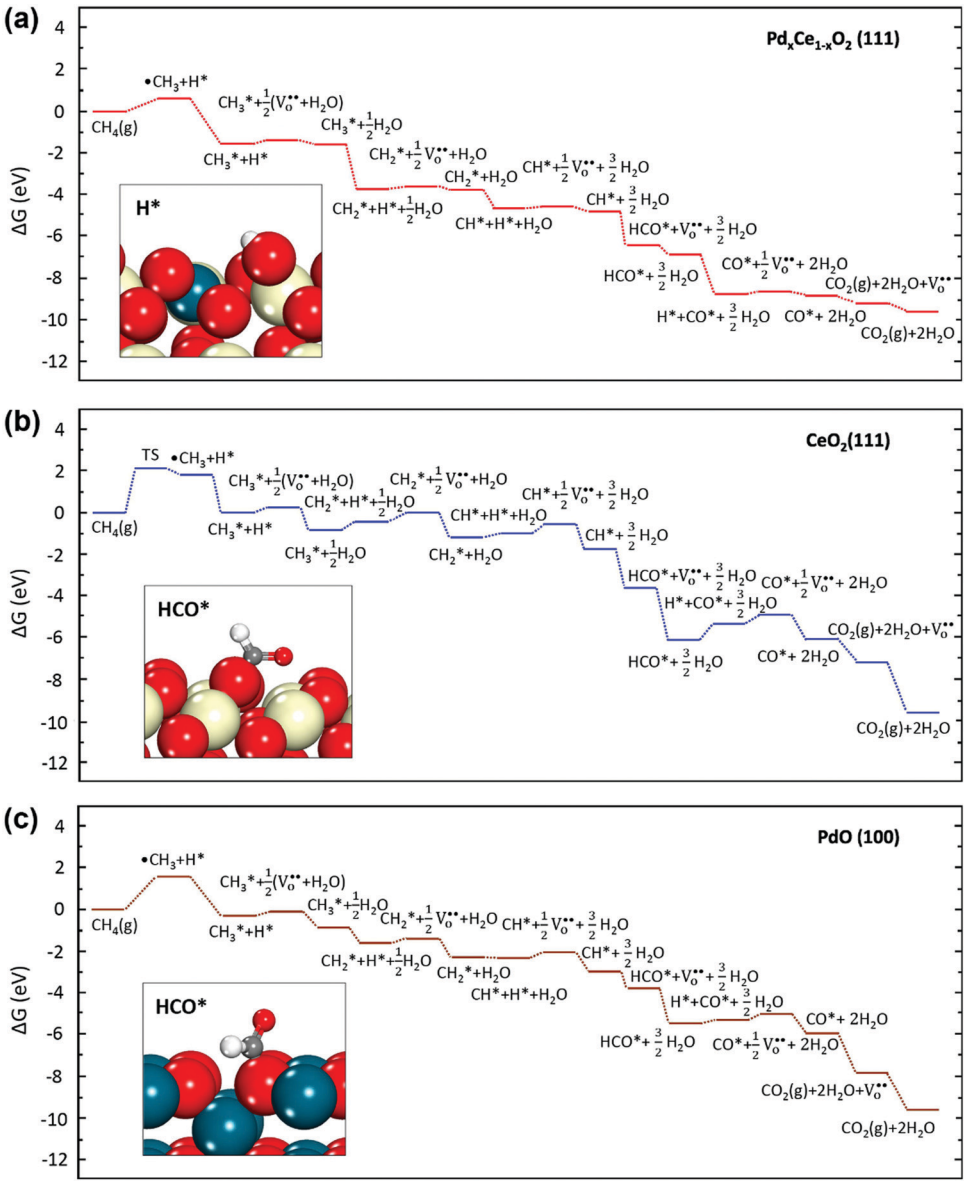

Fig. 18 Reaction free energy diagrams for $CH_4(g) + 2O_2(g) \rightarrow CO_2(g) + 2H_2O(g)$ over (a) $Pd_xCe_{1-x}O_2(111)$, (b) $CeO_2(111)$ and (c) PdO(100) at T = 298 K and P_{CH4} = 0.01 atm, P_{O2} = 0.04 atm, $P_{H2O} = P_{CO2} = 10^{-6}$ atm. Insets show the most stable intermediates in methane oxidation over the three surfaces. Ce is displayed as tan (light), Pd as light blue (gray), O as red (dark), and H as white.[242] Reproduced from ref. 242 with permission from Elsevier, copyright 2011.

(Fig. 19b(A–C)), followed by O_2 filling in the OV to generate –Fe–O–O (Fig. 19b(D)). The formation of C–O bonding in Fig. 19b(F) was favorable to activate the C–H bond of CH_x due to the spontaneous transfer of the C–O single bond to the C═O double bond with the breakage of C–H. The DOS profiles in their work showed that OVs generated more local states over reduced metal surfaces, which were the active sites for O_2 adsorption and thus made the C–H activation and O_2 splitting more feasible. The under-coordinated metal atoms and OVs could stabilize CH_x radicals to promote CH_4 dissociation (RDS), which are therefore essential for potential high-performance CH_4 oxidation catalysts.

In addition to the above metal oxide catalysts, IrO_2 was also reported to be an effective catalyst to activate the C–H bond of methane.[245] According to the DFT study of Yeh *et al.*,[246] formaldehyde formation was the most favorable reaction for methane oxidation. The reaction was limited by formaldehyde desorption, with a desorption energy of 1.10 eV on an $IrO_2(110)$ surface, and the reaction barrier was lower than 0.70 eV. An external electric field was employed to modify the reactivity of $IrO_2(110)$, which was found to have no apparent influence on methane dehydrogenation and C–O coupling but could regulate the desorption energy of the adsorbates, especially promoting methane oxidation to formaldehyde over an O-rich $IrO_2(110)$ surface.

Despite the most cases that lattice O was favorable for methane oxidation, surface oxygen adsorbed or "activated" O played an important role in the POM reaction on oxides with

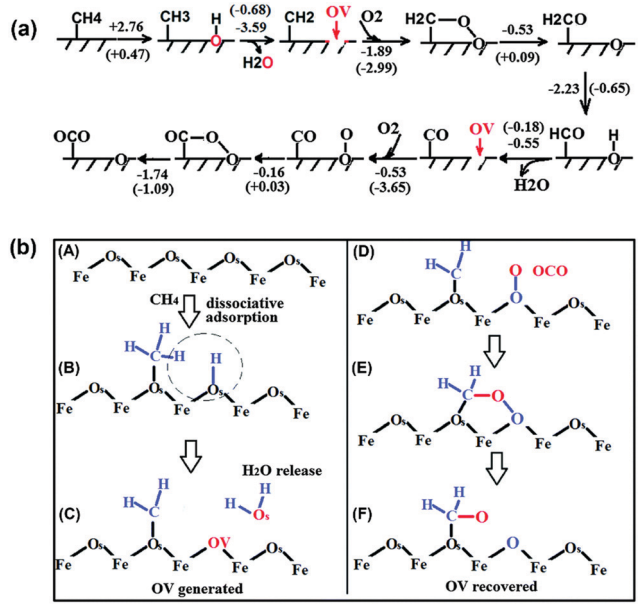

Fig. 19 (a) Mechanism schematics of CH_4 oxidation on the surfaces of Fe_2O_3 and CuO under the reaction atmosphere with abundant oxygen, together with calculated reaction energies in units of eV. Two values of the reaction energy are labelled for each elementary reaction: one is for Fe_2O_3, and the other given in the parentheses is for CuO. Red O indicates that the oxygen is from Fe_2O_3 or CuO, rather than adsorbed O_2. (b) Schematic configurations of surface bonding for CH_4 oxidation on the O-terminated Fe_2O_3(0001) surface. (A–C) show the generation of an OV, and (D–F) describe the recovery of the OV from O_2 dissociative adsorption. O_s represents the surface oxygen and OCO denotes one-coordinated oxygen.[244] Reproduced from ref. 244 with permission from the PCCP Owner Societies, copyright 2015.

high formation energies of oxygen vacancy, such as MoO_3(100)[247] and SiO_2 surfaces.[248]

Perovskite oxides (ABO_3) have stimulated interest in various redox cycle reactions (*e.g.* methane oxidation) due to their excellent crystal structure and redox reversibility.[249–251] Methane oxidation has been studied on $LaFeO_3$ based perovskites by DFT calculations focused on the active sites and oxygen mobility and their effects on catalyst activity and selectivity.[252,253] The mechanism and structure requirements of selective and total oxidation of methane in a chemical looping process are both experimentally and theoretically examined on $La_{0.5}Sr_{0.5}Fe_{1-x}Co_xO_{3-\delta}$ perovskites. The substitution of Sr for La at the A site and the substitution of Co for Fe at the B site of the ABO_3 perovskites significantly reduced the formation energy of oxygen vacancy. The lattice O diffusion rate and the activity of methane conversion increased, and the selectivity decreased upon decreasing the formation energy of oxygen vacancy. The formation energy of oxygen vacancy increased upon increasing the lattice oxygen charge. Recently, Zhang *et al.*[252] employed combined electrical conductivity relaxation measurements and DFT calculations to study the influence of FeO_6 octahedral distortion on lattice oxygen in $La_{1-x}Ce_xFeO_3$ perovskites for POM coupled with a CO_2 splitting process. It was found that changing the content of Ce_{3+} substitution in $La_{1-x}Ce_xFeO_3$ (x = 0, 0.25 0.5, 0.75, 1) resulted in a change in Fe–O bond-length variance, which could tune the FeO_6 octahedral distortion degree in $La_{1-x}Ce_xFeO_3$, activate the lattice oxygen and significantly improve the catalysts' performance in chemical looping POM-CO_2 splitting.

Methane oxidation on spinel structured oxides such as $CaFe_2O_4$[254] and $NiCo_2O_4$[255] was studied experimentally and theoretically. The deep reduction of calcium ferrite facilitated the production of synthesis gas through methane dehydrogenation and selective oxidation of C to CO. The mechanism difference of POM to form CO and H_2 with the $CaFe_2O_4$ carrier can be associated with the differences in the oxide phases existing during the reduction process, oxygen species concentration, and bonding in the lattice structure.[254] The metal total combustion on $NiCo_2O_4$ was observed to follow (1) O_2 dissociation on surface O vacancies; (2) the dissociated O atoms filled into O vacancies and coupled with H atoms to form OH and H_2O; (3) CH_4 dissociation to form CH_3* on Ni cations with a subsequent oxidation to CH_3O*; (4) CH_3O* dehydrogenation to form CH_2O* with a subsequent ODH (with the O species of the nearby Co site) to form CHO*; and (5) transformation of CHO* to products (CO_2 and H_2O) *via* two subpathways including OCHO dehydrogenation and CO oxidation. The high activity of $NiCo_2O_4$ in CH_4 conversion to H_2O and CO_2 at a relatively low temperature together with its low cost leads to $NiCo_2O_4$ being very promising for the removal of CH_4 in the exhaust gas of a natural gas engine through complete oxidation.

Unlike the extensive literature reported for methane oxidation, only a few theoretical studies have been conducted for SRM and DRM reactions on oxide catalysts, such as SRM on a $Ce_{0.90}Ni_{0.05}Ru_{0.05}O_2$ (CNR) catalyst,[256] and DRM on Rh-substituted lanthanum zirconate pyrochlore (LRhZ),[257] NiO–MgO,[258] and Ni–CaO.[259] In SRM and DRM, the metal oxides are normally used as supports to favor possible H_2O[92,200,260,261] or CO_2 activation[40,189,262,263] coupled with methane activation on transition metal surfaces. The relatively high activity and low cost of Ni-based catalysts, as well as good performance of other metal catalysts for SRM and DRM, make the research mainly focused on metal surfaces.

3. C–H bond activation in ethane

Ethylene is the most critical chemical building block which could be applied to synthesize various downstream products. It can be produced by noncatalytic thermal dehydrogenation, catalytic dehydrogenation, and oxidative dehydrogenation. Steam cracking is still the dominating route for industrial production of ethylene, but other technologies have also gained increasing attention. Several excellent reviews have addressed the progress in ethane dehydrogenation and oxidative dehydrogenation of ethane.[3,264–273] Here we summarize the progress of theoretical catalysis on C–H activation of ethane.

3.1 Ethane dehydrogenation on metal surfaces

Ethane is physisorbed on various metal and metal oxide surfaces, and the composition of the catalyst changes the physisorption very much. The C–H bond activation of ethane

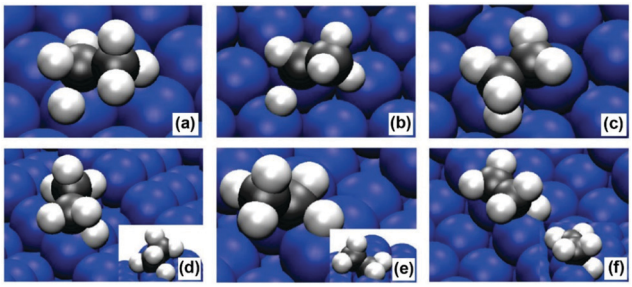

Fig. 20 Geometries of the transition states for the activation of ethane and ethyl C–H bonds on Pt(111): (a) CH_3CH_2–H, (b) CH_3CH–H, and (c) CH_2CH_2–H; and on Pt(211): (c) CH_3CH_2–H, (d) CH_3CH–H, and (e) CH_2CH_2–H.[279] Reproduced from ref. 279 with permission from the American Chemical Society, copyright 2010.

is similar to the C–H activation of methane and follows the universal scaling relationship of the activation energy of C–H activation of light alkanes. The C–H activation of ethane deals with the secondary C sp^3–H bond cleavage. The C–H activation energy of ethane is generally lower than the one of methane, due to the weaker strength of 2° than 1° C–H bonds.

3.1.1 Reaction mechanism. The exact reaction mechanism of dehydrogenation of ethane is still under debate, due to the fact that a large variety of materials can catalyze this reaction. The 4 step Horiuti–Polanyi mechanism is commonly used to describe the dehydrogenation mechanism on metal surfaces.[274] It consists of 4 main steps: dissociative adsorption of alkanes, C–H cleavage of a second hydrogen atom, the formation of a hydrogen molecule, and subsequent desorption of both the hydrogen and the olefin. Both the dissociative adsorption of ethane and C–H cleavage of a second hydrogen atom[275–277] have been suggested as the RDSs. Pt is the most active pure metal for ethane dehydrogenation to produce ethylene, due to its superior activity towards C–H bond activation and low activity towards C–C bond cleavage.[278] On the Pt surface, it is generally accepted that the reaction goes through ethane dehydrogenation to ethyl, CH_3CH_2*, then to ethylene, while the non-selective pathway to methane and deeply dehydrogenated species is predicted to go through dehydrogenation *via* CH_3CH*.

The geometries of the transition states for activation of ethane and ethyl C–H bonds on Pt(111) and Pt(211) surfaces are shown in Fig. 20, with the corresponding activation barriers summarized in Table 1.[279] The C–H bond activation of ethane on both surfaces occurs through the simultaneous interaction of C and H with a surface Pt atom, forming a C–Pt–H three-membered ring structure (Fig. 20a and d). The C–Pt–H three-membered ring structures are also found in ethyl to ethylene on both surfaces (Fig. 20c and f) and ethyl to CH_3CH* on the Pt(211) surface (Fig. 20e). For the transition states of ethyl to CH_3CH* on the Pt(111) surface, ethyl is bonded to Pt surfaces *via* the C atom, where the H in C–H is bonded to adjunct Pt (Fig. 20b). The energy barriers of the three steps follow the order Pt(211) < Pt(111), as shown in Table 1. Similarly, the energy barriers of Pt(433) step < Pt(433) terrace,[280] and Pt_{55} < Pt(111)[281] are obtained. The stepped Pt surfaces (or small Pt particles) having coordinatively unsaturated Pt atoms are therefore kinetically more active for the dehydrogenation of ethane to form ethylene than the flat surfaces.

In addition to activity, ethylene selectivity is another important factor in characterizing ethane dehydrogenation. From Table 1, one can see that the energy barrier of CH_3CH_2* → CH_3CH* is lower than that of CH_3CH_2* → CH_2CH_2* for both the Pt(211) and Pt(433) steps. It means that these under-coordinated step sites preferably promote deep dehydrogenation, resulting in coke formation and catalyst deactivation.[280] By decorating the step with AlO_x species (Al_6O_{11} decorated Pt(433)), the step sites can be blocked, leading to suppression of deep dehydrogenation and coke formation. The deep hydrogenation can also be suppressed by doping Pt with Sn. As shown in Table 1, Pt–Sn surface alloys with different site coverages of Sn and Pt–Sn bulk alloy have been investigated for ethane dehydrogenation *via* DFT calculations.[282–284] The activation energies of the first and second C–H bond cleavage steps for ethylene formation were calculated as Pt(111) < Pt_3Sn(111) (bulk alloy) < Pt_3Sn/Pt(111) (surface alloy) < PtSn/Pt(111) (surface alloy). The addition of Sn into Pt increases the C–H and C–C bond cleavage barriers, which inhibits the catalyst activity but favors ethylene selectivity over carbon formation.

Table 1 Calculated energy barriers (E_{act}) for ethane and ethyl dehydrogenation on different metal surfaces

	E_{act} (eV)						
Surface	CH_3CH_3(g) → CH_3CH_2*	CH_3CH_2* → CH_3CH*	CH_3CH_2* → CH_2CH_2*	XC functional	*k* points	Unit cell	Ref.
Pt(111)	0.54	0.88	0.81	PBE	5 × 5 × 1	2 × 2	279
Pt(211)	0.08	0.27	0.44		3 × 4 × 1	2 × 1	
Pt(110)-(1 × 2)	0.38	0.33	0.29	PW91	—	2 × 2	285 and 286
Pt(433) terrace	0.65	0.81	0.71	PW91	1 × 2 × 1	1 × 3	280
Pt(433) step	0.33	0.08	0.27				
Al_6O_{11} decorated Pt(433)	0.69	0.78	0.73				
Pt(111)	0.84	—	0.67	PBE	3 × 3 × 1	4 × 4	281
Pt_{55}	0.57	—	0.48		1 × 1 × 1	—	
Pt(111)	0.91	0.91	0.89	PW91	6 × 6 × 1	2 × 2	282 and 283
Pt_3Sn/Pt(111)	1.19	1.04	1.07				
PtSn/Pt(111)	1.58	1.28	1.28				
Pt(111)	0.90	0.95	0.88	PW91	6 × 6 × 1	2 × 2	284
Pt_3Sn/Pt(111)	1.18	1.30	1.08				
Pt_3Sn(111)	1.08	0.84	0.88				

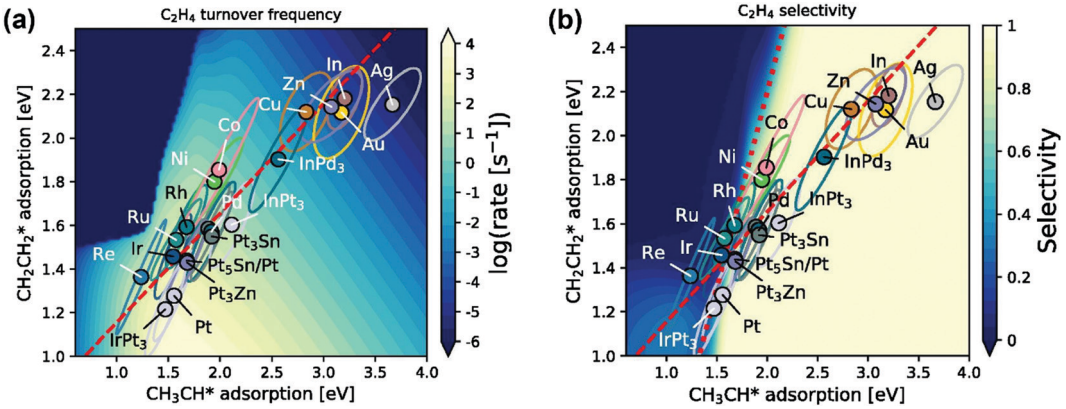

Fig. 21 (a) Activity volcano for ethylene production at 873 K, 0.2 bar C_2H_6(g), 2×10^{-4} bar C_2H_4 (1% carbon conversion), 0.6 bar H_2(g), and 10^{-9} bar CH_4 and 10^{-12} bar C_2H_2. (b) Map of carbon-specific selectivity.[287] Reproduced from ref. 287 with permission from Elsevier, copyright 2019.

A more detailed discussion on the site coverage of Sn and the location of the Sn on Pt catalyst for ethane dehydrogenation can be seen in Section 3.1.2.

Nørskov and co-workers[287] developed a descriptor based microkinetic model for ethane dehydrogenation over close-packed metal surfaces and varied reaction conditions. The C_2H_4 turnover frequency and selectivity can be predicted as functions of the adsorption energies of two key intermediates CH_3CH* and CH_2CH_2*. The model results showed that Pt and Pt alloys were among the most active catalysts for ethane dehydrogenation, as shown in Fig. 21(a). The catalytic activity followed the order $IrPt_3 \approx Pt > Re > Ir > Ru > Rh > Ni$, Co, while Cu, Zn, Au, In, and Ag were almost inactive. The Sn–Pt and Zn–Pt alloys showed reasonable activity, but it was lower than that of Pt. The Sn and Zn alloyed with Pt lowered the adsorption strength of CH_2CH_2*, and thus significantly enhanced ethylene selectivity, as shown in Fig. 21(b). The activity trend predicted by micro-kinetic modeling is in general agreement with experimental results.

Bell and co-workers[288] applied tetrahedral metal clusters in DFT calculations to represent metal NPs to study the elementary processes involved in ethane dehydrogenation. The DFT estimated free energy activation barrier for the dissociative adsorption of ethane to present activity trend followed $Pt_3Sn > Pt_3Ir > Pt_4$, which agreed relatively well with the experimentally measured activity order. The same group investigated the effects of intermetallic interaction on alkane dehydrogenation systematically using Pt-based, subnanometer-sized alloy cluster catalysts.[289] The alloys were modeled with Pt_3X (X = Pd, Sn, Ge, Si, In, Ga, Au, Ag, Cu, and Ir). For all the alloy catalysts, the RDS was found to be the same, namely the first C–H bond cleavage. The activation energy of the first C–H cleavage on the alloy clusters was predicted to be in the order of $Pt_3Si < Pt_3Ge < Pt_3Sn < Pt_3Ir <$ Pt. No significant BEP relationship could be found with respect to atomic H or CH_3 group binding energy for the Pt alloys. However, the catalyst activity correlated well with the HOMO–LUMO gap of the clean catalyst. Smaller HOMO–LUMO gaps indicated higher activity due to the increased flexibility of the valence electron at the active site.

3.1.2 Effect of promoters on selectivity and deactivation. Unpromoted Pt catalysts suffer from low alkene selectivity and rapid deactivation due to coking. Both undesired phenomena are mainly a consequence of deep dehydrogenation of surface C_2H_4*, leading to C–C bond breaking.[275–277] Improvements of catalyst activity, selectivity, and stability can be achieved by alloying Pt with Sn and by adding hydrogen to the alkane feed.[277,282–284] Pt alloys have been widely studied both experimentally and theoretically. DFT calculations have been used to provide a molecular understanding of those promoters for improving ethylene selectivity and catalytic stability. Alloys of Pt with Sn, Zn, Ga, Ge, and In have been widely studied, and Pt–Sn is the most studied system. Experiments showed that Pt–Ir and Pt–Sn had higher ethylene selectivity than Pt, and Pt–Ir exhibited better stability to coke deposition than Pt–Sn.[288] Microkinetic modeling[287] and the cluster model[267,289] suggested a higher selectivity of Pt–Sn compared to Pt. However, the sub-nanometer cluster model[288,289] predicted the selectivity trend. The cluster model predicted a higher C–H cleavage activation energy of ethylene and thus high activation energy of C–C cleavage, which resulted in a high ethylene selectivity and better stability on Pt_3Ir than Pt, in good agreement with experimental observation.

The cluster model[289] predicted relatively high ethylene selectivity on Pt-based catalysts due to their relatively high barriers for direct C–C bond cleavage compared to C–H bond breaking. A natural bond orbital analysis revealed that the d-orbital shape of the HOMO with its pronounced nodal features better facilitated the breaking of a C–H bond than that of a C–C bond due to better overlap with the C–H anti-binding orbital.

The site coverage of Sn and the location of the Sn on Pt catalyst do influence the catalyst performances for ethane dehydrogenation.[282–284] Kinetic reaction barriers were calculated for potential energy surfaces of C1 and C2 intermediates from C–H and C–C bond cleavage of ethane with $\frac{1}{4}$ and $\frac{1}{2}$ surface monolayers of Sn.[282] Sn weakened the binding energies of all species at both coverages. At the lower Sn coverage ($\frac{1}{4}$ monolayer), the effect was purely electronic since the binding geometries had not changed compared to those on the Pt(111)

surface. At the higher coverage of Sn, a larger effect on reaction energies was observed due to the changes in the binding geometries as a result of the elimination of 3-fold hollow sites that consist of Pt atoms. In terms of the electronic effect, Sn can donate electrons to Pt atoms and reduce the binding energies of adsorbates to Pt and increase the barrier for C–H and C–C cleavage, as shown in Table 1. The increase in the barriers favors ethylene selectivity over carbon formation. The same group further studied the effect of tin in the bulk of PtSn alloys for ethane dehydrogenation.[284] DFT calculations were performed on pristine Pt(111), a Pt_3Sn/Pt(111) surface alloy, and a Pt_3Sn(111) bulk alloy. The binding energies of adsorbates weakened on both Sn alloys. But on the bulk alloy, the binding energy was weaker than that on pure Pt but stronger than that on the surface alloy. Therefore, the activity trend for ethylene formation was predicted as pure Pt > bulk alloy > surface alloy based on the activation energies of the first and second C–H bond cleavage steps (Table 1). A selectivity descriptor was defined for ethane dehydrogenation as the energy difference between the activation energy for ethylene dehydrogenation (E_a, $CH_2CH_2^* \rightarrow CH_2CH^*$) and the desorption energy of ethylene (ΔE_{des}, $CH_2CH_2^*$) for several substitutional surface alloys. A smaller value indicates that further ethylene dehydrogenation is more favored over desorption and therefore predicts poor selectivity towards ethylene. The selectivity descriptor was calculated as −0.12, 0.04, and +0.36 eV for Pt, the bulk alloy, and the surface alloy, respectively. Therefore, the ethylene selectivity was highest on the surface alloy, followed by the bulk alloy and pure Pt.

The selectivity descriptor has been used to study a broader range of Pt–M surface alloys at low and high M coverages, including metals from groups 7–15.[283] The Pt_3M/Pt(111) alloy surface was created by replacing one surface Pt atom with alloying element M, giving 1/4 ML surface coverage for M. There were two types of 3-fold hollow sites, namely Pt_3 and Pt_2M sites on Pt_3M/Pt(111) surfaces. A PtM/Pt(111) surface was created by replacing two surface Pt atoms with M, giving 1/2 ML surface coverage for M. On the PtM/Pt(111) surface, the 3-fold Pt_3 sites were removed, and 3-fold binding sites included Pt_2M and PtM_2 sites. 27 elements (M) were selected for this study, which comprised the TMs from groups 7–11 and the post-transition (P-T) metals from groups 12–15. The P-T metals included Zn, Cd, Hg, Al, Ga, In, Tl, Ge, Sn, Pb, Sb, and Bi. The TMs were further classified as nonpreferred transition (NT) metals and carbon-preferred transition (CT) metals based on the preferred binding site of a carbon atom (Fig. 22a).

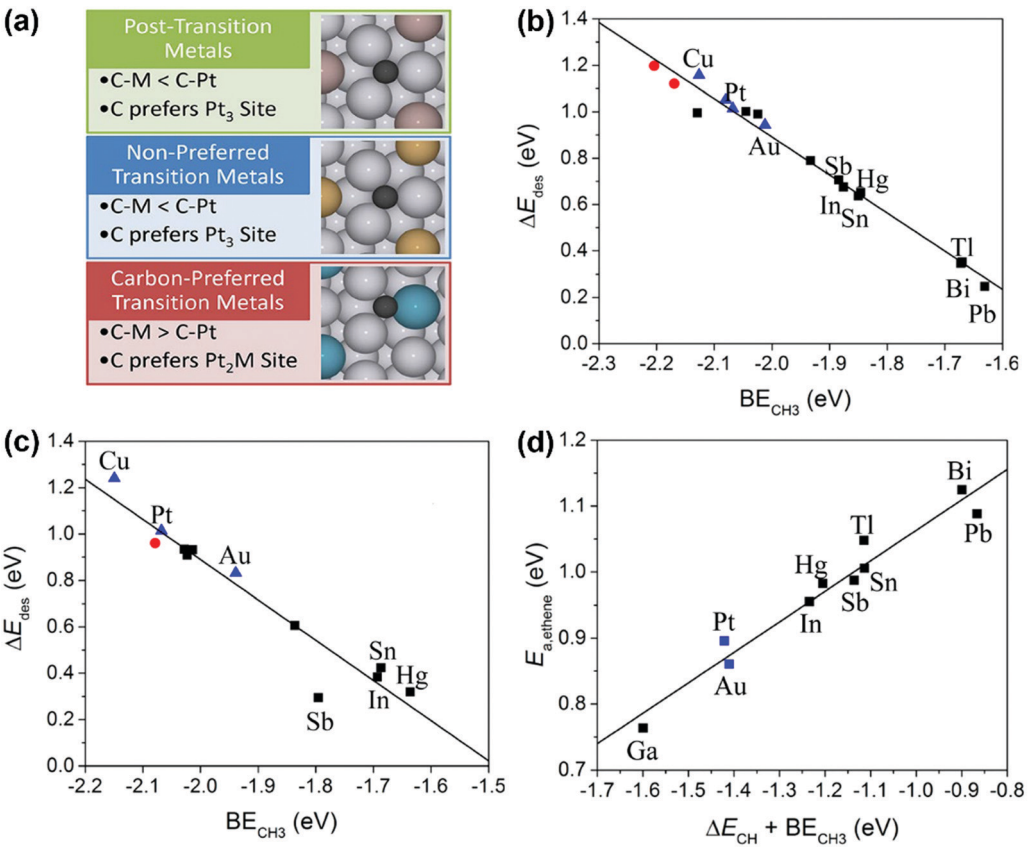

Fig. 22 (a) Binding site preferences of carbon atoms on three categories of alloying elements: post-transition (P-T) metals, nonpreferred transition (NT) metals, and carbon-preferred transition (CT) metals. Relationships between the methyl binding energy (BE_{CH3}) and the desorption energy of ethylene (ΔE_{des}) at (b) $\frac{1}{4}$ ML and (c) $\frac{1}{2}$ ML coverage. (d) Relationships between the methylidyne dehydrogenation reaction energy (ΔE_{CH}) plus methyl binding energy (BE_{CH_3}) and the ethylene dehydrogenation barrier (E_a, ethylene) for alloys at $\frac{1}{4}$ ML coverage. NT alloys in blue, P–T alloys in black, and CT alloys in red.[283] Reproduced from ref. 283 with permission from the American Chemical Society, copyright 2017.

NT metals were transition metals where a carbon atom placed on $Pt_3M/Pt(111)$ preferred to bind on Pt_3 sites. Conversely, the transition metals where C preferred to bind on Pt_2M sites over $Pt_3M/Pt(111)$ were labeled CT metals. The NT metals included Mn, Fe, Co, Ni, Pd, (Pt), Cu, Ag, and Au. The CT metals included Tc, Re, Ru, Os, Rh, and Ir. On P–T and NT alloys, C, H, and CH preferred to bind to Pt_3 at 1/4 ML coverage and Pt_2M at 1/2 ML coverage. CH_3 preferred to bind to top sites of Pt at both coverages. On CT alloys, C, H, and CH preferred to bind to Pt_2M at 1/4 ML coverage and PtM_2 at 1/2 ML coverage. CH_3 preferred to bind to top sites of the M atom at both coverages. The scaling relationship was established between the desorption energy of ethylene and methyl binding energy (BE_{CH3}) (Fig. 22b and c) as well as the activation energy of ethylene dehydrogenation and the methylidyne dehydrogenation reaction energy (ΔE_{CH}) plus the methyl binding energy (BE_{CH3}) (Fig. 22d) on various Pt_3–M alloys. It indicated that alloying Pt with Pb, Bi, Tl, Sn, Sb, Hg, and In decreased the ethylene desorption energy and increased the activation energy of C–H activation of ethylene, thus resulting in higher ethylene selectivity.[283]

Cybulskis *et al.*[290] investigated Zn promotion of platinum for ethane dehydrogenation by combining DFT, kinetic, and *in situ* spectroscopies. DFT calculations could accurately predict the electronic structure of Pt 5d valence orbitals in Pt/SiO_2 and $PtZn/SiO_2$. Zn lowers the energy of filled states of the Pt surface and weakens the binding energy between adsorbates and the Pt surface as well as increases the turnover rate of the reaction. In addition, Zn has a geometric effect, leading to the formation of a Pt_1Zn_1 intermetallic alloy with uniformly isolated Pt surface sites, which effectively suppresses hydrogenolysis and cracking reactions.

Ko *et al.*[291] investigated the influence of P doping into Ni-based catalysts on ethane dehydrogenation by combined DFT and experimental study. DFT calculations revealed that a $Ni_2P(001)$ surface exhibited a similar CH_3CH_2–H activation barrier to, but a much greater CH_2CH–H activation barrier (an indicator of the coking tendency) than a Ni(111) surface. Meanwhile, the experimental study demonstrated a much higher ethylene selectivity (<80%) and less carbon deposition on the $Ni_2P(2)/SBA\text{-}15$ catalyst compared to Ni/SBA-15 (<1% ethylene selectivity). This highlights the potential of using metal phosphides as robust and selective catalysts for alkane dehydrogenation.

Ge is another promising promoter. It can enhance the catalyst selectivity without decreasing the catalytic activity. DFT calculations were performed on MgO-supported Pt_3 and Pt_7 with Pt_2Ge and Pt_7Ge clusters.[278] It was found the Pt_2Ge could elongate the C–H bond more than Pt and had a lower activation barrier of 0.05 eV compared to 0.17 eV for pure Pt. Therefore, the activity of ethane dehydrogenation was not negatively affected by Ge. On the other hand, Ge quenched the unpaired electrons in the metal clusters, which were needed to activate alkenes for dehydrogenation. Ge in alloys made Pt interact less strongly with ethylene and therefore increased ethylene selectivity. For the smallest cluster size, the C binding energy was significantly reduced and increased catalyst resistance to deactivation due to coking.

3.1.3 Effect of Pt and Pt alloy particle size. Pt and PtSn alloy particle size effects were studied experimentally on ethane dehydrogenation by Bell and co-workers.[292] It was found that the ethane TOF increased monotonically with increasing particle size in the range of 1.5–8.5 nm, whereas the ethylene selectivity remained constant across all particle sizes. Their result suggested that ethane dehydrogenation was favored over flatter surfaces on large particles. The authors attributed the high TOF on large particles to the favored desorption of ethylene due to the lower binding energy of ethylene on terrace sites. The dehydrogenation and hydrogenolysis reactions have been studied on Pt(111) and Pt(211) with DFT calculations.[279] On the Pt(211) surface, CH_2CH_2* and CH_3CH* can be generated very rapidly from ethane with low activation barriers (Table 1). However, the stronger CH_2CH_2* adsorption energy on Pt(211) makes the desorption of ethylene more difficult compared to Pt(111). On Pt(111), CH_3CH* can be dehydrogenated rapidly to form CH_3C*. The C–C bond cleavage takes place most possibly *via* CH_3CH_2, CH_3CH, and CHCH. More quantitative data on reaction pathways require detailed microkinetic modeling. More recent work showed that under-coordinated step edge sites bonded C_2H_x and CH_x species more strongly than terrace sites.[280] These under-coordinated step edge sites promote deep dehydrogenation, resulting in coke formation and catalyst deactivation. Atomic layer deposition (ALD) of alumina on Pt step edge sites significantly suppresses unselective deep dehydrogenation and coke formation (Table 1). The experiment of decorating Pt with ALD of alumina results in a 4-fold increase in the TOF of ethylene formation.

Carbon deposition is also dependent on the particle size of Pt and PtSn alloy, as well as the Sn content. In general, carbon deposition under reaction conditions increases with increasing particle size, but higher Sn content suppresses carbon formation.[292]

3.2 Oxidative dehydrogenation of ethane

Oxidative dehydrogenation, which couples the endothermic dehydration of ethane with the strongly exothermic oxidation of hydrogen, exhibits higher ethane conversion and lower operation temperature compared to steam cracking, which leads to growing interest in this process. However, major practical challenges with ODH reaction still occur, which are (1) additional safety measures associated with O_2 in the feed and (2) the development of highly active and selective catalysts due to the high reactivity of olefins compared with the corresponding paraffins.[265] The ODH of ethane has not been practiced on a large scale yet. The relatively higher reactivity of olefins is attributed to the direct interaction of the olefin with catalytic surfaces. Typical undesired side reaction involves total oxidation to form CO, CO_2, and water. The reaction occurs through oxygen insertion into the C–H bond or from the addition of oxygen to olefins.

The only feedstock that can achieve high selectivity to olefins is ethane because ethylene is sufficiently unreactive

towards oxygen compared to ethane. This is evidenced by the bonding strength difference in paraffins and olefins. The weakest C–H bond in ethane has a bond energy of 4.35 eV, whereas the weakest C–H bond in ethylene has an energy of 4.60 eV. For propane and propylene, the weakest C–H bond has a bond energy of 4.16 and 3.74 eV respectively. A more significant difference exists for C–C bond energy; the weakest C–C bond in ethylene is a double bond with a bond energy of 7.46 eV compared to 4.29 eV in propylene, in which the weakest C–C bond is a single bond. In general, to achieve high selectivity, the weakest C–H or C–C bond in the olefin has to be less than 0.31 eV weaker than the weakest C–H bond in the reacting paraffin.[293] This is true for ethane and ethylene, but not for propane and propylene.

3.2.1 Reaction mechanism with oxygen as an oxidant on metal oxides. According to the analysis at the molecular level, the ODH of ethane with O_2 as an oxidant takes place by the way that dissociated O species that originated from gas-phase O_2 reacts with H species dissociated from ethane on the surface to form H_2O and ethylene, as shown below.[294]

$$C_nH_{2n+2} + 1/2O_2 \rightarrow C_nH_{2n} + H_2O \quad (8)$$

ODH normally accompanies the combustion of hydrocarbons, producing CO and CO_2. To avoid over-oxidation of hydrocarbons, lattice oxygen in metal oxides can be used as the alternative oxygen supplier for the ODH process, which is often called a chemical looping ODH process. Most of the catalysts that are active for the ODH of ethane fall into redox-active metal oxides such as V_2O_5,[295] MoO_3,[294] MoVTeNb mixed metal oxides,[296] Co oxides,[297] Ni oxides,[298] and IrO_2.[299] There is a general consensus that ODH of ethane on such materials follows a MVK[221] mechanism and the reactivity of oxygen plays a vital role in the C–H activation of ethane. That is, the lattice oxygen of metal oxides interacts with hydrocarbons to form oxygen vacancies (eqn (9)), followed by the regeneration process (eqn (10)).

$$C_nH_{2n+2} + M_xO_y \rightarrow C_nH_{2n} + M_xO_{y-1} + H_2O \quad (9)$$

$$M_xP_{y-1} + 1/2O_2 \rightarrow M_xO_y \quad (10)$$

V_2O_5 catalysts. The most prominent redox metal oxides for ethane ODH are supported V_2O_5 catalysts. The oxide support does not participate in the reaction, but it does influence the reactivity and stability of the oxygen bonded to V.[300] Three types of metal–oxygen bond have been identified in the surface vanadium species as illustrated in Fig. 23, including terminal V=O bonds, bridging O atoms between V and the support (V–O–S), and bridging O atoms between two V cations (V–O–V).[301] The isolated VO_4 species on the support contains the first two types of V–O bonds, while the polymeric VO_4 species contains all three V–O bonds.

Ethane ODH pathways on vanadium oxide catalysts were elucidated by kinetic and isotopic tracer and exchange measurements.[302] The lack of exchange products ($C_2H_{6-x}D_x$ or $C_2H_{4-x}D_x$ isotopomers) revealed that the first C–H bond cleavage in ethane and ethylene was an irreversible and kinetically relevant step in ODH and combustion reactions. $^{16}O_2$–$^{18}O_2$–C_2H_6 reactions on supported $V^{16}O_x$ domains led to the initial appearance of ^{16}O from the lattice in the products H_2O, CO, and CO_2, evidencing the involvement of lattice oxygen in C–H bond activation steps. The emerging paradigm is that the development of suitable catalysts requires fundamental insight into the reaction mechanism on a molecular level, including the details of the interactions with the catalytic surfaces and the associated gas-phase reactions. The theoretical calculation has been used to provide a molecular understanding of active sites and reaction mechanisms on vanadium-based oxides. Similar activity of oxygen species and reaction mechanisms of C–H bond activation have been found on ethane ODH[295] as well as propane ODH[303] on the V_2O_5(001) surface. The most favorable pathway occurred on the O(1) (V=O) site through a radical mechanism with an activation energy of 1.52 eV;[295] V–O–V was less active toward C–H bond activation (1.63 eV) through an oxo-insertion mechanism but much more selective towards ethylene formation. However, the terminal O site exhibited a more favorable side reaction leading to acetaldehyde than to ethylene. The first C–H activation step was the RDS, in good agreement with the experimental observation.[302] Water and acetaldehyde would desorb from the surface to create vacant O(1) sites easily. The oxygen molecule can re-oxidize the reduced vanadium, which is exothermic by 3.77 eV, with a barrier of 1.52 eV. Obviously, the surface of the catalyst can be re-oxidized easily at high temperatures when it is exposed to O_2. A more detailed discussion on the active sites, the reactivity of surface oxygen species, and the reaction mechanism of C–H bond activation of light alkanes can be seen in Section 4.2.

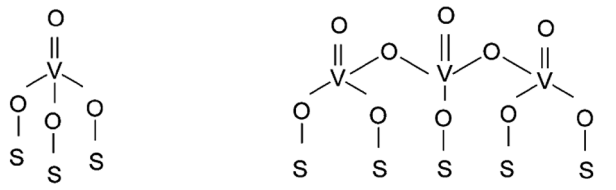

Fig. 23 Isolated and polymeric VO_4 species in supports.[301] Reproduced from ref. 301 with permission from the Royal Society of Chemistry, copyright 2011.

MoO_3 catalysts. The surface stability and equilibrium morphology of MoO_3 have been investigated by DFT calculations.[304] The (010) surface has the lowest surface energy among the surfaces exposed to the gas.[304] The ethane ODH mechanism on the MoO_3(010) surface was investigated by the first-principles study using the on-site Coulomb correction.[294] There are three types of surface oxygens, namely terminal O and symmetric and unsymmetric Mo–O–Mo, and the terminal O is the main active

site. Two stable configurations of ethylene adsorption on the $MoO_3(010)$ surface, namely horizontally and vertically adsorbed ethylenes, were identified. The horizontal adsorption favors ethylene formation with a barrier of 1.36 eV, which is lower than that of V_2O_5. The vertical adsorption of ethane favors acetaldehyde formation along the α-ODH pathway, and the ethylene oxide formation along the β-ODH pathway. The β-ODH pathway may also produce ethylene from the CH_2CH_2O intermediate, with the second C–H bond activation of ethane as the RDS. Towards horizontal C_2H_6 ODH reaction (the dominant ethylene formation pathway), the first C–H bond activation of ethane is the RDS. This is in agreement with the kinetic study that irrespective of the oxidant's chemical identity (O_2, CO_2 or H_2O), ethane activation occurs *via* the kinetically relevant C–H activation of C_2H_6 on the lattice O of MoO_x, forming ethylene.[305]

MoVTeNb mixed metal oxides. MoVTeNb mixed metal oxides have exhibited high selectivity and yields to C_2H_4. The catalyst is typically composed of two compounds $Mo_{7.8}V_{1.2}Te_{0.937}NbO_{28.9}$ and $Mo_{4.31}V_{1.36}Te_{1.81}Nb_{0.33}O_{19.81}$, which are referred to as M1 and M2 phases, respectively.[306] The structure of the M1 phase is illustrated in Fig. 24(a). It is generally accepted that the M1 crystalline phase is responsible for high activity and selectivity due to its ability to catalyze the initial homolytic H abstraction from alkanes.[307] Both the basal [001] plane[308] and lateral surface[309,310] have been reported to be responsible for the activation of alkanes. The S2–S4–S7 metal positions were proposed as the catalytic centers for alkane activation. The crystal termination of the M1 phase did have an impact on the intrinsic activity of ethane ODH.[296] A quantitative correlation was found between the sum of the surface areas of facets (001), (120), and (210) at the surfaces of the M1 crystals and the activity, demonstrating that multiple facets were involved in the reaction. Different facets would have different degrees of exposed active sites, and therefore different catalytic activities. The number of different facets can be tuned by changing the crystal morphology of the M1 phase of MoVTeNbO$_x$ catalysts.

In addition to the surface reaction, C_2H_6 ODH can also occur on M1 phase MoVTeNb mixed oxides' micropores, which was considered to be the reason for the high ethylene yields at moderate temperatures.[312,313] Deshlahra and co-workers[312] assessed the role of the M1 phase heptagonal channel micropores in regulating reactivity and selectivity using reactant size-dependent kinetic probes and DFT treatments for C_2H_6 and C_6H_{12} (cyclohexane) activations inside and outside the micropores and compared with nonmicroporous vanadium oxides (VO_x/SiO_2). As shown in Fig. 24(b), both C_2H_6 and C_6H_{12} activations can take place on the VO_x/SiO_2 surface and MoVTeNbO external surfaces. Inside the MoVTeNbO micropores, C_2H_6 activation is possible due to a tight guest–host fit, while C_6H_{12} cannot access intrapore sites because of the large kinetic diameter. The measured C_2H_6/C_6H_{12} activation rate ratios on MoVTeNbO were much higher than those measured on VO_x/SiO_2 and estimated by DFT calculations on the external surfaces, demonstrating that most C_2H_6 activations on MoVTeNbO occur inside the micropores under typical conditions.

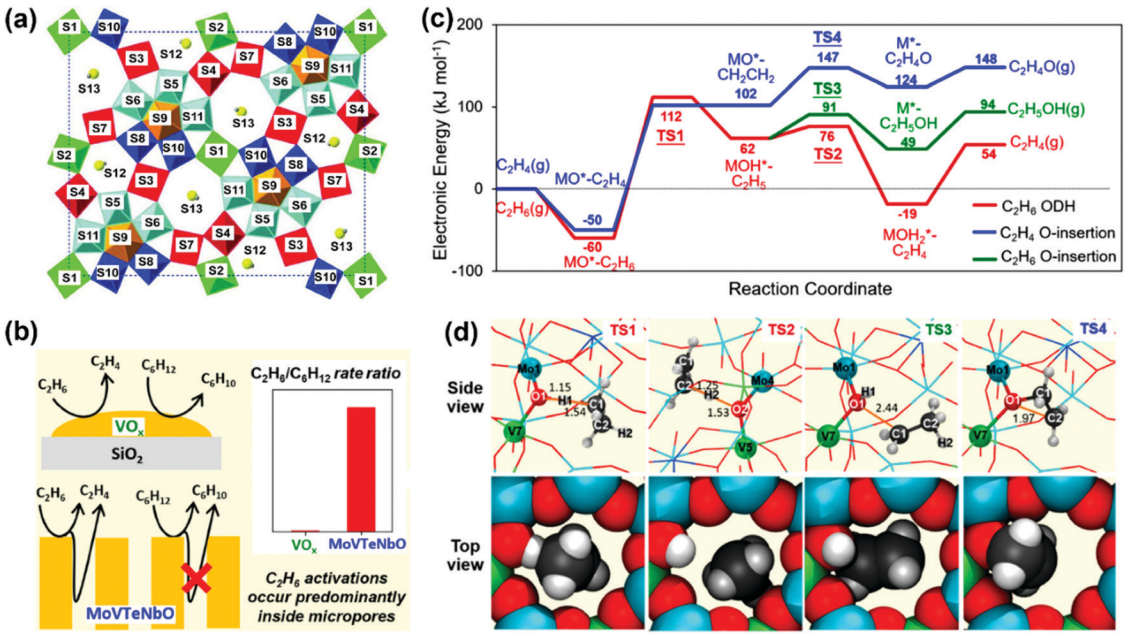

Fig. 24 (a) Two-dimensional diagram of the MoVTeNbO$_x$ M1 unit cell viewed in the [001] direction with 13 cation sites labelled as in the literature.[311] Active site centers are composed of metal positions S2–S4–S7 (red and green), located between unit cells.[296] Reproduced from ref. 296 with permission from Wiley-VCH, copyright 2016. (b) Accessibility of surface catalytic sites to reactants on VO_x/SiO_2 and MoVTeNbO as well as C_2H_6/C_6H_{12} rate ratios on MoVTeNbO relative to the corresponding values on VO_x/SiO_2. (c) vdW-DF2 derived electronic energies and (d) structures of transition states for C_2H_6 ODH (TS1, TS2), parallel O-insertion in $^{\bullet}C_2H_5$ (TS3) and sequential O-insertion in C_2H_4 (TS4) at O-atoms exposed in heptagonal pores of double-layer MoVTeNbO.[312] Reproduced from ref. 312 with permission from the American Chemical Society, copyright 2018.

MoVTeNbO and VO_x/SiO_2 exhibited similar product selectivities for C_6H_{12} oxidation, while for C_2H_6 oxidation, the ethylene selectivity was much higher on the former oxide. This suggested that the external surfaces of MoVTeNbO displayed a similar ability to activate C–H bonds and prevent O-insertion in products with VO_x/SiO_2, but the micropores in MoVTeNbO are more selective for C–H activation, which was confirmed by DFT calculations. The DFT calculated electronic energies and structures of transition states for C–H activation and O-insertion in C_2H_6 and C_2H_4 inside the heptagonal pores of MoVTeNbO are shown in Fig. 24(c) and (d), respectively. C_2H_6 ODH is the dominant reaction pathway, with the first C–H activation as the RDS and ethylene as the product. The C–O bond formation *via* two O-insertion pathways is hindered due to steric hindrances, which require much bulkier CH_2 groups in close contact with concave pore walls (top views of TS3 and TS4 in Fig. 24d). Therefore, the heptagonal pores of MoVTeNbO enhance ethylene selectivity by enhancing C–H activation and suppressing O-insertion reactions *via* a combination of van der Waals (vdW) and steric effects.

The same group investigated lattice O atom coordination effects and pore confinement on selectivity limitations for ethane ODH catalyzed by vanadium–oxo species.[313] DFT was used to calculate C–H activation and C–O formation in ethane ODH on (001) surfaces of V_2O_5 and MoVTeNb oxides and in pores of MoVTeNb oxides. High C_2H_4 selectivity depended strongly on the O atom coordination and H atom addition energies of the oxides. C–O formation preferably occurred at V═O terminal O atoms due to their significantly lower energy than V–O–V, V–O–Mo bridging or V_2–O–V tri-coordinated O atoms. In contrast, the C–H activations on MoVTeNbO(001) surfaces exhibited similar activation energies between bridging O atoms and terminal O atoms. Terminal O atoms are inaccessible in MoVTeNbO bulk oxide micropores, which leads to high ethane activation rates and ethylene selectivity.

Co oxides. Co_3O_4 is a good oxidation catalyst. Its high activity has been attributed to the weak metal–O bond among other transition metal oxides[314] and the easy formation of oxygen vacancies at the catalyst surfaces.[315] Co_3O_4 is also active for ODH. Surface termination can have an impact on the catalyst activity and selectivity of ODH. Experimental and theoretical calculations have identified several stable Co_3O_4 surfaces, such as (110), (111), and (100). Fung *et al.* developed a full catalytic cycle of ODH based on first-principles calculations on a thermodynamically stable Co_3O_4(111) surface.[297] The full catalytic cycle includes the first and second C–H bond activations, hydroxyl clustering, water formation, water desorption, and lattice oxygen-site regeneration. On the most stable terminal surface, there are two types of lattice oxygen: O^A, which is triply coordinated to the subsurface cobalt (Co^{3+}); and O^B, which is not only doubly coordinated to the subsurface Co but also singly coordinated to the surface Co. There are also two types of C–H activation of ethane, namely the homolytic pathway where the lattice O is the active site, and the heterolytic pathway where the O and Co pair is the active site. The C–H activity depends on the lattice oxygen reactivity. The formation energy of oxygen vacancy and Bader charges are good descriptors to predict well the higher reactivity of O^A. The first C–H activation was more favorable on more reactive lattice oxygen and had a lower barrier for the homolytic pathway ($\sim$0.62 eV), but the barrier for the second C–H activation was lower for the heterolytic pathway. The water formation step of the catalytic cycle on the pure (111) surface was found to be the RDS, possibly due to the highly oxyphilic nature of the Co surface.

The same group investigated the effects of Co_3O_4 doping on oxygen reactivity and ethane C–H activation energies over Co_3O_4(111) and (311) surfaces for a series of dopants.[316] The DFT calculations illustrated that the O vacancy formation energy and H adsorption energy were descriptors for oxygen reactivity, which were directly correlated with the ethane C–H activation energy and the TS geometry. The group also discovered that the surface orientation had a significant influence on dopant efficacy.

Ni oxides. The reaction mechanism of ODH of ethane has also been studied on nickel-based oxides, namely Ni_3O_x (x = 1, 2, 3) by DFT calculations using the cluster model.[298] Ethylnickel species have been identified as main reaction intermediates through a concerted mechanism involving two sites for the C–H bond activation step. Subsequent pathways include beta-H elimination, alpha-H abstraction, C–C bond cleavage, and isomerization to ethoxide species. The selectivity of ethylene depends on the relative rates of the four pathways. According to the calculation, the $S_{C_2H_4}$ selectivity increases from 37% to over 99% with decreasing x value. The oxygen vacancy has a significant influence on the selectivity and more oxygen vacancies in Ni oxides enhance remarkably the ethylene selectivity. An important issue for transition-metal catalyzed oxidation of hydrocarbons is the type of primary species generated from the C–H bond activation step and the types of species directly responsible for the initial product selectivity observed in the experiment.[14] The adsorbed ethane on oxygen sites forms ethoxide, which leads to ethylene formation. The high selectivity in the Ni_3O_1 case is due to the absence of a bare O atom nearby the α-Ni site and block isomerization from ethyl-nickel to ethoxide, which is more likely to undergo C–C bond cleavage.

Doping of NiO with Sn, Ti, and W has been shown to increase the catalytic activity and selectivity.[317] DFT calculations show that doping these metals into the NiO structure are thermodynamically feasible. The dopant, on the one hand, can decrease the particle size of NiO and open up more active sites. The incorporation of these metals into the NiO lattice, on the other hand, reduces the number of holes (h^+), resulting in a significant decrease of nonstoichiometric oxygen ($O^{\bullet-}$) in the NiO structure. The low concentration of nonstoichiometric oxygen contributes to the improved catalytic selectivity ($O^{\bullet-}$ is known to favor complete ethane oxidation to CO_2). Based on this study, a design criterion has been proposed; an optimum concentration of nonstoichiometric oxygen at the NiO surface exists. A too high oxygen concentration leads to total oxidation

of ethylene to CO_2, while a too low oxygen concentration leads to difficulty in activating ethylene at a lower temperature.

Doping of NiO with Nb in ethane ODH was found to form NbO_2 groups, considered to be the dopant, predicted by DFT calculations.[318] The NbO_2 groups were created because the Nb-doped NiO adsorbed oxygen very strongly from the gas phase and dissociated it to generate two chemisorbed O atoms, with each making an Nb–O–Ni bond. The calculated activation energies of dissociative adsorption of ethane on the NbO_2-doped oxide were substantially lower than that on undoped NiO. This is because the NbO_2-doped oxide was more reactive in breaking the C–H bond of ethane than undoped NiO. However, this is different from the experimental results[319,320] in that even adding a small amount of Nb decreased the ethane conversion per unit area and per unit time for NiO catalysts. The difference between the experimental observation and the DFT prediction might be due to the formation of NbO_x clusters on the surface or $NiNb_2O_6$ (instead of NbO_2 groups used in the model) during the calcination in oxygen for catalyst preparation. Experiments found that the slow deactivation of the catalyst was attributed to the formation of $NiNb_2O_6$.

IrO_2 catalysts. In contrast to most metal oxides, where initial C–H bond activation is the RDS of ethane ODH, the first C–H bond activation of ethane is a fast reaction over IrO_2 catalysts. A DFT study of ethane activation over an $IrO_2(110)$ surface reported by Pham *et al.*[321] indicated that ethane was most stably adsorbed on $IrO_2(110)$ by interacting with two adjacent Ir_{cus} (five-fold coordinated Ir) atoms, and ethane activation on $IrO_2(110)$ was both thermodynamically (ΔE, PBE: −1.12 eV; optB88-vdW: −1.13 eV) and kinetically (E_a, PBE: 0.50 eV; optB88-vdW: 0.57 eV) favorable, which was expected to occur at low temperature. Similarly, the temperature-programmed reaction spectroscopy (TPRS) and DFT results reported by Bian *et al.*[299] showed that ethylene desorption was the RDS in the conversion of ethane to ethylene over $IrO_2(110)$ during the TPRS. The DFT calculated barrier of ethane C–H bond cleavage over clean $IrO_2(110)$ (0.39 eV) was much lower than that of ethylene desorption (1.96 eV). However, the DFT calculation predicted that the oxygen vacancy plays a significant role in ethane conversion. Partial hydrogenation of $IrO_2(110)$ was found to enhance ethane conversion to ethylene while suppressing ethane oxidation to CO_x species. According to DFT, hydrogenation of reactive O atoms of $IrO_2(110)$ to OH groups effectively inhibited these sites as H atom acceptors, resulting in ethylene desorption being favored over further dehydrogenation. The study revealed that $IrO_2(110)$ displayed an exceptional ability to promote C_2H_6 dehydrogenation to C_2H_4 near room temperature, and controlled deactivation of reactive O atoms was an effective way to facilitate ethylene production from ethane on $IrO_2(110)$.

3.2.2 Reaction mechanism with CO_2 as an oxidant. CO_2 can also be used in ODH of ethane as a soft oxygenate.

$$C_2H_6(g) + CO_2(g) \rightarrow C_2H_4(g) + CO(g) + H_2O(l) \quad \Delta H_{25}^{\circ} = 1.39\ \text{eV} \tag{11}$$

The advantage of this approach is that overoxidation of the reactants and products can be reduced and therefore the olefin selectivity can be enhanced.[268] The effect of the support nature on the catalytic activity and stability has been investigated on CrO_x catalysts supported on γ-Al_2O_3, ZrO_2, CeO_2, and $Ce_xZr_{(1-x)}O_2$.[322] The nature of the support influences the oxidation state of chromium species. The reaction pathway, catalytic activity, and stability of the catalyst depend on both the chromium state and support properties, in particular, on its acid–base and redox properties. On CrO_x/γ-Al_2O_3 catalysts, ethylene is formed by a direct dehydrogenation (DDH) of ethane accompanied by RWGS, while on CrO_x/ZrO_2, ethylene is formed by selective ODH. Besides the oxide surface, bimetallic catalysts also appear to be active for this reaction.

In addition to producing ethylene *via* an ODH pathway through C–H bond scission, the interaction of ethane with CO_2 can also produce synthesis gas *via* a dry reforming pathway through C–C bond scission. High ethylene selectivity can be achieved by using different catalysts to selectively promote the C–H bond scission and preserve the C–C bond scission. Chen and co-workers have done a lot of work on it.[323–326] They studied the dry reforming and ODH of ethane with CO_2 as a soft oxidant on CeO_2 supported bimetallic catalysts.[323] It was found that $CoPt/CeO_2$, $CoMo/CeO_2$, and $NiMo/CeO_2$ bimetallic catalysts favored the reforming pathway to produce synthesis gas *via* the C–C bond cleavage, while $FeNi/CeO_2$ favored the ODH pathway to produce ethylene *via* the C–H bond cleavage. The DFT calculated energy profiles shown in Fig. 25 clearly

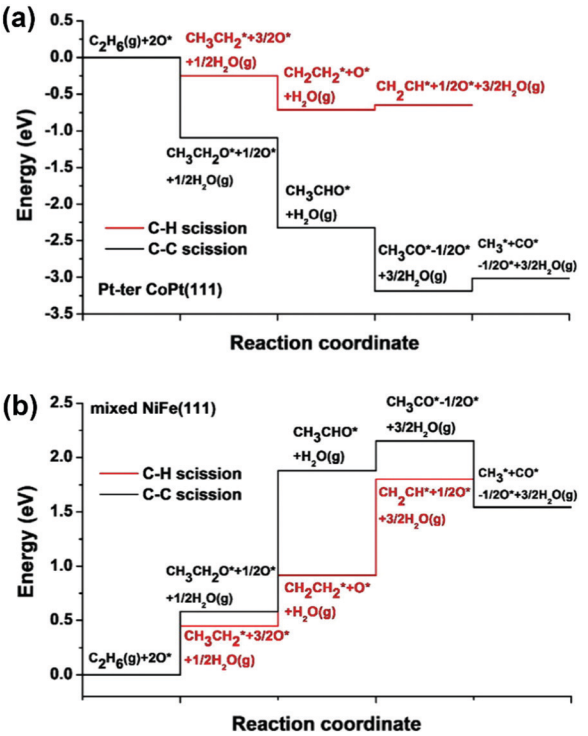

Fig. 25 DFT calculated energy profiles of reforming and ODH of ethane on (a) Pt-terminated CoPt(111) and (b) mixed FeNi(111).[323] Reproduced from ref. 323 with permission from Elsevier, copyright 2016.

demonstrate different pathways on the $CoPt/CeO_2$ catalyst compared to the $FeNi/CeO_2$ catalyst.

The most likely active sites over CeO_2-supported NiFe catalysts were further elucidated by the same group by combining *in situ* characterization with DFT calculations.[324] Both the experimental and theoretical results revealed that the Ni–FeO_x interfacial sites could selectively break the C–H bonds and preserve the C–C bond of C_2H_6 to produce ethylene, while the Ni–CeO_x interfacial sites efficiently cleaved all of the C–H and C–C bonds to produce synthesis gas. Similar work has been done on non-precious FeNi and precious NiPt catalysts supported on CeO_2 for ODH of propane by CO_2 of propane and dry reforming.[327] DFT was performed on three representative surfaces: Fe_3Ni, FeO/Ni(111), and Ni_3Pt. The FeO/Ni(111) surface was used to represent potential FeO–Ni interfacial active sites due to the observation of the FeO layer on the Ni surface during the reaction conditions. DFT results revealed that on bulk-terminated-Fe_3Ni(111) the ODH reaction (ΔE = 0.29 eV and E_a = 1.02 eV) had lower reaction energy and activation energy than *O insertion reaction (ΔE = 0.43 eV and E_a = 3.30 eV). Therefore, the ODH reaction is more favorable along the C–H bond cleavage pathway than the *O insertion reaction along the C–C bond cleavage pathway. Similarly, on the FeO/Ni(111) surface, ODH reaction is favored over the C–C bond cleavage dry reforming reaction. However, on the Ni_3Pt catalyst, the C–C bond cleavage is favored over C–H bond cleavage dehydrogenation reaction.

Chen and co-workers also found that the Mo_2C/γ-Al_2O_3 catalyst preserved the C–C bond cleavage of ethane to produce ethylene, while Pt/CeO_2 preferably produced synthesis gas.[325] These findings agreed with DFT results that the Mo_2C(001) surface led to ethylene formation, and the CeO_2/Pt(111) surface preferentially generated synthesis gas. Besides, the authors demonstrated that a MoO_x modified Mo_2C surface was related to ethylene formation in ethane ODH with CO_2.[326] Oxygen modification was able to inhibit the C–C bond cleavage and reduce coke formation. The Fe promoter could accelerate the formation of the surface MoO_x layer and stabilize it, leading to a higher ethylene yield and improved stability.

An *ab initio* microkinetic model (MKM) was constructed to investigate the reactivity trends of transition metal catalysts for ethane dehydrogenation with CO_2 as a mild oxidant.[328] Both direct ethane dehydrogenation and O-assisted ethane dehydrogenation on terrace (111) and step (211) surfaces were studied. Ethane was predominantly converted to ethylene *via* direct dehydrogenation on both surfaces. Towards O-assisted ethane dehydrogenation (CO_2 consumption), Co, Ru, Ni, and Rh were more active than other transition metals on both surfaces (Fig. 26a and b). In an attempt to screen bimetallic alloys to achieve greater CO_2 consumption activity with reduced coke formation, three potential bimetallic alloys (Ni_3Fe, Ni_3Co and Pt_3Co) were selected (Fig. 26c). Out of them, two were tested experimentally, and $FeNi/CeO_2$ has shown some promise for ethane dehydrogenation along with CO_2 reduction.

4. Activation of C–H bonds of propane and propylene

Propylene is one of the vital petrochemical building blocks for producing various chemical products, such as propylene oxide, polypropylene, and acrylonitrile. The conventional production processes of propylene are mainly steam cracking and fluidized catalytic cracking of light diesel, naphtha, and other oil byproducts.[329,330] Along with the large-scale revolution of shale gas and the growth of the global propylene demand (which is expected to increase to 130 million metric tons by 2023), on-purpose propylene production, specifically propane dehydrogenation (PDH), seems to be a promising alternative.[331] The PDH process is an endothermic reaction, and successfully commercialized PDH catalysts can be categorized into two groups: Pt- and Cr-based catalysts. The reaction is normally performed at around 600 °C on Al_2O_3 supported Pt–Sn or CrO_x catalysts. Pt-Based catalysts are commonly used commercial catalysts for PDH because of their high catalytic activity. Still, they suffer from unsatisfactory propylene selectivity, fast deactivation, and poor catalyst stability caused by coke formation and catalyst sintering at high reaction temperatures.[277,289,292,332] Thus,

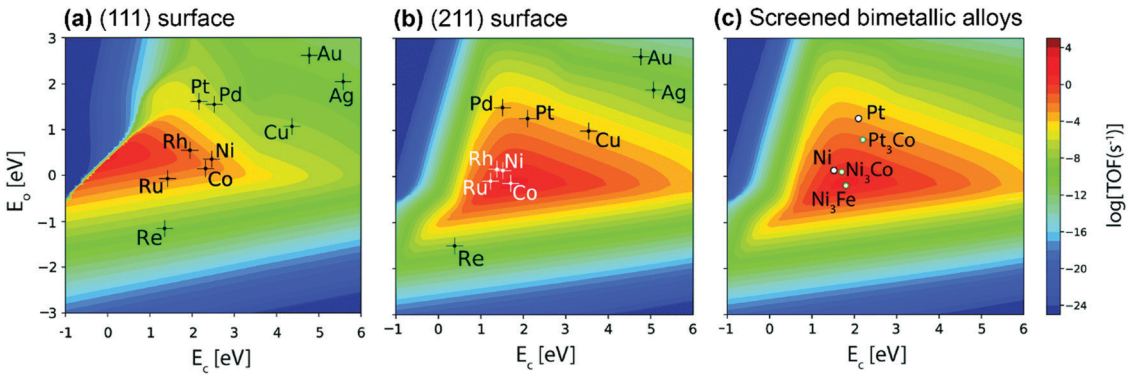

Fig. 26 Elementary reaction rate for oxygen assisted ethane dehydrogenation ($C_2H_6 + O \rightarrow C_2H_5 + OH$) over the (a) (111) surface and (b) (211) surface of transition metal catalysts; and (c) screened alloy candidates.[328] Reproduced from ref. 328 with permission from the Royal Society of Chemistry, copyright 2020.

significant efforts have been devoted to improving the performance of Pt-based catalysts, generally by doping with additional promoters, such as late TMs and main-group metals (including Ga and Sn) and by modifying carriers.[333,334]

The oxidative dehydrogenation of propane generally follows the MVK mechanism,[221,335,336] also known as the lattice oxygen mechanism. This mechanism holds that reactants with reducing properties react with highly reactive oxygen atoms in the catalyst surface to generate oxidation products and thus form oxygen vacancies on the surface. Then, followed by O_2 or CO_2 adsorption at the oxygen vacancy sites, the sites can be oxidized or filled with oxygen, forming a catalytic cycle. Besides, in order to break the thermodynamic limitations of the propane dehydrogenation reaction, an oxidant that is added to the reaction feed or system will react with the intermediate species hydrogen or the product H_2 to produce water, releasing a large amount of heat.[337,338] However, for the ODH of propane, the reaction products are easily oxidized to produce CO and CO_2, so the reaction has to be carried out at a lower temperature in order to obtain a higher selectivity.[339] Also, propane dehydrogenation is a kinetically controlled reaction, and the activation of the C–H bond in propane is usually a rate-determining step, which requires the reaction at a higher temperature.[340]

Currently, in the PDH and ODH systems, the nature of the reaction mechanisms and reaction pathways on the catalysts remains elusive, and many side reactions such as deep dehydrogenation, C–C bond cleavage, H migration, and H_2O formation also need to be taken into consideration. By DFT calculations, the surface electronic structures of catalysts can be studied, mainly for exploring the active sites, stability, and modulation mechanism on the surface. Then, the elementary steps of dehydrogenation reaction involved in the network of the main and side reactions, together with the migration of H on the catalyst surface, are investigated to identify a favorable reaction pathway. Besides, the kinetic analysis can further convert the rate constants of the elementary steps calculated with DFT to the corresponding turnover rates under the reaction conditions, and consequently, it can determine the activity trend and rate-determining steps. It is therefore of great interest to employ theoretical calculations as a tool for investigating how the PDH and ODH catalysts function on an atomic scale. We will see that, by using microkinetic analysis combined with results from DFT calculations, the crucial roles of different active sites, promoters, and supports, and reaction pathways and RDSs[29] can be explained, which guides the investigation toward a more effective catalyst for PDH and ODH. The progress in computational catalysis of PDH and ODH is reviewed in Sections 4.1 and 4.2, respectively.

4.1 C–H bond activation in propane on metals

4.1.1 Adsorption of propane and propylene on metal surfaces. In the last few decades, the activation of C–H bonds of propane over transition-metal and alloy surfaces has been extensively studied both theoretically and experimentally.[341–346] The surface reaction of PDH can lead to numerous fragments ranging from C1 to C3 species adsorbed on these surfaces. As for the C3 species, propane and propylene are the reactant and the desired main product, respectively,[347,348] and their adsorption on metal surfaces has been the subject of extensive research.[349–351] Generally, because the propane molecule is a saturated compound and has no unpaired electron, there is no hybridization between propane and metal d states, and therefore propane is physisorbed on the metal surfaces.[347,349,352] The lengths of the C–H and C–C bonds of adsorbed propane are found to be almost the same as those of the isolated propane (C–H: 1.10–1.11 Å, C–C: 1.53 Å).[349,351] The equilibrium adsorption distances between propane and metal surfaces are in the range from 2.5 to 4.5 Å, suggesting that this is mainly an intermolecular interaction.[348,350,352,353] On flat surfaces such as Pt(111), the GGA-PBE adsorption energies of propane at different adsorption sites fall within the range of −0.02 to −0.06 eV, as presented in Table 2.[349,354] The small variation in adsorption energy from site to site indicates that propane does not favor any particular site on the flat metal surfaces. The adsorption energies of propane are generally underestimated by the PBE functional because the standard GGA fails to account for long-range vdW interactions between propane and metal surfaces. With the vdW correction considered, the adsorption energy of propane becomes much more negative.[353] For the stepped metal surface, propane preferably adsorbs at the hollow site below the step edge, and the adsorption energies are in the range from −0.39 to −0.46 eV.[331,355] Clearly, the propane molecule experiences more attractive interactions from the stepped surface than those from the flat surface because there exists a larger contact area between them, and the strength of dispersion forces tends to increase with increasing molecular size. Moreover, alloying of Pt with metals such as Sn did not alter the adsorption energy (Table 2).[350]

A crucial point in the dehydrogenation reaction is the examination of the competition between propylene dehydrogenation and desorption, which provides the key to understanding how the selectivity of catalyst surfaces can be tuned.[358] Compared to propane, propylene has a half-saturated double bond (C═C), which could be readily decomposed on metal surfaces. Valcárcel *et al.* proposed a schematic representation of adsorbed propylene on Pt(111), where these surface structures mainly depend on coverage and temperature.[359] At temperatures below 230 K, propylene is undissociated to adsorb on the metal surface, as is the case for ethylene. The di–σ and π models are the most common propylene chemisorption configurations on metal surfaces, as shown in Fig. 27(a). The adsorption configuration depends on the site coverage of propylene, and the di–σ mode through its unsaturated C═C bond at a short bridge site is predominant below half-saturation coverage, with the C═C bond being nearly parallel to the surface, and the methyl group would tilt away from the surface as the site coverage is close to saturation. The adsorption energy of the di–σ adsorption is generally more negative than that of the π adsorption.[349,350,353,357,359] This can be explained by the larger valence charge density between the C and metal surface in the di–σ bond than in the π adsorption, indicating a stronger C–metal bond, as shown in Fig. 27(b). The strong adsorption weakens the C═C bond.[360] Upon the di–σ

Table 2 Adsorption energies and geometries of propane and propylene on different Pt surfaces

Surface	Propane	Propylene						
		di-σ				π		
	E_{ads} (eV)	E_{ads} (eV)	$d_{C1=C2}$ (Å)	d_{Pt-C1} (Å)	d_{Pt-C2} (Å)	E_{ads} (eV)	XC functional	Ref.
Pt(111)	−0.34	−0.83	1.501	2.145	2.178	—	vdW_DF	350
Pt_3Sn/Pt(111)	−0.39	−0.48	1.504	2.159	2.174	—		
Pt_3Sn(111)	−0.28	−0.54	1.497	2.159	2.193	—		
$PtSn_2$(111)	−0.24	−0.23	—	—	—	—		
Pt(111)	—	−0.64	1.48	2.12	2.14	0.06	B3LYP	356
Pt(111)	−0.06	−0.93	1.50	2.11	—	−0.66	PBE	349
Pt(100)	−0.04	−1.22	—	—	—	−1.07	PBE	357
Pt(111)	−0.04	−0.97	—	—	—	−0.67		
Pt(211)	−0.04	−1.43	—	—	—	—	PBE	347

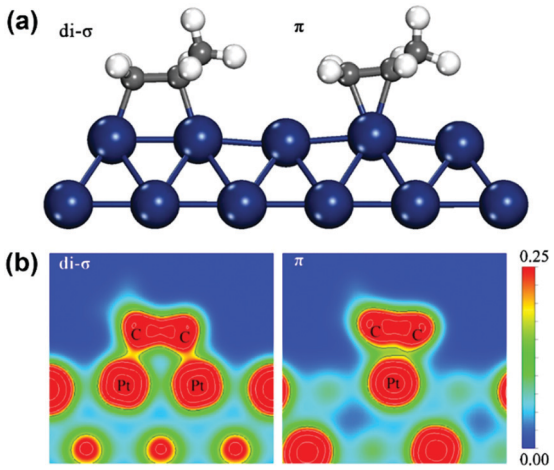

Fig. 27 (a) Adsorption modes of propylene on Pt surfaces.[357] Reproduced from ref. 357 with permission from Elsevier, copyright 2014. (b) The valence charge densities calculated for different propylene adsorption modes.[349] Reproduced from ref. 349 with permission from Elsevier, copyright 2010.

adsorption over metal surfaces, the length of the double C=C bond in propylene increases from 1.36 (in gas-phase propylene) to about 1.50 Å,[349,351,353] which is close to the single C–C bond length of propane. This change, together with the fact that propylene loses its "planarity" as the C–H bonds bend away from the surface plane, indicates the rehybridization of the C atom from sp^2 to sp^3, and the C=C bond is therefore weakened by forming covalent bonds with Pt atoms. On Pt(100)[357] and Pt(211) surfaces,[347] propylene adsorption also prefers the di–σ mode to the π mode. The adsorption energy of propylene follows the order of Pt(211) > Pt(100) > Pt(111), as can be seen in Table 2. Although the estimated adsorption energy depends on the functionals used, it does not change the trend on the different surfaces. The adsorption energy on Pt(111) obtained with the vdW–DF functional agrees well with the experimental desorption energy determined using temperature-programmed desorption (TPD) measurements.[350]

Alloying Pt(111) with less reactive metal Sn leads to weaker propylene adsorption, as can be seen in Table 2.[350] Propylene binds preferentially to the Pt_3Sn(111) surface in the di–σ mode, similar to that on Pt(111), but the adsorption is weak on the $PtSn_2$(111) surface and dominated by vdW interactions. This result is mainly attributed to the geometric effect of introduced Sn, which reduces the number of Pt–Pt di–σ sites accessible by propylene, whereas the electronic effect that originated from the interaction energy of the Pt–Pt di–σ sites was found to be small.

4.1.2 Activation of the first C–H bond of propane. The propane dehydrogenation process involves a relatively complex reaction network and a large number of reaction intermediates and the elementary steps involved are mainly the C–H and C–C bond-breaking reactions. These elementary steps can be divided into three categories, as shown in Fig. 28(a): (1) the dehydrogenation steps from propane to propylene (steps 1–4), (2) the deep dehydrogenation steps from propylene to 1-propenyl and 2-propenyl (steps 5 and 6), and (3) the C–C bond cleavage reactions of propane, 1-propyl, 2-propyl, and propylene (steps 7–10).[357] The initial C–H bond cleavage at the methyl (step 1) or methylene (step 2) groups of physisorbed propane is often the RDS that governs the rate law of the overall dehydrogenation reaction, leading to the 1-propyl or 2-propyl species.[358]

The C–H bond dissociation energy of propane is 4.35 and 4.17 eV for the primary and secondary C–H bond scission, respectively. In the catalytic system, the energy barriers for the initial activation of the propane C–H bonds at the methyl and methylene groups are 0.69 and 0.70 eV on Pt(111), respectively, which indicates that there is no particular preference for the activation of C–H bonds on the surface.[347] For the transition states of propane activation on Pt surfaces, propane is bonded to Pt surfaces *via* the C atom, where the H in C–H is bonded to adjunct Pt. The C–H bonds at the methyl group are stretched by 1.50 Å (see Fig. 28b), as compared to the C–H bond length in gas-phase propane (1.10 Å). The geometries of the transition states on Pt(111), Pt(100), and Pt(211) are almost identical, as shown in Fig. 28(b). The C–H bond activation follows the universal scaling relationship, as shown in eqn (4). The lower C–H bond energy leads to a lower activation energy of propane activation than ethane and methane activation. The activation energies of the first dehydrogenation steps on Pt(211) are lower than those on Pt(100) and Pt(111) due to the higher hydrogen affinity on the unsaturated surfaces, where the lower activation energies for propane give higher dehydrogenation activity on

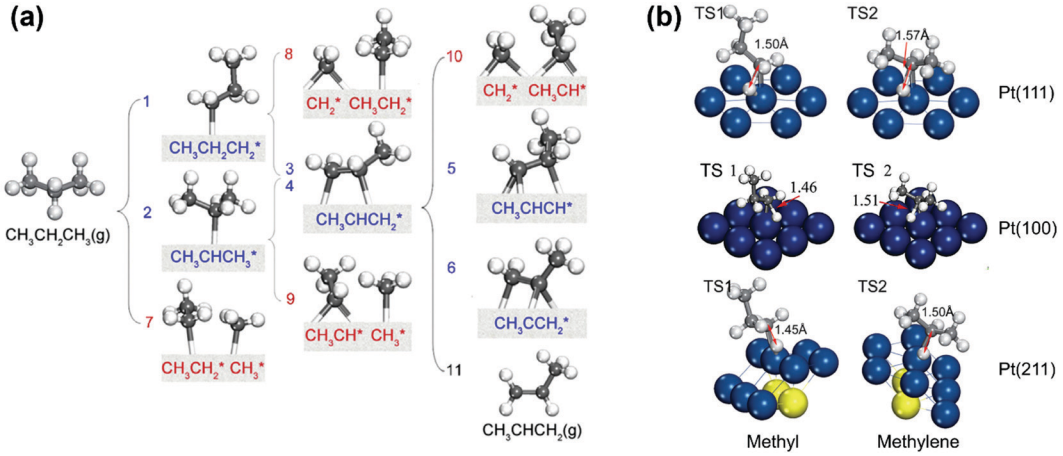

Fig. 28 (a) Reaction network for propane dehydrogenation to propenyl and (b) geometries of the transition states for the initial activation of the propane C–H bonds at the methyl and methylene groups on Pt(111), Pt(100), and Pt(211). The detached H atoms are not included for clarity. The numbers signify the sequence numbers of the elementary steps.[347,357] Reproduced from ref. 347 with permission from the PCCP Owner Societies, copyright 2011. Adapted from ref. 357 with permission from Elsevier, copyright 2014.

these three surfaces. The activated C–H bonds are stretched by 0.36–0.41 Å. The energy barriers for the activation of C–H bonds occurring at the two groups are calculated to be 0.32 and 0.28 eV on stepped Pt(211), and 0.43 and 0.42 eV on Pt(100), respectively.[357]

The addition of one or more main-group metals or TMs is an effective way to modify Pt-based catalysts.[350,361,362] DFT calculations revealed that the Sn component could broaden the d-band of Pt, giving rise to a downshift of the d-band center, and the dehydrogenation activity ranked in the descending order is: Pt(111) > Pt_3Sn(111) (bulk alloy) > Pt_3Sn/Pt(111) (surface alloy) > $PtSn_2$(111) (bulk alloy) > Pt_2Sn/Pt(111) (surface alloy).[348] In addition to Pt-based catalysts, other metal catalysts, such as metal Ni, intermetallic Pd–Zn, and Pd–Cu, have also been studied for the activation of C–H bonds.[351,363,364] Saelee *et al.* reported that the activation energy for the first dehydrogenation of propane on Ni(111) (0.69 eV) is close to that on Pt(111) (0.70 eV). Single Pd atoms at the edge site of Cu_{55} clusters can facilitate the first C–H bond cleavage, and the energy barrier predicted using the PBE functional is 1.06 eV, approximately 0.25 eV lower than the corresponding barrier on pure Cu_{55} clusters. With the correction of the vdW–DF functional, this energy barrier is increased to 1.17 eV.[364]

4.1.3 Mechanism of propane dehydrogenation to propylene on metal surfaces. Pt is one of the most commonly used commercial catalysts for PDH.[2] It is generally accepted that the dehydrogenation of propane over Pt catalyst follows the reverse Horiuti–Polanyi mechanism.[274] The dehydrogenation steps from propane to propylene is shown in Fig. 28(a) (steps 1–4), and the energy barriers for these four steps can describe the catalytic activity of metal surfaces for propylene production.[357] Table 3 summarizes some of the calculated energy barriers of PDH over Pt(111), Pt(100), and Pt(211) surfaces.[340,347,353,357] From the table, one can see that the energy barriers for both the first and second C–H bond activations of propane follow the order Pt(211) < Pt(100) < Pt(111). The stepped Pt surfaces having coordinatively unsaturated Pt atoms are kinetically more favorable for the dehydrogenation of propane to form propylene than the flat surfaces. Recently, however, Xiao *et al.*[365] suggested that although PDH over Pt(111) follows the generally accepted reverse Horiuti–Polanyi mechanism, as shown in Fig. 29, an unexpected non-reverse Horiuti–Polanyi mechanism over Pt(211) is proposed to dominate the kinetics.

In addition, the strongly endothermic nature of PDH ($\Delta_r H^\circ$ = 1.28 eV, under standard conditions at 298 K) requires high reaction temperature (800–980 K) to achieve a reasonable propane conversion.[366] However, side reactions, such as cracking, hydrogenolysis, deep dehydrogenation, oligomerization, cyclization, and coke formation, can be promoted even more dramatically by the increase in temperature.[332,367] As a result, ethylene (or ethane), methane, and coke are often produced in the PDH reaction as byproducts. The critical challenge for the catalysis of PDH is to reduce the selectivity to byproducts and to maintain the catalytic stability of the catalyst. It is thus essential to include not only the C–H bond activation but also the C–C bond cleavage in the whole catalytic cycle of PDH for the kinetic analysis. Yang *et al.* systematically investigated the PDH process on flat and stepped Pt surfaces, including Pt(111), Pt(100), and Pt(211).[347,349,357] They focused on the kinetics of the C–H bond activation of all the C3 intermediates in PDH, containing 17 dehydrogenation elementary reactions (see Fig. 30) and 12 C–C bond-breaking steps. As an example, the energy profile for PDH on Pt(111) is shown in Fig. 30(b). The insights provided by these studies are summarized as follows:

(1) A good scaling relation was found between the transition-state energy and the final-state energy for C_3H_x (x = 3–9) dehydrogenation. C–C bond cleavage steps have higher transition state energy and hence higher activation energy than C–H activation.[347] The adsorption strength of the intermediates is the key parameter in tuning the activity and selectivity. The stepped Pt surfaces are kinetically more favorable than the flat surfaces for the dehydrogenation of propane because of the stronger adsorption of intermediates on Pt(211).[347,368]

Table 3 Calculated energy barriers (E_{act}) for propane and propyl dehydrogenation on different Pt surfaces

Surface	E_{act} (eV)				XC functional	k points	Unit cell	Ref.
	$C_3H_8 \rightarrow 1\text{-}C_3H_7$	$C_3H_8 \rightarrow 2\text{-}C_3H_7$	$1\text{-}C_3H_7 \rightarrow C_3H_6$	$2\text{-}C_3H_7 \rightarrow C_3H_6$				
Pt(111)	0.69	0.70	0.70	0.68	PBE	$7 \times 7 \times 1$	3×3	347
Pt(211)	0.32	0.28	0.34	0.33	PBE	$4 \times 2 \times 1$	1×3	347
Pt(100)	0.43	0.42	0.39	0.39	PBE	$7 \times 7 \times 1$	3×3	357
Pt(111)	0.59	—	0.66	—	PBE	$5 \times 5 \times 1$	3×3	331
Pt(111)	0.92	0.92	0.90	0.94	BEEF-vdW	$3 \times 3 \times 1$	3×3	353
Pt(111)	0.75	0.60	0.74	0.78	opt-PBE vdW–DF	$3 \times 5 \times 1$	4×2	340

(2) The activation energy difference between propylene dehydrogenation and desorption was identified as the selectivity descriptor. Lowering the desorption energy and increasing the C–H bond activation barrier of propylene are crucial for increasing the propylene selectivity. Both quantities are closely related to the adsorption strength of propylene. The selectivity towards propylene is substantially lowered in the presence of the coordinatively unsaturated surface Pt atoms due to the strong adsorption of propylene, which has recently been widely used to screen promising candidates as the catalysts for PDH.[331,345,354,369]

(3) The deeply dehydrogenated intermediate of propyne (CH_3CCH^*) was identified as an important surface species for the C–C bond breaking because it is the sole C3 species that energetically prefers the cleavage of the C–C bond to the C–H bond breaking, which has also been determined by the microkinetic analysis on Pt(111).[340,353]

(4) PDH to propylene follows the generally accepted reverse Horiuti–Polanyi mechanism over Pt(111), while over Pt(211), a non-reverse Horiuti–Polanyi mechanism dominates.[365] The experimental[354] and theoretical analyses of Gibbs energy profiles of the PDH reaction[340,353] suggest that the first C–H bond activation is the RDS on Pt(211) and Pt(100) for smaller Pt cluster sizes, while the second C–H bond activation is the RDS on Pt(111). The first C–H activation of propane was identified as the RDS on the Pt(111) by a microkinetic analysis.[340] It should be noted that the energy barriers for the first and second C–H bond activations are quite close on Pt(111). The RDS could change with the reaction conditions.

So far, there have been only three microkinetic studies of PDH based on a relatively full description of the reaction pathway of dehydrogenation to propylene, deep dehydrogenation, and C–C bond cracking over Pt(111) surfaces, which were carried out by Saerens *et al.*,[340] Lian *et al.*,[353] and Xiao *et al.*,[365] respectively. The DFT-based kMC simulations by Lian *et al.* reveal that there are quick deactivation and steady states during the PDH process.[353] The precursor of coke is mainly formed during the rapid deactivation, which originates from the coverage of cracking products at the active sites. Then, the surface species and active sites covered by the hardly removed coke lead to the steady-state after quick deactivation. Saerens *et al.*[340] focused their studies on the influence of hydrogen co-feeding on the reaction mechanism of PDH. They pointed out that the increasing the co-feeding hydrogen pressure can decrease the coverage of deeply dehydrogenated coke precursors and increase the number of free sites on the Pt(111) surface; moreover, this increase in free sites can lead to higher catalytic activity. The modeling results rationalized the experimental observation of the reduced coke formation and enhanced propylene selectivity by co-feeding hydrogen in PDH.[340,353] By using microkinetic analysis in combination with results from DFT calculations, Xiao *et al.*[365] found that a non-reverse Horiuti–Polanyi mechanism accounts for more than half the propylene production at the under-coordinated active sites that dominate the kinetics of PDH (see Fig. 29), which consists of three dehydrogenation steps that have two β-H and one α-H atoms removed from propane, followed by the hydrogenation of CH_3CCH_2, and at this species the deep dehydrogenation reaction competes with the production of propylene.

The microkinetic modeling of the side reactions of C–C bond cracking and deep dehydrogenation, and coke formation indicates that the catalyst deactivation is due to the formation of CH_3CC^* and C^*, which lead to cracking and eventual coke formation, respectively.[340,353] The formed C1 and C2 species could desorb to form ethane, ethylene, and methane or serve as coke precursors.[340] Then, the formation of coke could block the active sites of the catalyst, impede the catalytic activity, and eventually deactivate the catalyst.[331,353] Lian *et al.* studied the detailed reaction pathway of propylene formation, deep dehydrogenation, and C–C bond cracking for understanding the origin of coke formation.[353] The deep dehydrogenations are *via* R6 → R11 and R10 and finally lead to the cracking of C3 species, mainly starting from propyne (see Fig. 30). The coke precursors are mainly formed during the quick deactivation, and the active sites are mainly occupied by C2 and C1 species, which are hardly removed from the surface. However, the covered active sites, after quick deactivation, can lead to a stable state, which can hinder the side reactions to achieve a stable selectivity. Besides, the co-adsorption of carbon can shift the d-band centers of the surface Pt atoms further below the Fermi level, leading to a decrease in the catalytic activity for PDH.[340] Zhu *et al.* proposed that coke formation is not structure-sensitive, as coke can be formed by all Pt facets and can preferentially cover the under-coordinated active sites.[354] The higher coking rate on small Pt clusters is due to the larger Pt surface area, and the faster coke formation resulted in faster deactivation. Therefore, the rational construction of a Pt surface structure can be a crucial factor in improving catalytic selectivity and controlling coke formation.[353]

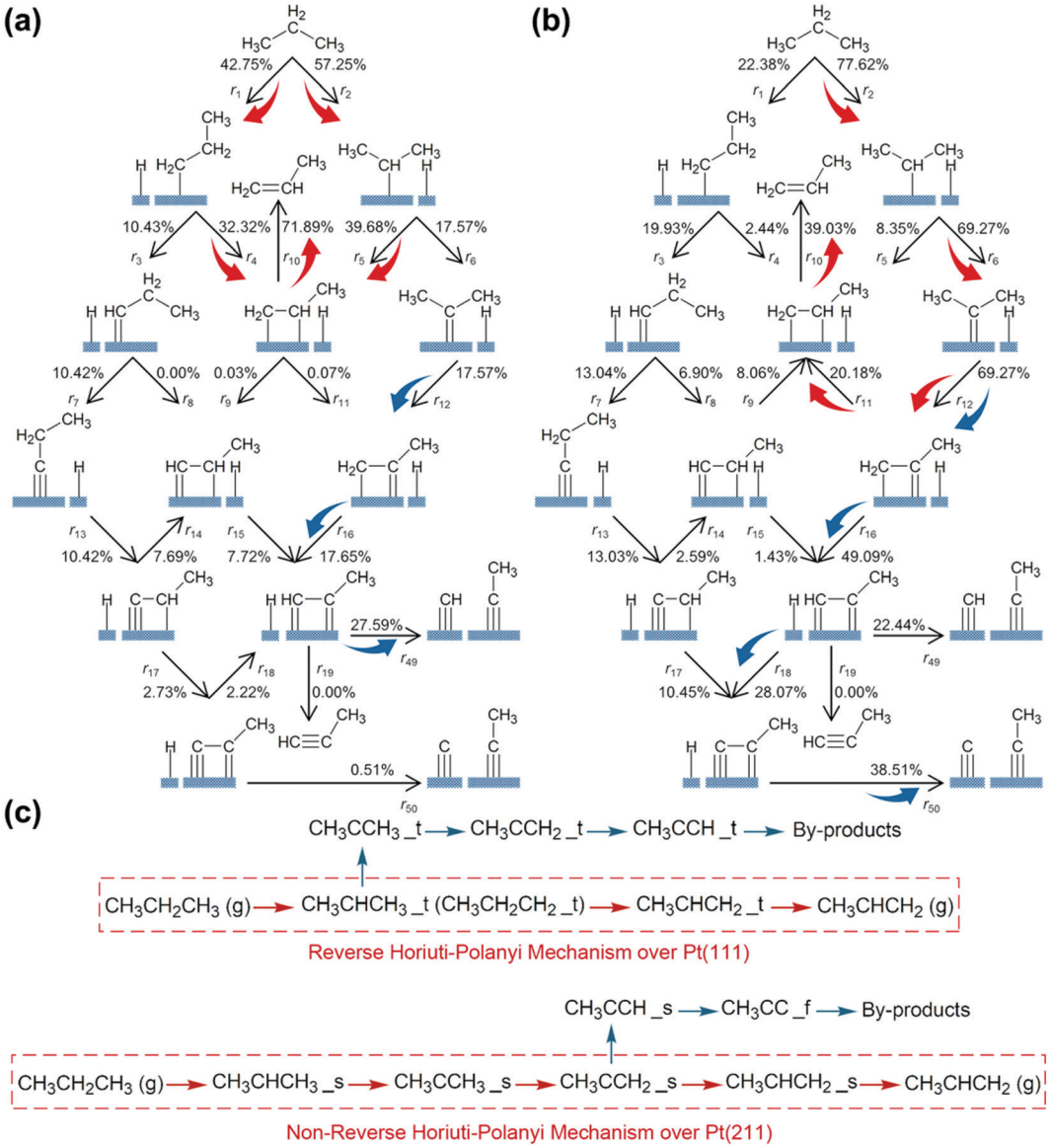

Fig. 29 Flux analysis of PDH under experimental reactor inlet conditions (723.15 K, 0.03 bar propane, and 0.04 bar hydrogen) over (a) Pt(111) and (b) Pt(211) with adsorbate–adsorbate interactions considered. The arrows which are labelled with the percentage of the total reaction flux indicate the direction in which the reversible elementary steps actually proceed. The percentage of the reaction flux is calculated as the absolute value of the net rate for that elementary step divided by the rate for propane consumption. (c) Simplified reaction networks for PDH over Pt(111) and Pt(211).[365] Reproduced from ref. 365 with permission from the American Chemical Society, copyright 2020.

4.1.4 Guidelines for improving the selectivity and coke resistance. The DFT studies by Zhu *et al.* identified propylene as the precursor for the formation of byproducts such as coke.[354] Strong adsorption of propylene means that the surface-adsorbed propylene molecule prefers dehydrogenation to desorption, leading to the deep dehydrogenation and cracking of the subsequent C3 derivatives. The formation of ethane, methane, and coke would lower selectivity to propylene. The critical challenge to gain a high selectivity to propylene and stable catalysts is to weaken the propylene adsorption strength and suppress the deep dehydrogenation on Pt-based catalysts. This provides a guideline for design of PDH catalysts with enhanced catalytic performance.

Under high-temperature reaction conditions, the interaction between Pt and propylene is strong, and side reactions readily occur to form coke and deactivate the catalyst, so the propylene selectivity is around 60–80%, and the catalyst stability is poor.[370] To increase the selectivity toward propylene at relatively high catalytic activity, various attempts have been made to modify the geometrical and electronic structures of Pt-based catalysts,[2,371,372] such as controlling the size and shape of Pt NPs, alloying Pt with TMs or main-group metals, and selecting appropriate catalyst supports. For example, Zhu *et al.* reported that the Pt catalysts of larger cluster sizes with (111) dominating the surface have higher selectivity toward propylene and better stability than the smaller clusters where (211) is dominant on

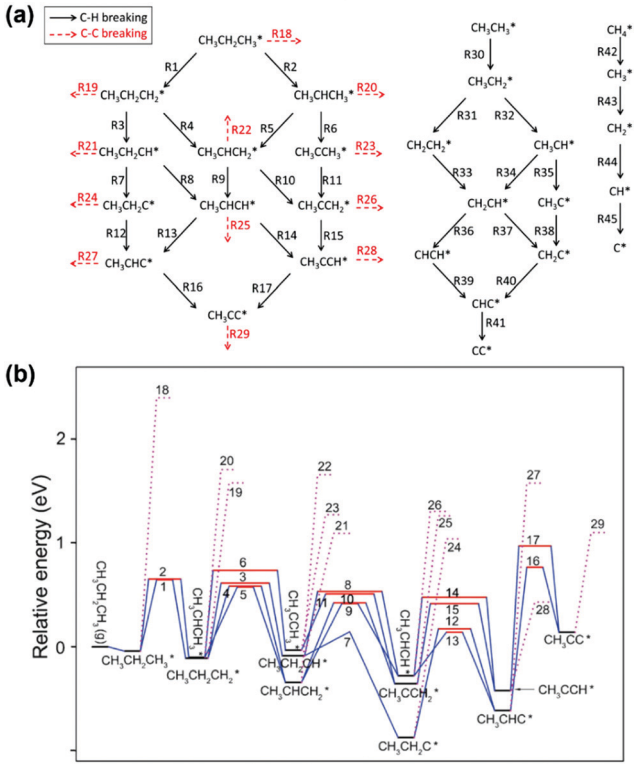

Fig. 30 (a) The network of surface reactions of PDH, not including the adsorption reactions of gases and dissociation of H_2. All elementary reactions are reversible, and asterisks indicate surface adsorbed species.[353] Reproduced from ref. 353 with permission from the American Chemical Society, copyright 2018. (b) Energy profile for propane dehydrogenation on Pt(111) including both the dehydrogenation steps (the solid lines) and the C–C cracking steps (the dotted lines).[347] Reproduced from ref. 347 with permission from the PCCP Owner Societies, copyright 2011.

the surface. This is due to the weakened binding strength of propylene and the higher energy barrier for deep dehydrogenation on Pt(111). Yang *et al.*[354,357] proposed that the introduction of H can decrease the desorption barrier for propylene, and therefore, the selectivity toward gaseous propylene is improved. The Gibbs free energy of the dominant reaction pathways of propane to propynyl ($CCCH_3$) on Pt(111) shows that with increasing H coverage the propylene adsorption strength decreases, while the energy barrier for the further dehydrogenation of propylene increases, leading to a higher catalytic selectivity.[340]

Previous studies have proved that alloying of Pt with one or more TMs, such as Sn, Ti, Ga, Cu, Co, Zn, Ir, and In, is an effective way to improve the catalytic performance in PDH.[2,290,373–377] Among them, Sn is most widely studied due to its application in the industrial process. Yang *et al.*[348] reported that with the increase in Sn content in Pt–Sn alloys, the d-band centers of surface Pt atoms are shifted farther below the Fermi level, as shown in Fig. 31(a), which changes the adsorption properties of Pt. According to the d-band model,[378] downshifting the d-band center of surface atoms would reduce the interaction strength between the surface and adsorbates, whereas upshifting the d-band center of surface atoms may cause the antibonding states to, at least in part, shift up through the Fermi level and become empty, which eventually leads to a stronger binding strength of the adsorbate to the metal surface. Therefore, from the figure, one can see that an upshift of the d-band center gives rise to stronger binding of 1-propyl to the surface and a lower energy barrier for PDH to 1-propyl, which lowers the catalytic activity for PDH. Moreover, the step sites of Pt modified by adding Sn show more profound electron transfer from Sn to Pt on the Pt–Sn alloy surfaces. In addition, the authors also investigated the competition between propylene dehydrogenation and propylene desorption. They found that the introduction of Sn into Pt(111) can lower the energy barrier for propylene desorption and simultaneously increase the activation energy for propylene dehydrogenation (see Fig. 31b). The electronic effect, *i.e.*, the decrease in the interaction energy of the available Pt–Pt di–σ sites, and the geometric effect of the introduced Sn reducing the number of Pt–Pt di–σ sites accessible by propylene can weaken propylene adsorption, leading to a lower desorption barrier than the dehydrogenation barrier of propylene, and thus higher propylene selectivity than Pt(111).[379] By considering the compromise between the catalytic activity and selectivity, the Pt_3Sn bulk alloy is proposed to be the best candidate for PDH. The related experiments also proved that the Sn component added as a promoter in the Pt/γ-Al_2O_3 catalyst can achieve higher propylene selectivity and minimize coke formation.[334,373,380,381] The work also reported that the addition of Sn can help Pt redisperse in the catalyst regeneration by providing nucleation sites on the γ-Al_2O_3 surface to achieve superior catalyst stability.[381]

Similarly, an improved catalytic performance was also reported on the Pt_3Ti catalyst.[382] As shown in Fig. 31(c), the d-band center of Pt(111) is located at −1.97 eV relative to the Fermi level, whereas that of Pt_3Ti(111) downshifts to −2.37 eV due to the strong Pt–Ti d–d orbital coupling, giving rise to weaker adsorption of reaction intermediates and changes in the relative free energy and barriers of the reaction steps during dehydrogenation and side reactions (see Fig. 31d and e). From the figure, one can see that the barrier for propylene desorption on Pt_3Ti(111) is 0.25 eV lower than that on Pt(111), but the energy barrier for deep propylene dehydrogenation is increased by the introduction of Ti into Pt. Moreover, on the Pt_3Ti(111) surface, the C–C bond cracking steps are all endergonic and hence are hindered compared to Pt(111), where C_3H_5* and C_3H_4* cracking are exergonic and much more favorable. These results indicate that Pt_3Ti has higher selectivity toward propylene for PDH compared to pure Pt. Wang *et al.* also studied the effect of Ga as a promoter of Pt/CeO_2–Al_2O_3 catalysts on PDH, indicating that introduced Ga can decorate Pt NPs by forming Pt–Ga alloys and, meanwhile, the Ga component can be incorporated into the cubic fluorite structure of CeO_2. The metal Ga promoter on Pt–Ga alloys can decrease the size of Pt ensembles or block the low-coordinated defect active sites, lower the desorption barrier of propylene and coke precursors by donating electrons to Pt atoms, and thus suppress undesirable side reactions to achieve better propylene selectivity. Besides, the

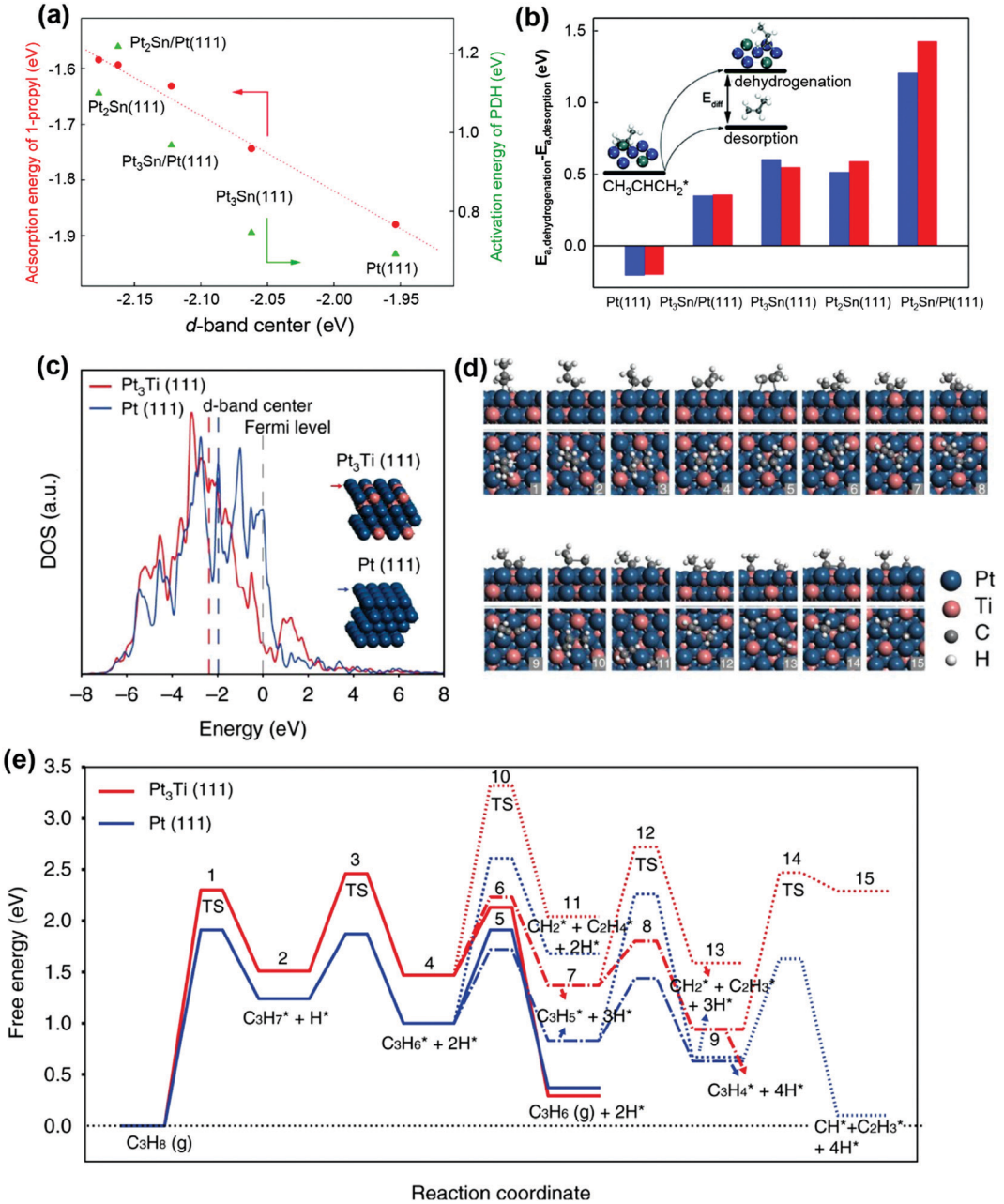

Fig. 31 (a) Plots of the binding energies of 1-propyl (red dots) and the energy barriers for propylene dehydrogenation to 1-propyl (green dots) against the d-band centers over Pt(111) and PtSn surfaces. (b) Energy barrier difference (E_{diff}) between propylene dehydrogenation and propylene desorption. Blue and red bars indicate pathways to 1- and 2-propenyls, respectively.[348] Reproduced from ref. 348 with permission from the American Chemical Society, copyright 2012. (c) DFT calculated projected DOS for the 5d orbitals of Pt in the top-layer $Pt_3Ti(111)$ and Pt(111). (d) Optimized structures as numbered in (e) from the side and top views (H* is not shown). (e) Free energy diagrams of relevant (side-)reaction steps in PDH on $Pt_3Ti(111)$ and Pt(111) surfaces. The dotted lines denote the C–C cracking of C_3H_6*, C_3H_5*, and C_3H_4*, and the dashed-dotted lines denote the deep dehydrogenation of C_3H_6* and C_3H_5*.[382] Reproduced from ref. 382 with permission from Springer Nature, copyright 2018.

promoter towards CeO_2 can enhance both lattice oxygen storage capacity and surface oxygen mobility to increase the reducibility of CeO_2 and consequently reduce the coke deposition and improve the catalyst stability.[376]

Besides, the addition of one or more main-group metals or TMs, such as Sn, In, Cu, and Ga, is also an effective way to reduce the tendency to form coke.[343,350,361,362] The dopants can promote the dispersion of Pt particles and thus prevent their sintering, suppress the structure-sensitive side reactions including hydrogenolysis and deep dehydrogenation to reduce the rate of carbon deposition, and promote the migration of carbon deposition from active metal components to the carrier, *etc.*[380,383,384]

In addition, some novel core–shell Pt-based catalysts can not only improve the catalytic performance but also effectively increase the utilization efficiency of precious metals. Note that

near-surface alloys (NSAs) having a host metal (such as Pt) as the subsurface and solute metals as the overlayer exhibit unique chemical and physical properties distinct from those of their constituent metals. Xiao *et al.*[331] reported that by substituting late TMs for the Pt atoms in the core region, the adsorption and catalytic properties of the surface Pt atoms in M@Pt core–shell catalysts could be tuned, which is attributed to the modification of the electronic structure of metal surfaces through the strain effect and electron transfer. The core–shell catalysts were found to have less negative propylene adsorption energies and higher activation energies for the dehydrogenation reactions than Pt, thus giving rise to lower catalytic activity and a higher selectivity toward propylene, as shown in Fig. 32(a). This figure also indicates that higher catalyst selectivity toward propylene can be attained at the expense of a lower catalytic activity for PDH. Co@Pt is proposed to be the best core–shell catalyst for PDH if a compromise is made between catalytic activity and catalyst selectivity. Cesar *et al.*[370] prepared bimetallic Pt–Co NPs for PDH with and without added H_2 and studied the effect of the Co loading amount on the core structure from Pt to Pt_3Co to PtCo. The result shows that bimetallic NPs have significantly better olefin selectivity than either single metal, suggesting that Co that acts as a less active promoter can utilize the geometric effects to enhance the selectivity by breaking up large Pt ensembles in the bimetallic catalysts. Therefore, through the experimental exploration for Pt–Co alloy catalysts, it is found that the catalysts exhibit superior PDH performance, especially catalytic selectivity, consistent with the results obtained by Xiao *et al.*[331] Besides, Sun *et al.*[385] pointed out that the isolated Pt atoms dispersed in Cu

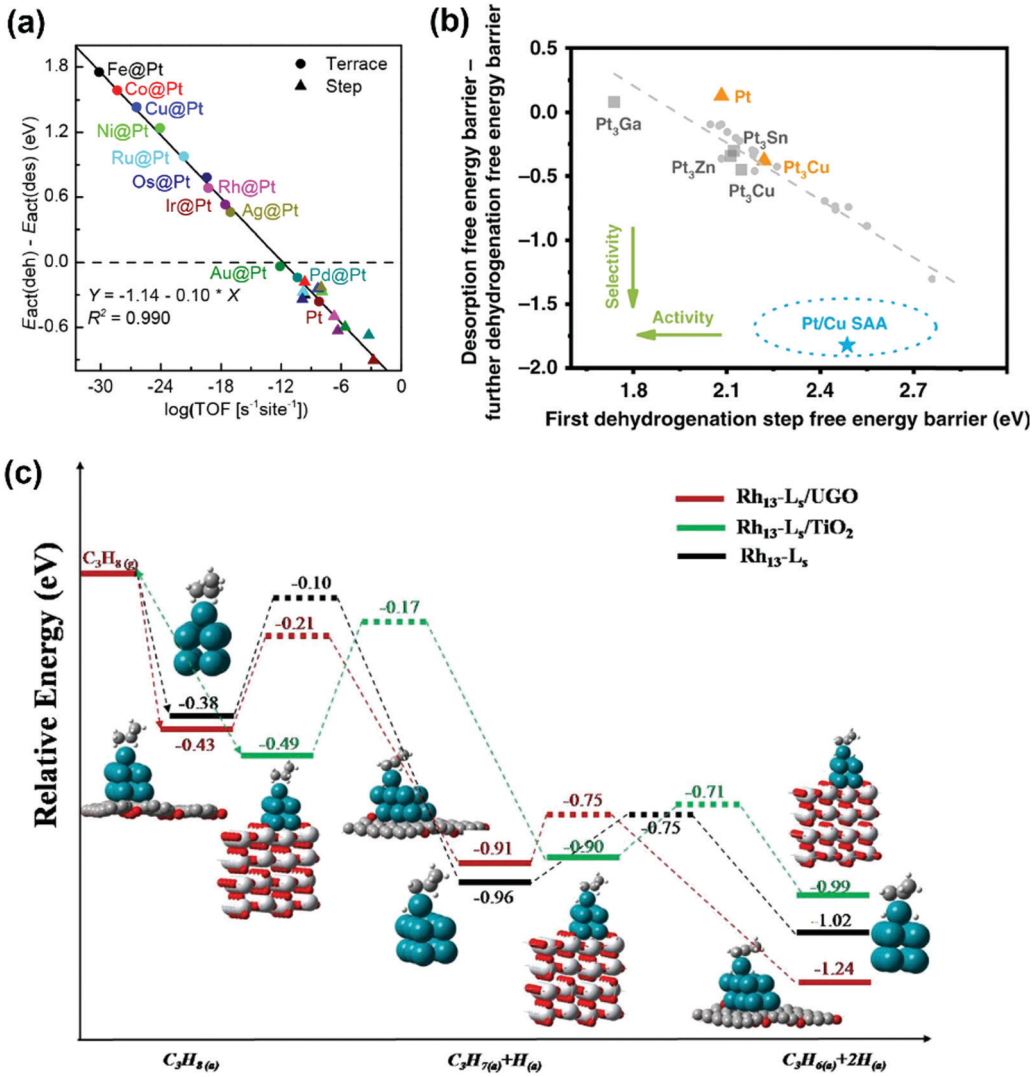

Fig. 32 (a) Linear scaling relation between catalytic activity and selectivity for PDH over 12 core–shell alloy catalysts.[331] Reproduced from ref. 331 with permission from Elsevier, copyright 2019. (b) Screening of Pt-based bimetallic catalysts for PDH, where SAA denotes the single atom alloy.[385] Reproduced from ref. 385 with permission from Springer Nature, copyright 2018. (c) Profiles of the potential-energy surface for PDH on Rh_{13}-L_s, Rh_{13}-L_s/UGO and Rh_{13}-L_s/TiO_2, where Rh_{13}-L_s is the low-symmetry Rh_{13} cluster and UGO is the unzipped graphene–oxide.[386] Reproduced from ref. 386 with permission from the PCCP Owner Societies, copyright 2017.

NPs can break the PtM alloy scaling relationship, which is different from the scaling for conventional Pt alloys during the PDH (see Fig. 32b). In other words, the Pt/Cu single atom alloy maintains a reasonable dehydrogenation activation barrier and at the same time displays quite a high selectivity, which is reflected by the low free energy barrier difference between the propylene desorption and deep dehydrogenation. Therefore, the use of dopants can improve the selectivity of Pt-based catalysts, suppress catalyst deactivation, and extend the use time of catalysts.

Moreover, selecting suitable catalyst supports is also an effective way to modify the catalytic performance of metal catalysts for PDH.[387,388] Chang *et al.*[386] investigated the PDH over Rh_{13}-L_s (low-symmetry Rh_{13} cluster), Rh_{13}-L_s/UGO (Rh_{13}-L_s cluster supported on a sheet of unzipped graphene oxide), and Rh_{13}-L_s/TiO_2 catalysts. They found that although electrons flowed from the Rh_{13} cluster towards both supports, the UGO support induced an electronic redistribution of the Rh_{13} cluster rather than just abstracting electronic charge from the Rh_{13} cluster to the support, as compared with the TiO_2 counterparts. UGO would induce an electronic accumulation onto the top area of the Rh_{13} cluster, while TiO_2 induced electronic depletion, which dictates different results for PDH. As shown in Fig. 32(c), for the Rh_{13}-L_s/UGO system, the energy barrier for the dehydrogenation of propane to propyl is 0.22 eV, and the calculated energy barrier for the dehydrogenation of propyl is 0.16 eV. UGO as a support could lower the energy barriers for both two dehydrogenation steps of propane, but TiO_2 as a support increased the energy barriers for both dehydrogenation steps, indicating that the UGO sheet is a more suitable support for the Rh_{13}-Ls cluster and for activation of the C–H bond in PDH. Besides, Jiang *et al.*[389] found that the addition of an appropriate amount of TiO_2 in Pt/TiO_2–Al_2O_3 catalysts can improve propylene selectivity and catalyst stability. The reasons are that the electrons could be transferred from the partially reduced TiO_x ($x < 2$) to the Pt atoms, and the partial coverage of the metal surface by TiO_x species, and thus the increased electron density of Pt can hinder propylene adsorption on active metal sites and facilitate coke migration from the active sites to the carrier.

4.2 C–H oxidative activation on metal oxides

Although the direct dehydrogenation of propane to propylene (PDH) is a rather promising solution, the ODH of propane has some advantages: ODH is thermodynamically favored even at low temperatures and can avoid the formation of coke.[303,390,391] Besides, unlike the PDH reaction, the ODH of propane is mainly based on the following two mechanisms: first, lattice oxygen is involved in the reaction, and then the oxygen vacancies formed can be filled by the added oxidants (removal of lattice oxygen anions and their reinsertion); second, lattice oxygen is not involved in the reaction; however, the oxidants can be adsorbed on the surface to react with the reactants or intermediates.[392,393] Supported vanadium oxides are known to be one of the best catalysts for the ODH reaction with high thermal stability and a relatively large surface area. Several research groups have studied the mechanism of ODH reaction on metal oxide catalysts, usually following the MVK redox mechanism involving lattice oxygen in C–H bond activation.[394–396] This redox mechanism mostly occurs on transition-metal oxide catalysts with relatively high reducibility. It can be generally described as a two-step mechanism: (1) the reduction of the oxide surface by the dehydrogenation of the hydrocarbon – the catalyst in the oxidation state activates the C–H bond and therefore the dissociated H atoms combine with the lattice oxygen atoms to desorb in the form of H_2O; and (2) the subsequent reoxidation by gas-phase oxygen – the generated oxygen vacancies complete the circulation process of the catalyst surface under the action of oxygen.[29,397,398] The C–H bond activation in propane on (un)supported metal oxides such as VO_x, Cr_2O_3, ZnO, V_2O_3, and Ga_2O_3[2,303,339,391,399–406] has been studied theoretically by using DFT calculations in which the active sites and reaction mechanism were focused. The reduction step has comprehensively been studied, and the full catalytic cycle is not considered because the oxidation of the substrate is typically a fast step.[336]

4.2.1 VO_x catalysts. The V_2O_5(001) surface is the most stable surface exposed in crystalline V_2O_5 formed at high vanadium loadings. It is generally accepted that there are three types of lattice oxygen on V_2O_5(001), which are singly coordinated terminal oxygen (O1), twofold-coordinated oxygen (O2), and threefold-coordinated oxygen (O3), as shown in Fig. 33. Previous experimental and theoretical studies have proposed that the terminal O1 and the bridging lattice O2 serve as the active sites assisting in the C–H bond activation in propane,[399,407] which is in good agreement with the DFT calculations by Fu *et al.*[303] They reported three possible C–H activation mechanisms for the oxygen-assisted first C–H bond activation over the V_2O_5(001) surface, including oxo-insertion, concerted, and radical mechanisms (see Fig. 34a). The reaction mechanism depends on the identity of the active sites. It was found that both the radical and oxo-insertion mechanisms are feasible at the O1 sites, while only the oxo-insertion mechanism is preferred at the O2 sites. In addition, the activation energies for C–H activation for the secondary C–H bond are lower than those for the primary C–H bond, in agreement with the order of the C–H bond dissociation energies in propane.

The reactivity of O sitting on V_2O_5(001) follows the order of $O_1 > O_2 > O_3$. The energy barriers of activation of the first C–H bond in propane are 1.18 and 1.32 eV at the O_1 and O_2 sites, respectively, as shown in Fig. 34(b). The threefold-coordinated oxygen (O_3) is the least active for C–H bond activation and almost inert.[303] The *i*-propoxide can much more easily further decompose into propylene at the O_2 site, releasing an H atom to a neighboring O_2 or O_3 atom, and the corresponding energy barrier is 0.95 eV lower than that at the O_1 site (>1.30 eV). The H_2O formation through the recombination of two OH groups at the O_1 site is facile, and H_2O desorption is endothermic with a relatively low reaction energy of 0.56 eV, leading to the formation of oxygen vacancies on the oxide surface. As the lattice oxygen is removed, the structure of the catalyst may collapse, indicating that the V_2O_5(001) surface is fully dynamic.

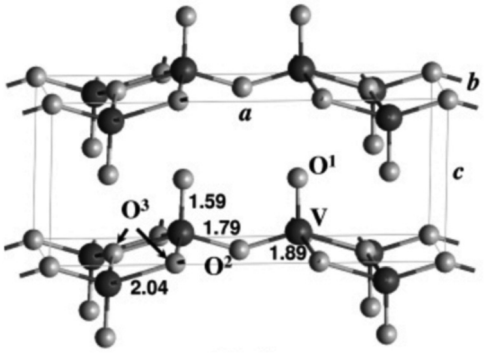

Fig. 33 V_2O_5 bulk surface.[408] *a*, *b*, and *c* of the orthorhombic unit cells are parallel to the (100), (010), and (001) directions, respectively. V atoms are depicted as the white circles and O atoms as the smaller gray circles. O_1, O_2, and O_3 denote the single, 2-fold, and 3-fold coordinated oxygen atoms, respectively. Bond lengths in Å. Reproduced from ref. 408 with permission from the American Chemical Society, copyright 2005.

For the second H abstraction step, the reaction energy is −1.58 eV, and the estimated activation barrier is 0.65 eV, where the surface reconstruction is not taken into account.[399,409] Gas-phase reactions of propane with VO_2^+ and $V_3O_7^+$ have also been studied.[410,411] When considering the more complex reaction conditions of vanadium oxide catalysts involving supports and O_2 adsorption, some of the energy barriers could be affected, such as propane adsorption and H_2O elimination. However, the terminal O_1 is too active to release propylene and therefore shows poor propylene selectivity.

4.2.2 Supported VO_x catalysts. For supported VO_x catalysts, the effect of supports and VO_x dispersion for propane ODH has been widely studied.[15,404,412] The binding strength of the surface lattice oxygen in the VO_x surface species is a key parameter that governs the activities and selectivities for propane ODH.[406]

Active sites. Depending on the loading of VO_x on the support, the VO_x can present as an isolated monomer, dimer, and polymer (sub-monolayer, a monolayer) and crystalline structure.[404,413] Three types of lattice O are identified, such as (a) terminal V=O sites, (b) bridging V–O–V sites, and (c) V–O–support sites.[403,414] The active sites depend on the catalyst structure on the surface. On the supported monomeric VO_x, there are two different types of available active O sites, namely terminal V=O sites and V–O–support interface sites. For the dimer and polymer VO_x, there are additional bridging V–O–V sites. Activation of propane requires a pair of oxygen sites denoted as O_A–O_B as the active sites, where V is inert.[414] The active sites are highly dynamic, and there are a large number of combinations of two oxygen sites among the three O sites.

Activation of propane and propylene. The activation of propane has been studied on the isolated monomeric O=V(O–)$_3$ supported on SiO_2,[401] a VO_x monolayer on TiO_2(001),[403] and monomeric and dimeric VO_x species supported on the (001) and (100) surfaces of anatase TiO_2.[414] Regardless of the supports, propane undergoes preliminary weak physical adsorption on the surface prior to dissociation. Unlike the non-selective activation on the metal surfaces, the secondary C–H bond activation is energetically preferred compared to the primary C–H bond activation, in agreement with the order of the C–H bond dissociation energies in propane. C–H bond activation follows similar mechanisms on the unsupported V_2O_5(001). The activation energies for hydrogen abstraction are almost the same at the different active sites of the unsupported catalyst, *i.e.*, O1 ≈ O2 ≈ O3, while they increase in the order O1 < O2 < O3 on the supported catalyst.[403]

On the supported VO_x monolayer on TiO_2(001), the C–H bond activation in propane is *via* a concerted mechanism at the V–O site, leading to the formation of the metal hydride and adsorbed propoxide.[403] The vanadyl site (V=O) is the most active site on V_2O_5(001) and V_2O_5/TiO_2, while the bridging V–O–V sites are more selective towards propylene. The rate-limiting step of oxidative PDH is the activation of propane *via* a direct H abstraction from the methylene C–H, based on the reaction path analysis at 0 K. The TiO_2 support enhances the C–H bond activation as compared to unsupported V_2O_5 by lowering the activation energy of the RDS as shown in Fig. 35 and influences

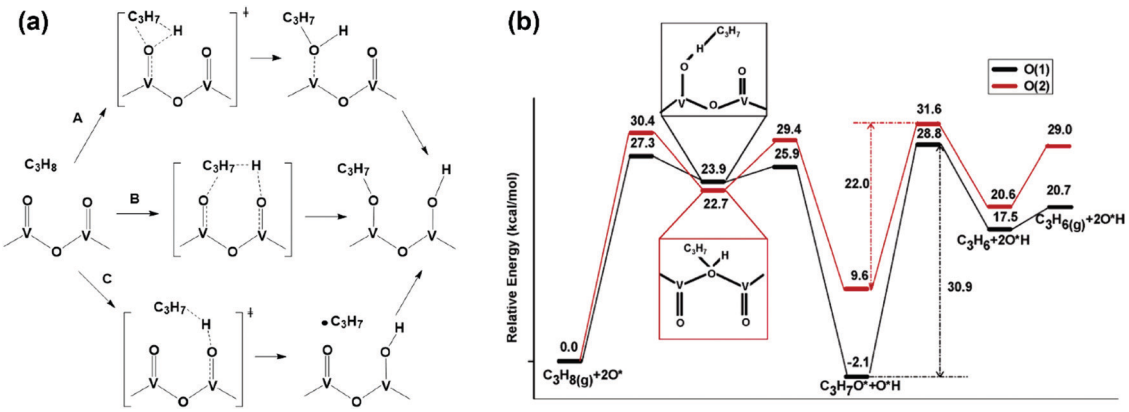

Fig. 34 (a) Three homolytic cleavage mechanisms for the C–H bond activation of propane: an oxo-insertion mechanism (A), a concerted mechanism (B), and a radical mechanism (C); and (b) lowest-energy pathways of the propane ODH process that occurred on O_1 and O_2 on the V_2O_5(001) surface.[303] Reproduced from ref. 303 with permission from the American Chemical Society, copyright 2006.

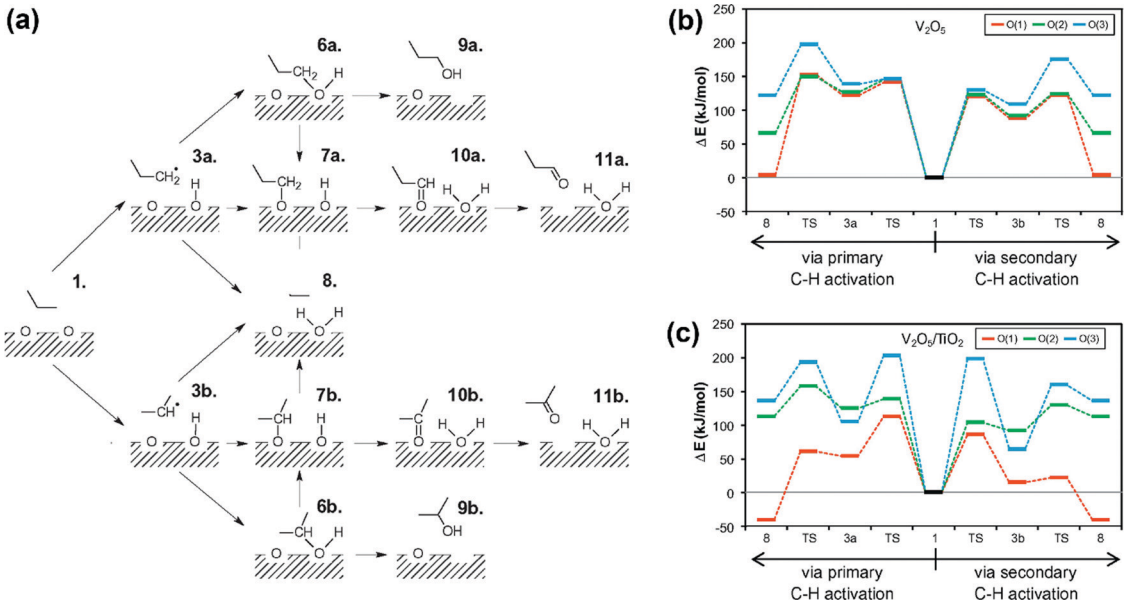

Fig. 35 (a) Investigated pathways for propane oxidation over the vanadia surface; the corresponding energy diagrams for propane oxidation to propylene on (b) V_2O_5 and (c) V_2O_5/TiO_2.[403] Reproduced from ref. 403 with permission from Elsevier, copyright 2012.

the selectivity of the supported monolayer VO_x catalyst towards propylene production rather than propanol and acetone.

The VO_x monomers and dimers supported on SiO_2 have also been studied by Rozanska *et al.*[415] The first H abstraction from propane is the RDS and yields activation barriers at 750 K, which are lower for dimeric VO_x (1.18 eV) than for monomeric VO_x (1.29 eV). Using the reaction energy as a reactivity descriptor, the energy barriers for propane ODH decrease with increasing VO_x coverage from dimers to larger oligomers. Besides, V^V/V^{IV} redox cycles are preferred over V^V/V^{III} cycles.

Dependence of activity on supports and cluster size. Various oxides such as TiO_2, SiO_2, CeO_2 and γ-Al_2O_3 have been studied as the supports of VO_x.[394,416–418] The activity of the active sites in VO_x depends strongly on the supports, which is ascribed to the electronic modification of active oxygen sites.[414] TiO_2 is the most widely studied support owing to the highest activity of VO_x/TiO_2. Du *et al.* observed that propane ODH activity can be tuned by supporting on anatase TiO_2 surface and changing VO_x dispersion.[414] The activation energy of the first C–H activation and the formation energy of propylene on the monomeric and dimeric VO_x species supported on the anatase $TiO_2(001)$ and (100) surfaces are summarized in Table 4.

By comparing the energy barrier of the first C–H activation step and the overall energy barrier of propylene formation on $TiO_2(001)$ and (100) surfaces given in Table 4,[414] it can be seen that the catalysts supported on the (100) surface show higher activity than those on the (001) surface. For the monomer, dimer, and monolayer of VO_x, the valence bond formed at the interface of VO_x and support surfaces. The interface electronic transfer resulted in the modification of the electronic structure of VO_x species, as evidenced by the projected p-DOS plots where the centers of the valence bands of the $VO_x/TiO_2(100)$ surfaces are closer to the Fermi level than those of the $VO_x/TiO_2(001)$ surfaces. This is also reflected in more negative Bader charges of oxygen sites on the (100) than (001) surfaces. This indicates that the oxygen sites are the nucleophilic centers to attack the positively charged H atoms and activate the C–H bond. The stronger basic oxygen sites with more negative charges in VO_x supported on (100) attack more efficiently the acidic C–H bond, and thus result in higher activities than those on the (001) surfaces. In addition, the support changed the relative charge of the oxygen sites. For example, the higher activity of the terminal V=O sites than that of the V–O–Ti interface sites on the dimeric $VO_x/TiO_2(001)$ can be ascribed to the more negatively charged O on the former sites.

Table 4 A summary of the active oxygen sites and energetics for the most feasible pathways of propane ODH reaction on the four catalysts[a].[414] Adapted from ref. 414 with permission from Elsevier, copyright 2013

	$VO_x/TiO_2(001)$		$VO_x/TiO_2(100)$	
	First C–H activation	Propylene formation	First C–H activation	Propylene formation
Monomer	O_{V-Ti} (1.58)	R: O_{V-Ti} (1.83) C: O_{V-Ti} (1.85)	$O_{V=}$ (1.37)[1.14] O_{V-Ti} (1.36)[1.19]	R: O_{V-Ti} (1.86)[1.65] C: O_{V-Ti} (1.86)[1.69]
Dimer	$O_{V=}$ (1.62)	C: O_{V-Ti} (2.02)	$O_{V=}$ (1.05)[0.86]	C: O_{V-Ti} (1.19)[1.08]

[a] R represents the radical propyl mechanism and C represents the concerted propoxide mechanism. Values in the brackets for the monomeric and dimeric $VO_x/TiO_2(100)$ surfaces are ZPE corrected (unit: eV).

A comparative study of PDH on monomeric and dimeric VO_x supported on γ-Al_2O_3 and V_2O_5 crystal, as shown in Fig. 36, revealed that the cluster size has a remarkable influence on the relative activity of oxygen sites and the rate-determining step.[404] The first C–H bond activation has a lower activation barrier than the secondary C–H activation on the supported V_2O_5, while both C–H bond activations have similar energy barriers on the supported VO_3. Besides, the O p-band center could correlate with the dehydrogenation barrier of the O sites to predict the dehydrogenation activity. Luo *et al.* also reported that mixed CaO and γ-Al_2O_3 supported VO_x is beneficial to the propylene formation compared to pure CaO supported VO_x, which is attributed to the moderate level of acidity and metal–support interaction.[419]

Moreover, p-DOS analysis suggests that the electronic structure depends on the VO_x cluster size or dispersion, which rationalizes the activity dependence of the cluster size of VO_x on the support. The monomer dispersed VO_x is more active than the dimer dispersed VO_x on the TiO_2(001) surface, while the dimer dispersed VO_x is more active than the monomer dispersed VO_x on the TiO_2(100) surface.[414] Cheng *et al.*[420] reported that the coordination number of the vanadium atom was the key structural parameter in predicting the catalytic activity, showing that the activation energy of the first dehydrogenation step for propane on anatase-supported vanadium oxide monomers and dimers is 1.73 eV and 1.91 eV, respectively.

The above discussion reveals that the support surface and the dispersion of the VO_x catalyst change the electronic properties of the oxygen sites and thus change their activity in activating the C–H bond of propane. The oxygen activity in VO_x seems to be of vital importance for C–H bond activation.

The activity of the lattice oxygen can also be described by the formation energy of the oxygen vacancy. The formation energy of surface oxygen vacancy can be identified as a dominant parameter in determining the adsorption mode and the catalytic activity of metal oxides.[421] Li *et al.* reported that the formation energy of surface oxygen vacancy could be used as a descriptor to explain the adsorption behaviors, which is more sensitive to the change in the electronic structure of perovskites, arising from the fact that the actual partial charges the oxygen and transition-metal ions carry determine

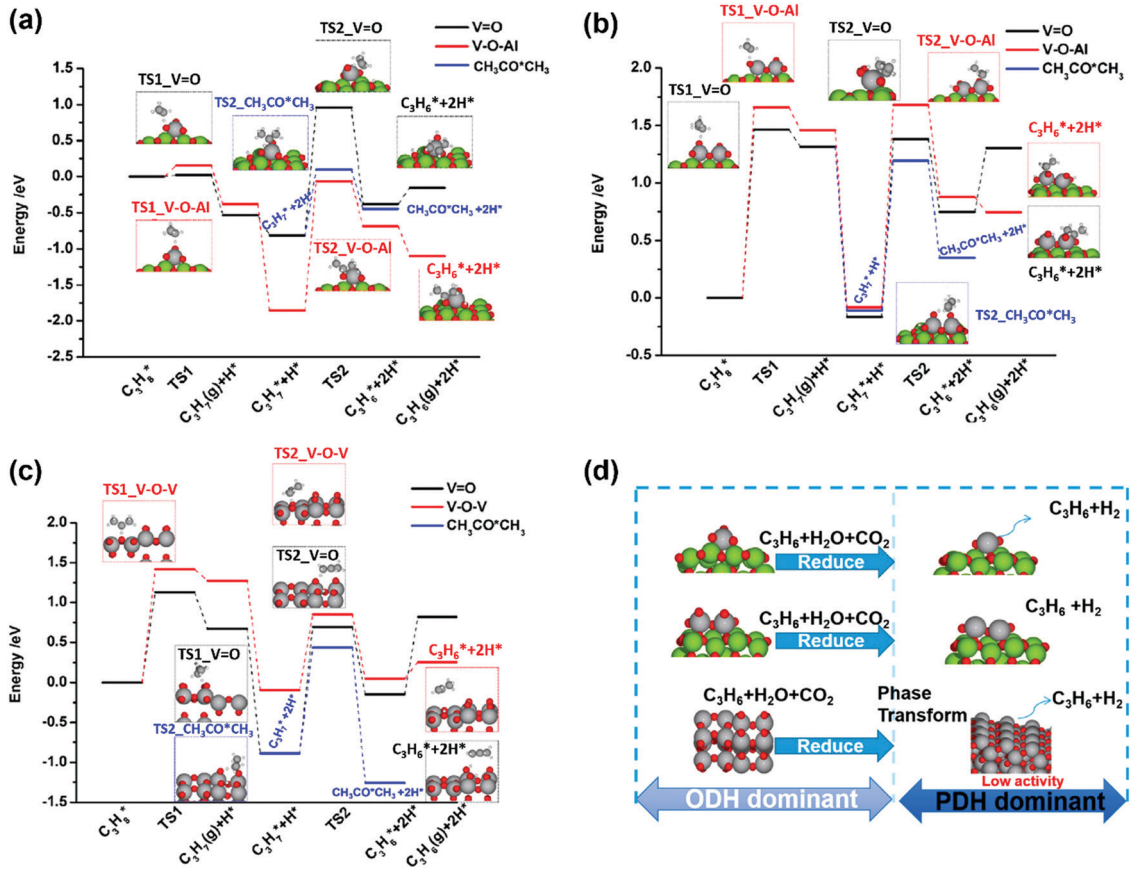

Fig. 36 Reaction energy profiles of C_3H_6* formation and CH_3COCH_3* formation by two successive H ruptures of C_3H_8* over (a) supported monomeric VO_3/Al_2O_3, (b) supported dimeric V_2O_5/Al_2O_3, and (c) slab V_2O_5(001) surfaces. (d) Proposed reaction mechanisms over the different degrees of vanadium polymerization in different periods of reaction. The structures of transition states and adsorbed C_3H_6* are shown in the diagram. The black line denotes the C–H rupture by the V=O bond, while the red line denotes the C–H rupture by V–O–Al (or by the V–O–V bond). The blue line denotes the CH_3CO*CH_3 formation catalyzed by the V=O bond. The structures of transition states and adsorbed C_3H_6* are shown in the diagram. Color scheme: H white; Al green; V gray; O red; C gray.[404] Reproduced from ref. 404 with permission from the American Chemical Society, copyright 2019.

Table 5 Calculated oxygen vacancy formation energies (eV) on unsupported and supported VO_x. O_1, singly coordinated vanadyl O; O_2 or O_2–support, doubly coordinated bridging O; O_3 or O_3–support, triply coordinated bridging O

	$O^* \rightarrow * + 1/2O_2(g)$					
Model	O_1	O_2	O_3	O_2–support	O_3–support	Ref.
$V_2O_5(001)$	2.04	3.37	3.78	—	—	403
V_2O_5/TiO_2	2.44	4.50	3.49	—	—	
$V_2O_5(001)$	1.67	3.30	—	—	—	413
VO_3/TiO_2	1.86	—	—	0.77	—	
V_2O_5/TiO_2	2.63	—	—	2.76	2.23	
V_3O_6/TiO_2	2.86	4.16	—	2.85	4.29	
V_4O_8/TiO_2	2.68	3.92	—	—	—	
1 mL VO_x/TiO_2	2.89	4.77	—	—	—	
Monomeric $OVSi_7O_{12}H_7$	2.98	—	—	—	—	423
Dimeric $O_2V_2Si_6O_{12}H_6$	2.87	—	—	—	—	
Octameric V_8O_{20}	2.65	—	—	—	—	

the adsorption behaviors of the oxygen and transition-metal ions.[422] The estimated formation energies of oxygen vacancy of VO_x are summarized in Table 5.

When going from monomeric through dimeric and eventually to octameric VO_x species, the reaction energy for VO_x species yielding an O defect site changes from 2.98 through 2.87 and eventually to 2.65 eV, as shown in Table 5, while the reaction energy for H abstraction in propane at the corresponding V=O site decreases from 1.06 through 0.90 and eventually to 0.52 eV.[415,423] The lower formation energy of oxygen vacancy corresponds to a higher oxygen activity. Likewise, the TiO_2 support lowered the formation energy of oxygen vacancy, thus increasing the activity. The formation energy of the oxygen vacancy can therefore be used as a descriptor when searching for new catalysts for ODH of propane.

Dependence of activity and selectivity on the cluster size and valence state. The selectivity of propylene remains a challenge in ODH of propane. A study of deep oxidation of propane to CO_2 on $V_2O_5(001)$[424] revealed that the terminal V=O sites are the active sites for the formation of acetone from *i*-propoxide and the further combustion of acetone to CO_2. The V–O–support is the main active site for propylene formation. It provides a guideline for the rational design of new catalysts with improved selectivity. The ratio of the terminal V=O to the other two oxygen sites is a key parameter in the catalyst design. Small cluster VO_x with a low V=O ratio could increase the propylene selectivity at the expense of lowering the activity, while polymeric VO_x with a high V=O ratio could lower the propylene selectivity. The cluster size needs to be compromised between the activity and selectivity, and sub-monolayer VO_x could provide a high propylene yield, which has been very recently confirmed experimentally by Gong and coworkers.[413]

Very recently, Xiong and co-workers found that the PDH reaction can be divided into two periods in the VO_x reduction by propane: the initial ODH dominant period leading to propylene, water and CO_2 formation and the non-ODH dominant period (see Fig. 36d).[404] Over γ-Al_2O_3 supported VO_x, the V=O mainly contributes to H_2O and $CH_3CO^*CH_3$ formation and deep oxidation to CO_2 in the ODH dominant period. With the consumption of the V=O during the reaction, the Al–O–V sites become dominating active sites for propylene formation. Note that the PDH ability should be related to their corresponding valence state.[420,425] It has been illustrated that the oxygen vacancy modified the electronic structure of active species and even change the reaction mechanism.[426]

Gas-phase O_2 in the reactant mixture reoxidizes the reduced V species and removes carbon deposits. The lattice O of VO_x species provides pathways toward desired propylene formation, while the surface O mainly forms undesired CO_x species. Propane conversion and the propylene yield could be described by a kinetic model including propane ODH, parallel propane combustion, and sequential propylene combustion. Propylene is the most abundant primary product. CO and CO_2 are formed by the secondary combustion of propylene, which is the main source of carbon oxides in the studied reaction, and CO_2 also forms by direct combustion of propane.[335,427,428] The activation energies of CO and CO_2 formation from secondary propylene combustion are less than the activation energy for propylene formation on TiO_2/SiO_2-supported VO_x catalysts, leading to the inverse conversion *versus* selectivity relationship.[429] This result is different from the energy profiles for propane ODH and propylene combustion over VO_x/Al_2O_3 catalysts, as shown in Fig. 37.[15] The C–H bond activation and the recombination of the remaining OH groups to form H_2O are irreversible.[427,428] For the propane ODH reaction over VO_x involving the participation of the O_2 molecule, the energy barriers for H_2O elimination on the surface can be reduced.[409] The rate of propane ODH reaction is proportional to C_3H_8 partial pressure and independent of O_2 partial pressure in the limit of very low H_2O concentrations, and therefore propane activation is a kinetically relevant step. However, the rates acquire a more complex dependence on C_3H_8 and O_2 pressures when H_2O is present at higher concentrations. On V_2O_5 powders and supported VO_x, the dependencies of reaction rates on C_3H_8, O_2, and H_2O concentrations are identical, indicating that both surfaces have similar active centers.[427]

In addition to these studies, significant efforts have been devoted to improving the activity of the different O sites for propane ODH of the supported VO_x catalyst. Alkali metal additives have been found to improve the propylene selectivity

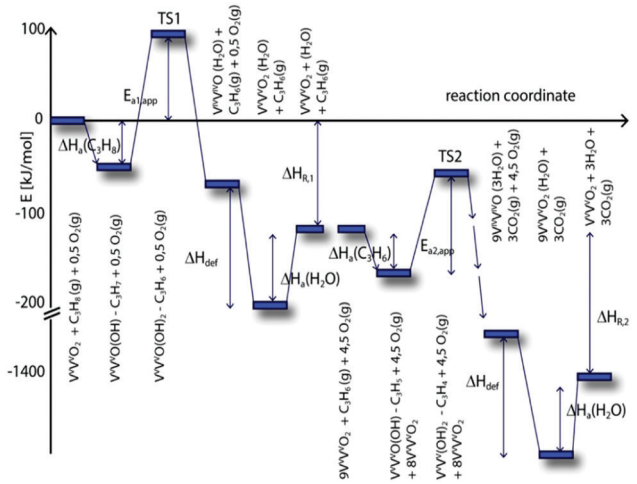

Fig. 37 Energy profile for propane ODH (left) and rate determining step of propene combustion over VO_x/Al_2O_3 catalysts.[15] Reproduced from ref. 15 with permission from the American Chemical Society, copyright 2014.

for propane ODH on V-based and Mo-based catalysts; the effect is explained by a modification of the acid–base properties of the catalysts.[335,430–432] On VO_x/SiO_2 catalysts, the potassium additive by blocking active centers on the catalyst surface exhibits a strong inhibitory effect on the consecutive propylene and parallel propane combustion and has a lower influence on ethylene and ethane combustion.[335] Thus, potassium does not change the ethylene selectivity but has a distinct influence on the propylene selectivity, and thus leads to high initial selectivity (−95%). Zhao *et al.*[433] also reported that OH groups on supported VO_x catalysts can lead to lower PDH activity and less coke formation by combined experimental and calculational studies, but the fresh VO_x catalysts under a C_3H_8 atmosphere are directly reduced to V_2O_3.

4.2.3 Other catalysts. Other types of catalysts, such as Cr-based catalysts, Ga-based catalysts, Mo-based catalysts, and mixed metal oxides, have also been studied in the ODH of propane, and these catalysts generally permit the redox mechanism to occur without structural collapse.[72,393] However, most of these studies mainly involve experimental findings due to the complexity of the metal oxides, including the different crystal structures, the oxidation states, and the surface facets.[337,338,434–437] Liu *et al.*[402] studied PDH on perfect $Ga_2O_3(100)$ by DFT calculations. The bridge-bound surface O sites are active for cleaving the C–H bonds in propane, and thus rather stable OH groups are formed on the surface. The initial C–H bond activation of propane energetically prefers the radical mechanism and shows a rather low energy barrier (0.78 eV) at the surface O sites. Propylene can be formed through H abstraction from physically adsorbed propyl radicals or from propoxide and propylgallium intermediates. Besides, propylene at the surface O sites has high adsorption energy, which tends to be further dehydrogenated or oligomerized, leading to catalyst deactivation. Once the surface O ions are blocked or consumed by the H atoms, the Ga sites will become the main reaction sites to catalyze the further dehydrogenation reactions and H abstraction by Ga sites needs to overcome high energy barriers to form gallium hydrides (GaH). However, the formation of H_2 from the GaH and OH groups is much easier. Therefore, the RDS changes from H abstraction by oxygen sites at the initial reaction stage to H abstraction by Ga sites from various propyl sources to form GaH. On the $Ga_2O_3(100)$ surface, it is difficult for the H atoms in the OH groups to form H_2 or H_2O. Since it is also possible to generate gaseous H_2O at high temperatures, the reaction would follow an ODH mechanism comprising H_2O at the initial stage and follow a PDH mechanism forming H_2 at the steady stage.

Fu *et al.*[400] also reported that the initial propane activation on molybdenum oxides follows the same ODH mechanism as V-based catalysts in that lattice oxygens participate the C–H activation, where 6 possible mechanisms of the C–H bond activation on metal oxides are considered on Mo_3O_9, leading to 17 transition states involving C–H activations from the methyl and methylene groups in propane. For example, this activation step can specifically take place at M–O ion pairs by a heterolytic mechanism or at O–O pairs by a homolytic mechanism or at the terminal M═O site by an oxygen insertion mechanism. On the surface, it is found that the most feasible reaction pathway for the initial propane activation is H abstraction by the terminal Mo═O site and the C–H activation for methylene is 0.20 eV more favorable than that for the methyl C–H bond. The calculated activation enthalpy and entropy for the methylene C–H bond are 32.3 kcal mol^{-1} and −28.6 cal $(mol\ K^{-1})^{-1}$, respectively.

Also, for MoO_x catalysts, similar active centers are present on supported MoO_x, MoO_3, and $ZrMo_2O_8$.[428] Surface O and OH groups are the most abundant surface intermediates that can lead to a rate expression to accurately describe the measured kinetics of propane ODH.[427,428] On MoO_x and VO_x catalysts, similar kinetic rate expressions confirm that propane ODH occurs *via* similar pathways, using lattice oxygen atoms to abstract hydrogen atoms from propane in the RDS of irreversible C–H bond activation.[339] For the transition state for this elementary step, the electrons are transferred from lattice oxygens to metal centers as an i-propoxide and an OH group from propane.[438] Propane ODH activation energies (1.03–1.31 eV) are higher than those for propylene combustion (0.53–0.67 eV), where the measured difference in activation energy (0.50–0.63 eV) between the both is larger than the difference in the weakest C–H bond dissociation enthalpy between propane and propylene (0.42 eV).

The activation energies for propane primary dehydrogenation and propylene secondary combustion increase as the Lewis acidity of the cations increases ($V^{5+} < Mo^{6+} < W^{6+}$), while the corresponding reaction rates decrease. Therefore, metal oxides having high redox properties exhibit high catalytic activity, and less acidic metal oxides lead to higher propylene yields.[339] Chen *et al.* also reported that VO_x catalysts are much more active than MoO_x catalysts with similar H_2 reduction rates.[438]

Zhu *et al.*[358,391,405,439] systematically studied the catalytic performance of PDH on Cr_2O_3, ZnO, V_2O_3, and Ga_2O_3. There are oxygen vacancies that can exist on the ZnO surfaces, also

implying that the reaction path of the ODH mechanism could occur in the initial reaction stage.[405] Besides, oxygen vacancies may modify their electronic structure, thereby positively affecting the reactivity of α-Cr_2O_3, but negatively affecting ZnO mainly due to the weaker Lewis acid–base interaction on ZnO(10−10). Therefore, for the dehydrogenation reaction over some transition metal oxides without oxidants (such as O_2 and CO_2) introduced into the reaction gas mixture, active lattice oxygen can participate in the C–H bond activation, possibly following an ODH mechanism in the initial stage of the reaction before the oxide surfaces reach a steady state. However, if oxidants are introduced into the reaction gas, the dehydrogenation reaction could follow the ODH mechanism to remove the H atoms absorbed on the surface.[337,440,441] For example, Atanga *et al.*[442] proposed that CO_2 as a mild oxidant for the ODH of propane can reactivate deactivated redox catalysts caused by metal oxide reduction, and the introduction of CO_2 can also overcome the problems of over-oxidation and low propylene selectivity.

4.3 C–H activation on single atom–oxide hybrids

Single-atom catalysis is an area of intense current research.[443–445] On the one hand, single-atom catalysts (SACs) exhibit properties that are distinctly different from those of supported nanoclusters. On the other hand, single-atom catalysts have well-defined local structures, and therefore provide an opportunity for establishing the structure–reactivity relationship.[446–448] However, because of the low coordination environment, the surfaces of SACs have a high surface free energy, and single atoms tend to migrate and aggregate to form clusters. Recently, several research efforts have been devoted to synthesizing thermally stable SACs, such as the proposal of strong metal–support interactions (SMSI), which can play a role in keeping single atoms from sintering on the surface.[446,449] Lang *et al.* found that isolated Pt atoms or PtO_2 units can be trapped on an Fe_2O_3 support through SMSI during high-temperature calcination (800 °C, 5 h).[450]

Single metal atoms have been deposited onto transition metal, graphene, and metal oxides, among which singly dispersed metal atoms on metal oxides have received much attention in catalyzing PDH.[364,385,451–455] As has been observed by Xiong *et al.*,[451] isolated single atoms of Pt can be steadily trapped on CeO_2 catalysts, while the catalyst is not selective towards propylene. DFT calculations show that the strongly adsorbed propylene is expected to undergo further reactions, leading eventually to C–C bond cleavage. To prevent a further reaction, Sn is added to the Pt single-atom catalyst. They found that propylene showed much lower adsorption energy on small Pt–Sn clusters than that on single Pt atoms. Consequently, a higher selectivity is obtained on Pt–Sn–CeO_2. Sun *et al.*[385] directly dispersed single Pt atoms on Cu NPs to form SAA catalysts, which exhibit high propylene selectivity (~90%) and great stability at 520 °C. In addition to the use of SAA catalysts, other SACs that provide excellent catalytic performance for PDH are still under theoretical research.

Some supports have been considered to anchor single metal atoms by theoretical calculations.[358,391,405,439] For instance, Pt_1–Cr_2O_3(0001) and Pt_1–ZnO(10−10) oxides were constructed by Chang *et al.*,[405] and show higher activity than their pristine surfaces by lowering the activation energy for the RDS and promoting H_2 desorption, and on these two types of oxide surfaces single Pt atoms act as promoters (see Fig. 38). These findings are in line with experimental and DFT studies by Liu *et al.* and Sattler *et al.*,[333,456] which clearly showed that the addition of a trace amount of Pt could accelerate H_2 desorption over ZnO/Al_2O_3 catalysts and affect the distribution of Ga^{3+}, thereby leading to a higher activity than the pristine surfaces.[2,456] This may be attributed to the interactions

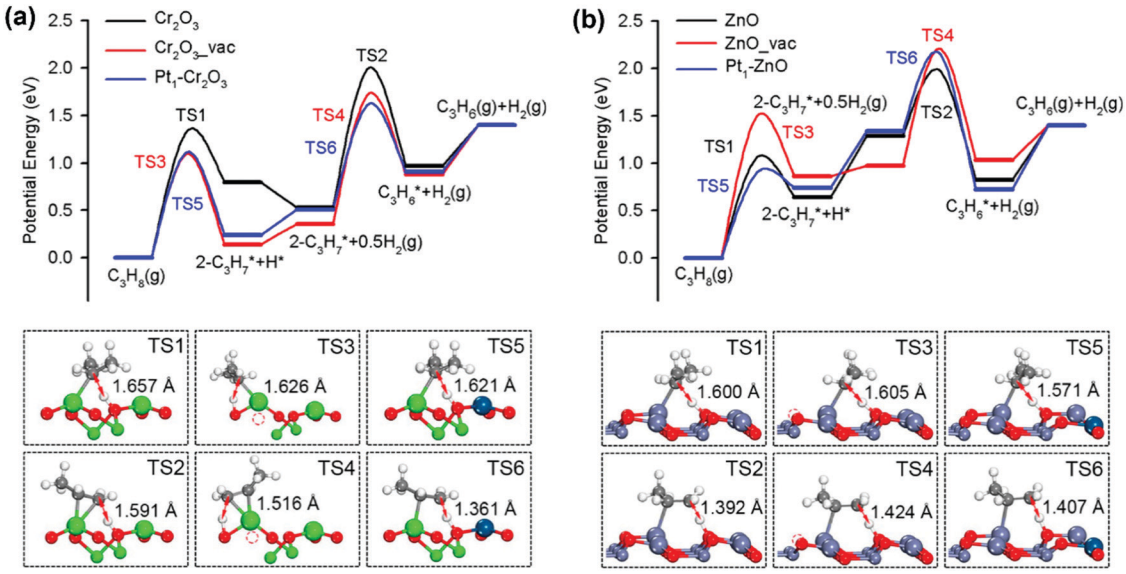

Fig. 38 Energy profiles for PDH on pristine, oxygen-deficient, and Pt-doped (a) Cr_2O_3 and (b) ZnO surfaces. All the potential energies are referenced to gas-phase propane.[405] Reproduced from ref. 405 with permission from the American Chemical Society, copyright 2019.

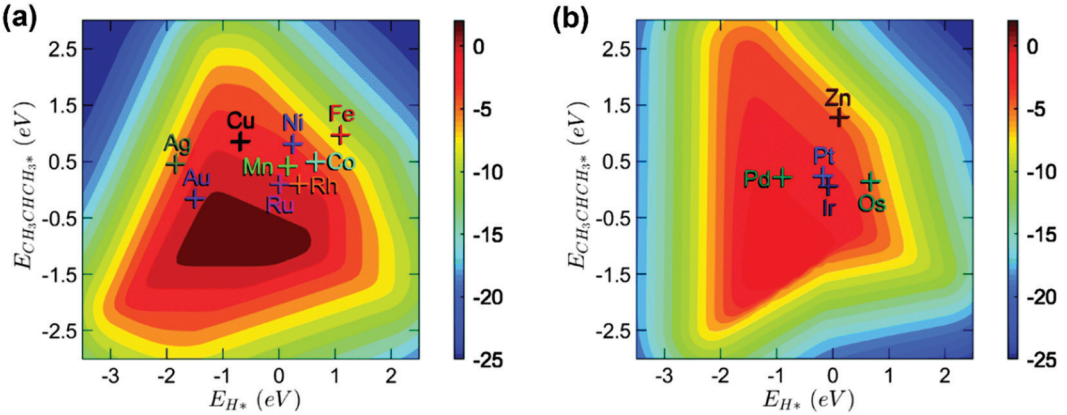

Fig. 39 TOFs for propane dehydrogenation to propylene as a function of the formation energies of adsorbed H at the O site and adsorbed 2-propyl at the M site on the (a) first and (b) second groups of doped oxide surfaces.[358] Reproduced from ref. 358 with permission from the Royal Society of Chemistry, copyright 2020.

between Pt and ZnO (or TiO_2). On the Pt_1–Ga_2O_3(100) surface, a Pt-doped Ga_2O_3 catalyst shows a bifunctional character in PDH where the Pt–O site brings about dehydrogenation, while the Ga–O site is active for desorbing H_2.[439]

The kinetics of the PDH reaction over M_1–V_2O_3 (M = Mn–Cu, Ru–Ag, and Os–Au) were studied by Zhang *et al.*[391] In their model, surface V and O atoms are replaced with single atoms, including M_1–(V_{vac})–V_2O_3(0001) (M = Mn, Fe, Co, Ni, and Cu) and M_1–(O_{vac})–V_2O_3(0001) (M = Pd, Pt, and Au). Moreover, it shows that the V–O(o) site is the dominant active site over V_2O_3(0001). These findings agree well with the experimental studies by Liu *et al.* who found that V^{3+} was more active for PDH over VO_x/Al_2O_3, which, to some extent, explains why a VO_x catalyst without H_2 reduction shows higher initial activity.[394] Besides, on M_1–(V_{vac})–V_2O_3(0001), the active site for PDH is V–O(o) and M acts as the promoter, while on M_1–(O_{vac})–V_2O_3(0001) the M and V ion pairs act as the active site. Apart from the work by Zhang *et al.*, Ma *et al.* systemically examined the structural stability, catalytic activity and selectivity of 13 M_1–ZnO (M = Mn, Fe, Co, Ni, Cu, Ru, Rh, Pd, Ag, Os, Ir, Pt, and Au).[358] By applying linear scaling relations of chemisorption energy and transition-state energy, it is found that the formation energies of H and 2-propyl can be used to measure the binding strengths of all the reaction intermediates and activated complexes and can therefore be used as descriptors to describe the kinetics of PDH over M_1–ZnO. As indicated in Fig. 39, theoretical calculations predict that most of the single-atom-doped ZnO catalysts except for Fe- and Os-doped ZnO exhibit higher activity than pristine ZnO. Such a study can not only offer new opportunities to develop a more cost-effective heterogeneous catalyst but also help guide future experiments.

5. Conclusions and perspectives

The paper reviews the computational catalysis of the C–H bond activation of light alkanes such as methane, ethane, and propane towards synthesis gas and light olefins, as the important building blocks of the chemical industry. Quantum chemical calculations have grown into a technique of extraordinary power that pervades all current discussions of heterogeneous catalysis. In particular, computational approaches that use results from DFT calculations combined with descriptor-based scaling relationships as inputs to microkinetic analysis or kinetic Monte Carlo simulations not only play a significant role in developing a step-by-step, molecular-level view of the pathway leading to products but also provide an effective way to rationally screen potential catalyst candidates for a given catalytic reaction. A highly integrated approach using DFT, linear scaling relations, and microkinetic modeling successfully accounts for the way catalyst compositions like various metals, alloys, single atoms, metal–oxide interfaces, and locally coordinated oxygen in oxides modify the electronic properties of the active sites and their relations to the catalytic performance of alkane conversion. DFT-based microkinetic analysis extends the computational catalysis from model surfaces to industrially relevant catalysts. In this review, we attempted to illustrate the recent substantial progress made by using such theoretical methods in understanding the effects of geometrical and electronic structures on the activation of C–H bonds of light alkanes and in the discovery of new and more effective catalysts for light alkane conversion on metal and metal oxides. Special efforts have been devoted to recognizing the patterns of catalytic activity and selectivity for a class of substances applied in commercially important reactions.

Despite the fact that many different reactions and different types of catalysts have been applied to convert light alkanes to valuable products, it is common that the light alkane transformation initiates from C–H cleavage. The C–H bond activation of methane, ethane, and propane on metal and metal oxides was summarized and compared. A universal scaling relationship of C–H bond activation across C1–C3 alkanes and various catalysts was discussed.

Some mechanistic insights into methane conversion to synthesis gas are common for steam reforming, dry reforming and partial oxidation, involving C–H bond cleavage to form CH_x

followed by subsequent oxidation of CH* or C* by O* or OH*. The preferred reaction pathways and rate-determining step depend on the catalysts and operating conditions. DFT calculations and microkinetic modeling provide a guideline to manipulate the catalyst surface to reduce the carbon formation by lowering the surface carbon coverage. The lowered surface carbon coverage benefits from the enhanced CH* oxidation and the reduced CH* formation and its decomposition to surface carbon.

The critical challenges in ethane and propane dehydrogenation and oxidative dehydrogenation are the selectivities to olefins and coke formation. The DFT calculations and kinetic analysis unravel useful fundamental insights into these key challenges at the molecular level, where the difference in the desorption energy of olefins and the activation energy of deep dehydrogenation of surface intermediates is used as the descriptor. Computational catalysis suggested Pt-based alloys as the best candidates for industrial catalysts by lowering the olefin desorption energy.

Oxidative dehydrogenation on oxides is an attractive alternative for light alkane dehydrogenation to olefins due to the breaking of the thermodynamic limitation and *in situ* supply of heat for highly endothermic dehydrogenation reactions. However, the critical challenge in olefin selectivity still remains due to the high reactivity of olefins. DFT calculations elucidated the active sites and surface reactions responsible for the formation of olefins, CO_x, and other byproducts. The lattice oxygen is the main active site. It significantly adds complexity in DFT modeling, where the activity of oxygen depends on the local structure and coordination as well as oxygen vacancy. However, it also provides huge opportunities to tune the oxygen activity to reduce the C–C bond cleavage and oxidation to CO_x. Oxides are a large family and present numerous oxide structures. The experimental and theoretical studies revealed the catalyst's activity dependence on the oxide identity, doping, cluster size, and supports. The formation energy of oxygen vacancy or hydrogen affinity was identified as the descriptor to describe the oxygen activity. However, a thorough screening of a huge number of oxide structures to find appropriate catalyst candidates for a given reaction remains a formidable challenge. Most of the studies have been performed only addressing the C–H bond activation. DFT calculations of elementary steps involved in the whole catalytic cycle, including by-product formation, are essential to address the selectivity. In addition, the active sites are highly dynamic on oxides due to their redox nature, with generation and filling of the oxygen vacancy. The oxygen vacancy in the steady-state can be changed with reaction conditions. Full modeling of reactions accounting for active site dynamics is also extremely challenging. Better scaling relationships for adsorption energy and activation energy on oxides need to be explored based on a big dataset. Machine learning and artificial intelligence could be explored to significantly accelerate catalyst development.

There is generally a strongly constrained relation between the C–H bond activation of light paraffins, olefin desorption, and deep C–H bond activation, which presents a challenge in catalyst design to maintain high activity, selectivity, and stability with a high coking resistance, simultaneously. The alloy of Pt with a second metal and a core–shell structure is an effective way to lower the ethylene and propylene desorption energy and increase the olefin selectivity and lower the coking potential, but at the expense of lower activity. The single metal or metal clusters on oxides could be explored to break down the constrained relation to enhance the catalytic performance. However, the active sites at the metal–oxide interface largely increase the complexity of the modeling. There are much more possible sites for adsorption and elementary reactions compared to the metal and oxide alone.

There remain several challenges in theoretical catalysis, which makes it difficult to discuss the chemistry of light alkane conversion in a more quantitative way. First, DFT has its complexity and a lot of physics hidden inside the approximate exchange–correlation functional. This term works surprisingly well given its simplicity and holds the key to the success of the theory. However, it is still challenging to quantitatively reproduce the reaction rates obtained from experiments, since the values of the calculated reaction heat and activation energy obtained by DFT calculations have an uncertainty of 0.1–0.2 eV.[457,458]

Second, the structure of active sites on catalysts is generally represented by simple low-index surfaces in computational studies. A gap still exists between realistic catalysts under reaction conditions and model surfaces. *In situ* characterization of working catalysts can provide more detailed structural information to help build more reliable structures close to industrial catalysts. Even though computational modeling of the surface structure of industrial catalysts needs to be carried out with caution, there is no doubt that DFT calculations are able to suggest mechanisms and structure–activity–selectivity relations, and rationalize a considerable amount of experimental observations, which are often difficult to understand. Finally, the microkinetic analysis of reactions is necessary to present the experimental conditions appropriately to understand important industrial reactions. The DFT calculations and microkinetic modeling need to be even more tightly associated with multiscale modeling at catalyst pellet and reactor levels, as well as the experimental study for searching for new catalysts and improving industrial catalysts.

Despite many challenges, with advances in density functional theory, scaling relationships, and descriptor-based microkinetic modeling, it is now possible to describe catalytic reactions at surfaces with the detail and accuracy required for computational results to compare favorably with experiments.[28] The computational approach has become an effective tool for the design of catalysts with high activity, selectivity, and stability. It is interesting to note that the advanced computational catalysis approach has predicted the most active pure metals for methane and propane activation, and some bimetallic alloys are screened based on the volcano curve obtained from pure metals for ethane activation. The highly integrated computational and experimental approach will be explored to accelerate the development of next-generation catalysts for alkane conversion.

Conflicts of interest

There are no conflicts to declare.

Acknowledgements

The supports from NTNU energy, the Centre for Industrial Catalysis Science and Innovation (iCSI), which receives financial support from the Norwegian Research Council, the Natural Science Foundation of China (No. 91645122 and 22073027), and the Natural Science Foundation of Shanghai (No. 20ZR1415800), as well as the computational time provided by the Notur project (nn4685k), are gratefully acknowledged.

Notes and references

1 X. Tang, X. Jia and Z. Huang, *Chem. Sci.*, 2018, **9**, 288–299.
2 J. J. H. B. Sattler, J. Ruiz-Martinez, E. Santillan-Jimenez and B. M. Weckhuysen, *Chem. Rev.*, 2014, **114**, 10613–10653.
3 R. Grabowski, *Catal. Rev.*, 2006, **48**, 199–268.
4 B. A. Arndtsen, R. G. Bergman, T. A. Mobley and T. H. Peterson, *Acc. Chem. Res.*, 1995, **28**, 154–162.
5 A. E. Shilov and G. B. Shul'pin, *Chem. Rev.*, 1997, **97**, 2879–2932.
6 S. S. Stahl, J. A. Labinger and J. E. Bercaw, *Angew. Chem., Int. Ed.*, 1998, **37**, 2180–2192.
7 B. G. Hashiguchi, S. M. Bischof, M. M. Konnick and R. A. Periana, *Acc. Chem. Res.*, 2012, **45**, 885–898.
8 J. A. Labinger and J. E. Bercaw, *J. Organomet. Chem.*, 2015, **793**, 47–53.
9 N. J. Gunsalus, A. Koppaka, S. H. Park, S. M. Bischof, B. G. Hashiguchi and R. A. Periana, *Chem. Rev.*, 2017, **117**, 8521–8573.
10 R. G. Bergman, *Nature*, 2007, **446**, 391–393.
11 H. Schwarz, *Angew. Chem., Int. Ed.*, 2011, **50**, 10096–10115.
12 P. Schwach, X. Pan and X. Bao, *Chem. Rev.*, 2017, **117**, 8497–8520.
13 A. Obradović, J. W. Thybaut and G. B. Marin, *Chem. Eng. Technol.*, 2016, **39**, 1996–2010.
14 D. Balcells, E. Clot and O. Eisenstein, *Chem. Rev.*, 2010, **110**, 749–823.
15 C. A. Carrero, R. Schloegl, I. E. Wachs and R. Schomaecker, *ACS Catal.*, 2014, **4**, 3357–3380.
16 J. F. Weaver, C. Hakanoglu, A. Antony and A. Asthagiri, *Chem. Soc. Rev.*, 2014, **43**, 7536–7547.
17 Z. Nawaz, *Rev. Chem. Eng.*, 2015, **31**, 413–436.
18 J. T. Grant, J. M. Venegas, W. P. McDermott and I. Hermans, *Chem. Rev.*, 2018, **118**, 2769–2815.
19 JCPDS—Joint Committee on Powder Diffraction Standards, International Center of Diffraction Data, CD-ROM, 1994, Pensilvânia, USA.
20 X. Sun, P. Han, B. Li, S. Mao, T. Liu, S. Ali, Z. Lian and D. Su, *Chem. Commun.*, 2018, **54**, 864–875.
21 G. Caeiro, R. H. Carvalho, X. Wang, M. A. N. D. A. Lemos, F. Lemos, M. Guisnet and F. Ramôa Ribeiro, *J. Mol. Catal., A*, 2006, **255**, 131–158.
22 J. M. Venegas, W. P. McDermott and I. Hermans, *Acc. Chem. Res.*, 2018, **51**, 2556–2564.
23 R. A. Periana, G. Bhalla, W. J. Tenn, K. J. H. Young, X. Y. Liu, O. Mironov, C. J. Jones and V. R. Ziatdinov, *J. Mol. Catal., A*, 2004, **220**, 7–25.
24 F. J. Keil, *Comput. Math. Appl.*, 2013, **65**, 1674–1697.
25 J. K. Norskov, *Nature*, 2001, **414**, 405–406.
26 J. K. Norskov, M. Scheffler and H. Toulhoat, *MRS Bull.*, 2006, **31**, 669–674.
27 J. K. Norskov, T. Bligaard, B. Hvolbaek, F. Abild-Pedersen, I. Chorkendorff and C. H. Christensen, *Chem. Soc. Rev.*, 2008, **37**, 2163–2171.
28 J. K. Norskov, T. Bligaard, J. Rossmeisl and C. H. Christensen, *Nat. Chem.*, 2009, **1**, 37–46.
29 Z. J. Zhao, C. C. Chiu and J. Gong, *Chem. Sci.*, 2015, **6**, 4403–4425.
30 C. A. Gaggioli, S. J. Stoneburner, C. J. Cramer and L. Gagliardi, *ACS Catal.*, 2019, **9**, 8481–8502.
31 A. H. Motagamwala, M. R. Ball and J. A. Dumesic, *Annu. Rev. Chem. Biomol. Eng.*, 2018, **9**, 413–450.
32 L. Grajciar, C. J. Heard, A. A. Bondarenko, M. V. Polynski, J. Meeprasert, E. A. Pidko and P. Nachtigall, *Chem. Soc. Rev.*, 2018, **47**, 8307–8348.
33 F. Abild-Pedersen, J. Greeley, F. Studt, J. Rossmeisl, T. R. Munter, P. G. Moses, E. Skulason, T. Bligaard and J. K. Norskov, *Phys. Rev. Lett.*, 2007, **99**, 016105.
34 A. Michaelides, Z.-P. Liu, C. Zhang, A. Alavi, D. A. King and P. Hu, *J. Am. Chem. Soc.*, 2003, **125**, 3704–3705.
35 J. Greeley, *Annu. Rev. Chem. Biomol. Eng.*, 2016, **7**, 605–635.
36 Y. Wang, L. Xiao, Y. Qi, M. Mahmoodinia, X. Feng, J. Yang, Y. A. Zhu and D. Chen, *Phys. Chem. Chem. Phys.*, 2019, **21**, 19269–19280.
37 M. Ravi, M. Ranocchiari and J. A. van Bokhoven, *Angew. Chem., Int. Ed.*, 2017, **56**, 16464–16483.
38 R. Horn and R. Schlögl, *Catal. Lett.*, 2014, **145**, 23–39.
39 B. Wang, S. Albarracín-Suazo, Y. Pagán-Torres and E. Nikolla, *Catal. Today*, 2017, **285**, 147–158.
40 D. Pakhare and J. Spivey, *Chem. Soc. Rev.*, 2014, **43**, 7813–7837.
41 F. J. Keil, *Nat. Chem.*, 2013, **5**, 91–92.
42 P. Tang, Q. Zhu, Z. Wu and D. Ma, *Energy Environ. Sci.*, 2014, **7**, 2580–2591.
43 G. Keller and M. Bhasin, *J. Catal.*, 1982, **73**, 9–19.
44 D. J. Driscoll, W. Martir, J. X. Wang and J. H. Lunsford, *J. Am. Chem. Soc.*, 1985, **107**, 58–63.
45 T. Ito, J. Wang, C. H. Lin and J. H. Lunsford, *J. Am. Chem. Soc.*, 1985, **107**, 5062–5068.
46 L. Wang, L. Tao, M. Xie, G. Xu, J. Huang and Y. Xu, *Catal. Lett.*, 1993, **21**, 35–41.
47 X. Guo, G. Fang, G. Li, H. Ma, H. Fan, L. Yu, C. Ma, X. Wu, D. Deng and M. Wei, *Science*, 2014, **344**, 616–619.
48 A. P. E. York, T. Xiao and M. L. H. Green, *Top. Catal.*, 2003, **22**, 345–358.
49 A. W. Budiman, S.-H. Song, T.-S. Chang, C.-H. Shin and M.-J. Choi, *Catal. Surv. Asia*, 2012, **16**, 183–197.
50 B. Abdullah, N. A. Abd Ghani and D.-V. N. Vo, *J. Cleaner Prod.*, 2017, **162**, 170–185.

51 W.-J. Jang, J.-O. Shim, H.-M. Kim, S.-Y. Yoo and H.-S. Roh, *Catal. Today*, 2019, **324**, 15–26.
52 P. V. Beurden, *On the Catalytic Aspects of Steam–Methane Reforming – A Literature Surve*, 2004.
53 J. P. Van Hook, *Catal. Rev.*, 2006, **21**, 1–51.
54 J. Liu, *Kinetics, catalysis and mechanism of methane steam reforming*, 2007.
55 D. Li, Y. Nakagawa and K. Tomishige, *Appl. Catal., A*, 2011, **408**, 1–24.
56 S. D. Angeli, G. Monteleone, A. Giaconia and A. A. Lemonidou, *Int. J. Hydrogen Energy*, 2014, **39**, 1979–1997.
57 T. L. LeValley, A. R. Richard and M. Fan, *Int. J. Hydrogen Energy*, 2014, **39**, 16983–17000.
58 E. Meloni, M. Martino and V. Palma, *Catalysts*, 2020, **10**, 352.
59 Y. Kathiraser, U. Oemar, E. T. Saw, Z. Li and S. Kawi, *Chem. Eng. J.*, 2015, **278**, 62–78.
60 M. Usman, W. M. A. Wan Daud and H. F. Abbas, *Renewable Sustainable Energy Rev.*, 2015, **45**, 710–744.
61 Z. Bian, S. Das, M. H. Wai, P. Hongmanorom and S. Kawi, *ChemPhysChem*, 2017, **18**, 3117–3134.
62 N. A. K. Aramouni, J. G. Touma, B. A. Tarboush, J. Zeaiter and M. N. Ahmad, *Renewable Sustainable Energy Rev.*, 2018, **82**, 2570–2585.
63 T. Yabe and Y. Sekine, *Fuel Process. Technol.*, 2018, **181**, 187–198.
64 Y. Wang, L. Yao, S. Wang, D. Mao and C. Hu, *Fuel Process. Technol.*, 2018, **169**, 199–206.
65 A. Abdulrasheed, A. A. Jalil, Y. Gambo, M. Ibrahim, H. U. Hambali and M. Y. Shahul Hamid, *Renewable Sustainable Energy Rev.*, 2019, **108**, 175–193.
66 R. Pitchai and K. Klier, *Catal. Rev.*, 1986, **28**, 13–88.
67 V. D. Sokolovskii, N. J. Coville, A. Parmaliana, I. Eskendirov and M. Makoa, *Catal. Today*, 1998, **42**, 191–195.
68 C. R. H. de Smet, *Partial oxidation of methane to synthesis gas: reaction kinetics and reactor modelling*, 2000, DOI: 10.6100/IR535178.
69 B. Christian Enger, R. Lødeng and A. Holmen, *Appl. Catal., A*, 2008, **346**, 1–27.
70 S. A. Al-Sayari, *Open Catal. J.*, 2013, **6**, 17–28.
71 R. Wang, J. Chen, W. Zhao, X. Zhang and J. Ran, *Theor. Chem. Acc.*, 2019, **138**, 38–51.
72 J. Védrine, *Catalysts*, 2016, **6**, 22.
73 J. C. Vedrine, *J. Energy Chem.*, 2016, **25**, 936–946.
74 J. C. Védrine and I. Fechete, *C. R. Chim.*, 2016, **19**, 1203–1225.
75 J. Wei and E. Iglesia, *J. Phys. Chem. B*, 2004, **108**, 4094–4103.
76 J. Wei and E. Iglesia, *J. Phys. Chem. B*, 2004, **108**, 7253–7262.
77 J. Wei, *J. Catal.*, 2004, **225**, 116–127.
78 J. Wei and E. Iglesia, *Angew. Chem., Int. Ed.*, 2004, **43**, 3685–3688.
79 J. Wei and E. Iglesia, *Phys. Chem. Chem. Phys.*, 2004, **6**, 3754–3759.
80 J. Wei and E. Iglesia, *J. Catal.*, 2004, **224**, 370–383.
81 S.-G. Wang, D.-B. Cao, Y.-W. Li, J. Wang and H. Jiao, *J. Phys. Chem. B*, 2006, **110**, 9976–9983.
82 S.-G. Wang, X.-Y. Liao, J. Hu, D.-B. Cao, Y.-W. Li, J. Wang and H. Jiao, *Surf. Sci.*, 2007, **601**, 1271–1284.
83 M. Maestri, D. Vlachos, A. Beretta, G. Groppi and E. Tronconi, *J. Catal.*, 2008, **259**, 211–222.
84 A. Trinchero, A. Hellman and H. Grönbeck, *Surf. Sci.*, 2013, **616**, 206–213.
85 L. Foppa, M.-C. Silaghi, K. Larmier and A. Comas-Vives, *J. Catal.*, 2016, **343**, 196–207.
86 M. Jørgensen and H. Grönbeck, *ACS Catal.*, 2016, **6**, 6730–6738.
87 Y. Wang, H. Wang, A. H. Dam, L. Xiao, Y. Qi, J. Niu, J. Yang, Y.-A. Zhu, A. Holmen and D. Chen, *Catal. Today*, 2020, **355**, 139–147.
88 R. Wang, J. Chen, W. Zhao, J. Wen, H. Li, L. Li and J. Ran, *Appl. Surf. Sci.*, 2019, **471**, 566–586.
89 Y. Wang, L. Xiao, Y. Qi, J. Yang, Y.-A. Zhu and D. Chen, *J. Phys. Chem. C*, 2020, **124**, 2501–2512.
90 Y. Meng, C. Ding, X. Gao, L. Ma, K. Zhang, J. Wang and Z. Li, *Appl. Surf. Sci.*, 2020, **513**, 145724.
91 D. Hibbitts and M. Neurock, *Surf. Sci.*, 2016, **650**, 210–220.
92 J. Niu, Y. Wang, Y. Qi, A. H. Dam, H. Wang, Y.-A. Zhu, A. Holmen, J. Ran and D. Chen, *Fuel*, 2020, **266**, 117143.
93 Y.-A. Zhu, D. Chen, X.-G. Zhou and W.-K. Yuan, *Catal. Today*, 2009, **148**, 260–267.
94 C. Fan, Y.-A. Zhu, M.-L. Yang, Z.-J. Sui, X.-G. Zhou and D. Chen, *Ind. Eng. Chem. Res.*, 2015, **54**, 5901–5913.
95 J. S. Yoo, J. Schumann, F. Studt, F. Abild-Pedersen and J. K. Nørskov, *J. Phys. Chem. C*, 2018, **122**, 16023–16032.
96 W. Tu, M. Ghoussoub, C. V. Singh and Y. C. Chin, *J. Am. Chem. Soc.*, 2017, **139**, 6928–6945.
97 Y. Chen and D. G. Vlachos, *Ind. Eng. Chem. Res.*, 2012, **51**, 12244–12252.
98 R. L. Arevalo, S. M. Aspera, M. C. S. Escano, H. Nakanishi and H. Kasai, *Sci. Rep.*, 2017, **7**, 13963–13970.
99 G. Jones, T. Bligaard, F. Abild-Pedersen and J. K. Norskov, *J. Phys.: Condens. Matter*, 2008, **20**, 064239.
100 S. Wang, V. Petzold, V. Tripkovic, J. Kleis, J. G. Howalt, E. Skulason, E. M. Fernandez, B. Hvolbaek, G. Jones, A. Toftelund, H. Falsig, M. Bjorketun, F. Studt, F. Abild-Pedersen, J. Rossmeisl, J. K. Norskov and T. Bligaard, *Phys. Chem. Chem. Phys.*, 2011, **13**, 20760–20765.
101 G. Kumar, S. L. J. Lau, M. D. Krcha and M. J. Janik, *ACS Catal.*, 2016, **6**, 1812–1821.
102 N. Shi, Y. Xie, Y. Yang, S. Xue, X. Li, K. Zhu, D. Huan, R. Peng, C. Xia and Y. Lu, *Mater. Renewable Sustainable Energy*, 2020, **9**, 1–18.
103 A. A. Latimer, H. Aljama, A. Kakekhani, J. S. Yoo, A. Kulkarni, C. Tsai, M. Garcia-Melchor, F. Abild-Pedersen and J. K. Norskov, *Phys. Chem. Chem. Phys.*, 2017, **19**, 3575–3581.
104 J. Xu, X.-M. Cao and P. Hu, *J. Phys. Chem. C*, 2019, **123**, 28802–28810.
105 R. K. Singha, Y. Tsuji, M. H. Mahyuddin and K. Yoshizawa, *J. Phys. Chem. C*, 2019, **123**, 9788–9798.
106 A. A. Latimer, A. R. Kulkarni, H. Aljama, J. H. Montoya, J. S. Yoo, C. Tsai, F. Abild-Pedersen, F. Studt and J. K. Norskov, *Nat. Mater.*, 2017, **16**, 225–229.

107 H. Aljama, J. K. Nørskov and F. Abild-Pedersen, *J. Phys. Chem. C*, 2017, **121**, 16440–16446.
108 H. Aljama, J. K. Nørskov and F. Abild-Pedersen, *J. Phys. Chem. C*, 2018, **122**, 22544–22548.
109 V. Fung, F. Polo-Garzon, Z. Wu and D.-E. Jiang, *Catal.: Sci. Technol.*, 2018, **8**, 702–709.
110 A. D. Mayernick and M. J. Janik, *J. Phys. Chem. C*, 2008, **112**, 14955–14964.
111 A. R. Derk, B. Li, S. Sharma, G. M. Moore, E. W. McFarland and H. Metiu, *Catal. Lett.*, 2013, **143**, 406–410.
112 B. Li and H. Metiu, *J. Phys. Chem. C*, 2011, **115**, 18239–18246.
113 W. Tang, Z. Hu, M. Wang, G. D. Stucky, H. Metiu and E. W. McFarland, *J. Catal.*, 2010, **273**, 125–137.
114 I. M. Ciobîcă, F. Frechard, R. A. V. Santen, A. W. Kleyn and J. Hafner, *J. Phys. Chem. B*, 2000, **104**, 3364–3369.
115 I. M. Ciobica and R. A. V. Santen, *J. Phys. Chem. B*, 2002, **106**, 6200–6205.
116 L. Xiao and L. Wang, *J. Phys. Chem. B*, 2007, **111**, 1657–1663.
117 M. F. Fellah and I. Onal, *Catal. Today*, 2011, **171**, 52–59.
118 J. Li, E. Croiset and L. Ricardez-Sandoval, *J. Mol. Catal., A*, 2012, **365**, 103–114.
119 J. Niu, J. Ran, X. Du, W. Qi, P. Zhang and L. Yang, *Mol. Catal.*, 2017, **434**, 206–218.
120 Z. Jiang, Z. Wu, T. Fang and C. Yi, *Chem. Phys. Lett.*, 2019, **715**, 323–329.
121 R. L. Arevalo, S. M. Aspera, M. C. Sison Escano, H. Nakanishi and H. Kasai, *ACS Omega*, 2017, **2**, 1295–1301.
122 J. R. Rostrup-Nielsen, *J. Catal.*, 1973, **31**, 173–199.
123 J. R. Rostrupnielsen and J. H. B. Hansen, *J. Catal.*, 1993, **144**, 38–49.
124 D. Qin and J. Lapszewicz, *Catal. Today*, 1994, **21**, 551–560.
125 L. M. Aparicio, *J. Catal.*, 1997, **165**, 262–274.
126 H. S. Bengaard, J. K. Nørskov, J. Sehested, B. S. Clausen, L. P. Nielsen, A. M. Molenbroek and J. R. Rostrup-Nielsen, *J. Catal.*, 2002, **209**, 365–384.
127 G. Jones, J. Jakobsen, S. Shim, J. Kleis, M. Andersson, J. Rossmeisl, F. Abildpedersen, T. Bligaard, S. Helveg and B. Hinnemann, *J. Catal.*, 2008, **259**, 147–160.
128 D. Mei, V.-A. Glezakou, V. Lebarbier, L. Kovarik, H. Wan, K. O. Albrecht, M. Gerber, R. Rousseau and R. A. Dagle, *J. Catal.*, 2014, **316**, 11–23.
129 L. Maier, B. Schädel, K. H. Delgado, S. Tischer and O. Deutschmann, *Top. Catal.*, 2011, **54**, 845.
130 D. W. Blaylock, T. Ogura, W. H. Green and G. J. O. Beran, *J. Phys. Chem. C*, 2009, **113**, 4898–4908.
131 P. W. van Grootel, E. J. Hensen and R. A. van Santen, *Langmuir*, 2010, **26**, 16339–16348.
132 D. W. Blaylock, Y.-A. Zhu and W. H. Green, *Top. Catal.*, 2011, **54**, 828–844.
133 Y. Xu, A. C. Lausche, S. Wang, T. S. Khan, F. Abild-Pedersen, F. Studt, J. K. Nørskov and T. Bligaard, *New J. Phys.*, 2013, **15**, 125021.
134 T. Zhu, P. W. van Grootel, I. A. W. Filot, S.-G. Sun, R. A. van Santen and E. J. M. Hensen, *J. Catal.*, 2013, **297**, 227–235.
135 Y. Yoon, H. Kim and J. Lee, *J. Power Sources*, 2017, **359**, 450–457.
136 E. Kikuchi, S. Tanaka, Y. Yamazaki and Y. Morita, *Bull. Jpn. Pet. Inst.*, 1974, **16**, 95–98.
137 J. K. Norskov and C. H. Christensen, *Science*, 2006, **312**, 1322–1323.
138 D. Chen, R. Lødeng, H. Svendsen and A. Holmen, *Ind. Eng. Chem. Res.*, 2011, **50**, 2600–2612.
139 C. Pistonesi, A. Juan, B. Irigoyen and N. Amadeo, *Appl. Surf. Sci.*, 2007, **253**, 4427–4437.
140 Z. Wang, X. M. Cao, J. Zhu and P. Hu, *J. Catal.*, 2014, **311**, 469–480.
141 M. Zhang, K. Yang, X. Zhang and Y. Yu, *Surf. Sci.*, 2014, **630**, 236–243.
142 O. R. Inderwildi, S. J. Jenkins and D. A. King, *Angew. Chem., Int. Ed.*, 2008, **47**, 5253–5255.
143 A. Donazzi, A. Beretta, G. Groppi and P. Forzatti, *J. Catal.*, 2008, **255**, 241–258.
144 A. Donazzi, A. Beretta, G. Groppi and P. Forzatti, *J. Catal.*, 2008, **255**, 259–268.
145 C. J. H. Jacobsen, S. Dahl, P. L. Hansen, E. Törnqvist, L. Jensen, H. Topsøe, D. V. Prip, P. B. Møenshaug and I. Chorkendorff, *J. Mol. Catal., A*, 2000, **163**, 19–26.
146 K. Honkala, A. Hellman, I. N. Remediakis, A. Logadottir, A. Carlsson, S. Dahl, C. H. Christensen and J. K. Nørskov, *Science*, 2005, **307**, 555–558.
147 E. Nikolla, J. Schwank and S. Linic, *J. Catal.*, 2009, **263**, 220–227.
148 M. Zeppieri, P. L. Villa, N. Verdone, M. Scarsella and P. De Filippis, *Appl. Catal., A*, 2010, **387**, 147–154.
149 D. A. J. M. Ligthart, R. A. van Santen and E. J. M. Hensen, *J. Catal.*, 2011, **280**, 206–220.
150 V. C. H. Kroll, H. M. Swaan and C. Mirodatos, *J. Catal.*, 1996, **161**, 409–422.
151 D. Chen, R. Lødeng, A. Anundskås, O. Olsvik and A. Holmen, *Chem. Eng. Sci.*, 2001, **56**, 1371–1379.
152 J.-W. Snoeck, G. F. Froment and M. Fowles, *J. Catal.*, 1997, **169**, 240–249.
153 F. Abild-Pedersen, J. K. Nørskov, J. R. Rostrup-Nielsen, J. Sehested and S. Helveg, *Phys. Rev. B: Condens. Matter Mater. Phys.*, 2006, **73**, 115419.
154 F. C. Schouten, O. L. J. Gijzeman and G. A. Bootsma, *Bull. Soc. Chim. Belg.*, 1979, **88**, 541–547.
155 F. C. Schouten, O. L. J. Gijzeman and G. A. Bootsma, *Surf. Sci.*, 1979, **87**, 1–12.
156 M. Eizenberg and J. M. Blakely, *J. Chem. Phys.*, 1979, **71**, 3467–3477.
157 I. Alstrup, *J. Catal.*, 1988, **109**, 241–251.
158 F. F. Tabrizi, S. A. H. S. Mousavi and H. Atashi, *Energy Convers. Manage.*, 2015, **103**, 1065–1077.
159 D. Pashchenko, *Int. J. Energy Res.*, 2020, **44**, 438–447.
160 F. Besenbacher, I. Chorkendorff, B. Clausen, B. Hammer, A. Molenbroek, J. K. Nørskov and I. Stensgaard, *Science*, 1998, **279**, 1913–1915.
161 J. H. Jeong, J. W. Lee, D. J. Seo, Y. Seo, W. L. Yoon, D. K. Lee and D. H. Kim, *Appl. Catal., A*, 2006, **302**, 151–156.

162 X. You, X. Wang, Y. Ma, J. Liu, W. Liu, X. Xu, H. Peng, C. Li, W. Zhou, P. Yuan and X. Chen, *ChemCatChem*, 2014, **6**, 3377–3386.
163 D. Li, Y. Zhan, K. Nishida, Y. Oumi, T. Sano, T. Shishido and K. Takehira, *Appl. Catal., A*, 2009, **363**, 169–179.
164 Y. Zhan, D. Li, K. Nishida, T. Shishido, Y. Oumi, T. Sano and K. Takehira, *Appl. Clay Sci.*, 2009, **45**, 147–154.
165 N. V. Parizotto, K. O. Rocha, S. Damyanova, F. B. Passos, D. Zanchet, C. M. P. Marques and J. M. C. Bueno, *Appl. Catal., A*, 2007, **330**, 12–22.
166 E. Nikolla, A. Holewinski, J. Schwank and S. Linic, *J. Am. Chem. Soc.*, 2006, **128**, 11354–11355.
167 C. Fan, Y. A. Zhu, Y. Xu, Y. Zhou, X. G. Zhou and D. Chen, *J. Chem. Phys.*, 2012, **137**, 014703.
168 J. C. S. Wu and H.-C. Chou, *Chem. Eng. J.*, 2009, **148**, 539–545.
169 H. Arbag, S. Yasyerli, N. Yasyerli and G. Dogu, *Int. J. Hydrogen Energy*, 2010, **35**, 2296–2304.
170 Y. Xu, C. Fan, Y.-A. Zhu, P. Li, X.-G. Zhou, D. Chen and W.-K. Yuan, *Catal. Today*, 2012, **186**, 54–62.
171 H. Liu, B. Wang, M. Fan, N. Henson, Y. Zhang, B. F. Towler and H. Gordon Harris, *Fuel*, 2013, **113**, 712–718.
172 L. Chen, Z. Qi, S. Zhang, J. Su and G. A. Somorjai, *Catalysts*, 2020, **10**, 858.
173 V. C. H. Kroll, H. M. Swaan, S. Lacombe and C. Mirodatos, *J. Catal.*, 1996, **164**, 387–398.
174 Y. Schuurman, V. C. H. Kroll, P. Ferreira-Aparicio and C. Mirodatos, *Catal. Today*, 1997, **38**, 129–135.
175 J.-S. Chang, S.-E. Park, J. W. Yoo and J.-N. Park, *J. Catal.*, 2000, **195**, 1–11.
176 T. Osaki, T. Horiuchi, K. Suzuki and T. Mori, *J. Chem. Soc., Faraday Trans.*, 1996, **92**, 1627–1631.
177 J. Z. Luo, Z. L. Yu, C. F. Ng and C. T. Au, *J. Catal.*, 2000, **194**, 198–210.
178 T. Osaki and T. Mori, *J. Catal.*, 2001, **204**, 89–97.
179 M. C. J. Bradford and M. A. Vannice, *Appl. Catal., A*, 1996, **142**, 97–122.
180 A. Nandini, K. K. Pant and S. C. Dhingra, *Appl. Catal., A*, 2006, **308**, 119–127.
181 Y. Cui, H. Zhang, H. Xu and W. Li, *Appl. Catal., A*, 2007, **318**, 79–88.
182 J. Zhang, H. Wang and A. K. Dalai, *Ind. Eng. Chem. Res.*, 2009, **48**, 677–684.
183 S.-G. Wang, D.-B. Cao, Y.-W. Li, J. Wang and H. Jiao, *J. Phys. Chem. B*, 2005, **109**, 18956–18963.
184 D.-B. Cao, Y.-W. Li, J. Wang and H. Jiao, *Surf. Sci.*, 2009, **603**, 2991–2998.
185 J. Ko, B.-K. Kim and J. W. Han, *J. Phys. Chem. C*, 2016, **120**, 3438–3447.
186 P. Schlexer, H.-Y. T. Chen and G. Pacchioni, *Catal. Lett.*, 2017, **147**, 1871–1881.
187 S. Kattel, B. Yan, J. G. Chen and P. Liu, *J. Catal.*, 2016, **343**, 115–126.
188 X. Yang, S. Kattel, S. D. Senanayake, J. A. Boscoboinik, X. Nie, J. Graciani, J. A. Rodriguez, P. Liu, D. J. Stacchiola and J. G. Chen, *J. Am. Chem. Soc.*, 2015, **137**, 10104–10107.
189 J. Niu, S. E. Liland, J. Yang, K. R. Rout, J. Ran and D. Chen, *Chem. Eng. J.*, 2019, **377**, 119763.
190 J. Niu, X. Du, J. Ran and R. Wang, *Appl. Surf. Sci.*, 2016, **376**, 79–90.
191 P. Ferreira-Aparicio, A. Guerrero-Ruiz and I. Rodríguez-Ramos, *Appl. Catal., A*, 1998, **170**, 177–187.
192 J. H. Edwards and A. M. Maitra, *Fuel Process. Technol.*, 1995, **42**, 269–289.
193 F. Solymosi, G. Kutsán and A. Erdöhelyi, *Catal. Lett.*, 1991, **11**, 149–156.
194 P. G. Lustemberg, P. J. Ramírez, Z. Liu, R. A. Gutiérrez, D. G. Grinter, J. Carrasco, S. D. Senanayake, J. A. Rodriguez and M. V. Ganduglia-Pirovano, *ACS Catal.*, 2016, **6**, 8184–8191.
195 C. Vogt, J. Kranenborg, M. Monai and B. M. Weckhuysen, *ACS Catal.*, 2019, **10**, 1428–1438.
196 M. Akri, S. Zhao, X. Li, K. Zang, A. F. Lee, M. A. Isaacs, W. Xi, Y. Gangarajula, J. Luo and Y. Ren, *Nat. Commun.*, 2019, **10**, 1–10.
197 Z. Liu, D. C. Grinter, P. G. Lustemberg, T. D. Nguyen-Phan, Y. Zhou, S. Luo, I. Waluyo, E. J. Crumlin, D. J. Stacchiola, J. Zhou, J. Carrasco, H. F. Busnengo, M. V. Ganduglia-Pirovano, S. D. Senanayake and J. A. Rodriguez, *Angew. Chem., Int. Ed.*, 2016, **55**, 7455–7459.
198 Z. Liu, P. Lustemberg, R. A. Gutierrez, J. J. Carey, R. M. Palomino, M. Vorokhta, D. C. Grinter, P. J. Ramirez, V. Matolin, M. Nolan, M. V. Ganduglia-Pirovano, S. D. Senanayake and J. A. Rodriguez, *Angew. Chem., Int. Ed.*, 2017, **56**, 13041–13046.
199 Z. Zuo, S. Liu, Z. Wang, C. Liu, W. Huang, J. Huang and P. Liu, *ACS Catal.*, 2018, **8**, 9821–9835.
200 L. Foppa, T. Margossian, S. M. Kim, C. Muller, C. Coperet, K. Larmier and A. Comas-Vives, *J. Am. Chem. Soc.*, 2017, **139**, 17128–17139.
201 K. Li, X. Chang, C. Pei, X. Li, S. Chen, X. Zhang, S. Assabumrungrat, Z.-J. Zhao, L. Zeng and J. Gong, *Appl. Catal., B*, 2019, **259**, 118092.
202 K. Li, F. He, H. Yu, Y. Wang and Z. Wu, *J. Catal.*, 2018, **364**, 248–261.
203 M. A. L. Ferreira, N. N. Nichio and O. A. Ferretti, *J. Mol. Catal., A*, 2003, **202**, 197–213.
204 U. Guharoy, E. Le Saché, Q. Cai, T. R. Reina and S. Gu, *J. CO_2* Util., 2018, **27**, 1–10.
205 L.-l. Xu, H. Wen, X. Jin, Q.-m. Bing and J.-y. Liu, *Appl. Surf. Sci.*, 2018, **443**, 515–524.
206 S. M. Kim, P. M. Abdala, T. Margossian, D. Hosseini, L. Foppa, A. Armutlulu, W. van Beek, A. Comas-Vives, C. Coperet and C. Muller, *J. Am. Chem. Soc.*, 2017, **139**, 1937–1949.
207 A. Omran, S. H. Yoon, M. Khan, M. Ghouri, A. Chatla and N. Elbashir, *Catalysts*, 2020, **10**, 1043.
208 S.-H. Kye, H. S. Park, R. Zhang, H. J. Yang, K. H. Lee, H. Suh, J.-G. Kim, M. G. Kim, G. S. Hwang and N. H. Hur, *J. Chem. Phys.*, 2020, **152**, 054715.
209 R. Sharma, H. Poelman, G. B. Marin and V. V. Galvita, *Catalysts*, 2020, **10**, 194.
210 V. A. Kondratenko, C. Berger-Karin and E. V. Kondratenko, *ACS Catal.*, 2014, **4**, 3136–3144.

211 P. Aghalayam, Y. K. Park and D. G. Vlachos, *Catalysis*, 2000, 98–137, DOI: 10.1039/9781847553270-00098.
212 J. Zhu, D. Zhang and K. D. King, *Fuel*, 2001, **80**, 899–905.
213 M. Prettre, C. Eichner and M. Perrin, *Trans. Faraday Soc.*, 1946, **42**, 335–339.
214 A. B. Mhadeshwar and D. G. Vlachos, *Ind. Eng. Chem. Res.*, 2007, **46**, 5310–5324.
215 D. A. Hickman and L. D. Schmidt, *AIChE J.*, 1993, **39**, 1164–1177.
216 D. A. Hickman and L. D. Schmidt, *Science*, 1993, **259**, 343–346.
217 Y. Boucouvalas, Z. Zhang and X. E. Verykios, *Catal. Lett.*, 1994, **27**, 131–142.
218 J. T. Richardson and S. A. Paripatyadar, *Appl. Catal.*, 1990, **61**, 293–309.
219 A. Erdohelyi, J. Cserenyi and F. Solymosi, *J. Catal.*, 1993, **141**, 287–299.
220 E. P. J. Mallens, J. H. B. J. Hoebink and G. B. Marin, *Catal. Lett.*, 1995, **33**, 291–304.
221 P. Mars and D. W. van Krevelen, *Chem. Eng. Sci.*, 1954, **3**, 41–59.
222 A. B. Mhadeshwar and D. G. Vlachos, *J. Phys. Chem. B*, 2005, **109**, 16819–16835.
223 M. Maestri, D. G. Vlachos, A. Beretta, P. Forzatti, G. Groppi and E. Tronconi, *Top. Catal.*, 2009, **52**, 1983–1988.
224 M. Maestri, D. G. Vlachos, A. Beretta, G. Groppi and E. Tronconi, *AIChE J.*, 2009, **55**, 993–1008.
225 M. Maestri, A. Beretta, T. Faravelli, G. Groppi, E. Tronconi and D. G. Vlachos, *Chem. Eng. Sci.*, 2008, **63**, 2657–2669.
226 A. Donazzi, M. Maestri, B. C. Michael, A. Beretta, P. Forzatti, G. Groppi, E. Tronconi, L. D. Schmidt and D. G. Vlachos, *J. Catal.*, 2010, **275**, 270–279.
227 Y.-H. Chin, C. Buda, M. Neurock and E. Iglesia, *J. Catal.*, 2011, **283**, 10–24.
228 C.-T. Au, M.-S. Liao and C.-F. Ng, *J. Phys. Chem. A*, 1998, **102**, 3959–3969.
229 J. B. Claridge, M. L. H. Green, S. C. Tsang, A. P. E. York, A. T. Ashcroft and P. D. Battle, *Catal. Lett.*, 1993, **22**, 299–305.
230 J. He, Z. Yang, C. Ding, L. Zhang, Y. Yan and X. Du, *Fuel*, 2018, **226**, 400–409.
231 Y. Meng, C. Ding, Y. Xue, X. Gao, K. Zhang, J. Wang and Z. Li, *New J. Chem.*, 2020, **44**, 3922–3929.
232 D. Guo and G.-C. Wang, *J. Phys. Chem. C*, 2017, **121**, 26308–26320.
233 D. Guo, J.-H. Wen and G.-C. Wang, *Catal. Today*, 2020, **355**, 422–434.
234 G. J. Hutchings, M. S. Scurrell and J. R. Woodhouse, *Chem. Soc. Rev.*, 1989, **18**, 251–283.
235 J. G. McCarty and H. Wiseb, *Catal. Today*, 1990, **8**, 231–248.
236 T. Seiyama, *Catal. Rev.*, 1992, **34**, 281–300.
237 Q. Zhu, X. Zhao and Y. Deng, *J. Nat. Gas Chem.*, 2004, **13**, 191–203.
238 E. W. McFarland and H. Metiu, *Chem. Rev.*, 2013, **113**, 4391–4427.
239 T. M. Gür, *Prog. Energy Combust. Sci.*, 2016, **54**, 1–64.
240 J. L. Callahan and R. K. Grasselli, *AIChE J.*, 1963, **9**, 755–760.
241 O. Kiyoshi, U. Tetsuya and Y. Ichiro, *Chem. Lett.*, 1993, 1517–1520.
242 A. D. Mayernick and M. J. Janik, *J. Catal.*, 2011, **278**, 16–25.
243 Z.-P. Liu and P. Hu, *J. Am. Chem. Soc.*, 2003, **125**, 1958–1967.
244 Y. Jin, C. Sun and S. Su, *Phys. Chem. Chem. Phys.*, 2015, **17**, 16277–16284.
245 Y. Tsuji and K. Yoshizawa, *J. Phys. Chem. C*, 2018, **122**, 15359–15381.
246 C.-H. Yeh, T. M. L. Pham, S. Nachimuthu and J.-C. Jiang, *ACS Catal.*, 2019, **9**, 8230–8242.
247 B. Irigoyen, N. Castellani and A. Juan, *J. Mol. Catal., A*, 1998, **129**, 297–310.
248 S. Ozturk, I. Onal and S. Senkan, *Ind. Eng. Chem. Res.*, 2000, **39**, 250–258.
249 M. A. Peña and J. L. G. Fierro, *Chem. Rev.*, 2001, **101**, 1981–2018.
250 S. Royer, D. Duprez, F. Can, X. Courtois, C. Batiot-Dupeyrat, S. Laassiri and H. Alamdari, *Chem. Rev.*, 2014, **114**, 10292–10368.
251 K. Kousi, D. Neagu, L. Bekris, E. I. Papaioannou and I. S. Metcalfe, *Angew. Chem., Int. Ed.*, 2020, **59**, 2510–2519.
252 X. Zhang, C. Pei, X. Chang, S. Chen, R. Liu, Z. J. Zhao, R. Mu and J. Gong, *J. Am. Chem. Soc.*, 2020, **142**, 11540–11549.
253 H. Chang, E. Bjorgum, O. Mihai, J. Yang, H. L. Lein, T. Grande, S. Raaen, Y. A. Zhu, A. Holmen and D. Chen, *ACS Catal.*, 2020, **10**, 3707–3719.
254 D. D. Miller, J. Riley and R. Siriwardane, *Energy Fuels*, 2019, **34**, 2193–2204.
255 F. F. Tao, J. J. Shan, L. Nguyen, Z. Wang, S. Zhang, L. Zhang, Z. Wu, W. Huang, S. Zeng and P. Hu, *Nat. Commun.*, 2015, **6**, 7798–7807.
256 Y. Chen, B. deGlee, Y. Tang, Z. Wang, B. Zhao, Y. Wei, L. Zhang, S. Yoo, K. Pei, J. H. Kim, Y. Ding, P. Hu, F. F. Tao and M. Liu, *Nat. Energy*, 2018, **3**, 1042–1050.
257 F. Polo-Garzon, M. He and D. A. Bruce, *J. Catal.*, 2016, **333**, 59–70.
258 S. Jiang, Y. Lu, S. Wang, Y. Zhao and X. Ma, *Appl. Surf. Sci.*, 2017, **416**, 59–68.
259 P. Wu, Y. Tao, H. Ling, Z. Chen, J. Ding, X. Zeng, X. Liao, C. Stampfl and J. Huang, *ACS Catal.*, 2019, **9**, 10060–10069.
260 V. A. Ranea, I. Carmichael and W. F. Schneider, *J. Phys. Chem. C*, 2009, **113**, 2149–2158.
261 R. S. Alvim, I. Borges, D. G. Costa and A. A. Leitão, *J. Phys. Chem. C*, 2011, **116**, 738–744.
262 J. H. Bitter, K. Seshan and J. A. Lercher, *J. Catal.*, 1998, **176**, 93–101.
263 J. Guo, H. Lou, L. Mo and X. Zheng, *J. Mol. Catal. A: Chem.*, 2010, **316**, 1–7.
264 H. H. Kung, *Advances in Catalysis*, Elsevier, 1994, vol. 40, pp. 1–38.
265 C. A. Gärtner, A. C. van Veen and J. A. Lercher, *ChemCatChem*, 2013, **5**, 3196–3217.

266 F. Cavani and F. Trifiro, *Catal. Today*, 1995, **24**, 307–313.
267 F. Cavani and F. Trifiro, *Catal. Today*, 1999, **51**, 561–580.
268 S. Wang and Z. Zhu, *Energy Fuels*, 2004, **18**, 1126–1139.
269 A. Alamdari, R. Karimzadeh and S. Abbasizadeh, *Rev. Chem. Eng.*, 2019, **1**, DOI: 10.1515/revce-2017-0109.
270 D. Mukherjee, S.-E. Park and B. M. Reddy, *J. CO_2* Util., 2016, **16**, 301–312.
271 L. Shi, Y. Wang, B. Yan, W. Song, D. Shao and A.-H. Lu, *Chem. Commun.*, 2018, **54**, 10936–10946.
272 E. Gomez, B. Yan, S. Kattel and J. G. Chen, *Nat. Rev. Chem.*, 2019, 1–12.
273 A. M. Gaffney, Q. An, W. A. Goddard, W. Diao and M. V. Glazoff, *Top. Catal.*, 2020, 1–15.
274 I. Horiuti and M. Polanyi, *Trans. Faraday Soc.*, 1934, **30**, 1164–1172.
275 R. D. Cortright, P. E. Levin and J. A. Dumesic, *Ind. Eng. Chem. Res.*, 1998, **37**, 1717–1723.
276 Q. Li, Z. Sui, X. Zhou and D. Chen, *Appl. Catal., A*, 2011, **398**, 18–26.
277 A. W. Hauser, J. Gomes, M. Bajdich, M. Head-Gordon and A. T. Bell, *Phys. Chem. Chem. Phys.*, 2013, **15**, 20727–20734.
278 E. Jimenez-Izal, J.-Y. Liu and A. N. Alexandrova, *J. Catal.*, 2019, **374**, 93–100.
279 Y. Chen and D. G. Vlachos, *J. Phys. Chem. C*, 2010, **114**, 4973–4982.
280 G. Peng, D. Gerceker, M. Kumbhalkar, J. A. Dumesic and M. Mavrikakis, *Catal.: Sci. Technol.*, 2018, **8**, 2159–2174.
281 X. Ding, H. Zhu, H. Ren, D. Liu, Z. Yu, N. Shi and W. Guo, *Phys. Chem. Chem. Phys.*, 2020, **22**, 21835–21843.
282 A. Hook, J. D. Massa and F. E. Celik, *J. Phys. Chem. C*, 2016, **120**, 27307–27318.
283 A. Hook and F. E. Celik, *J. Phys. Chem. C*, 2017, **121**, 17882–17892.
284 J. Nam and F. E. Celik, *Top. Catal.*, 2020, **63**, 700–713.
285 A. Anghel, D. Wales, S. Jenkins and D. King, *Chem. Phys. Lett.*, 2005, **413**, 289–293.
286 A. Anghel, D. Wales, S. Jenkins and D. King, *J. Chem. Phys.*, 2007, **126**, 044710.
287 M. H. Hansen, J. K. Nørskov and T. Bligaard, *J. Catal.*, 2019, **374**, 161–170.
288 J. Wu, S. M. Sharada, C. Ho, A. W. Hauser, M. Head-Gordon and A. T. Bell, *Appl. Catal., A*, 2015, **506**, 25–32.
289 A. W. Hauser, P. R. Horn, M. Head-Gordon and A. T. Bell, *Phys. Chem. Chem. Phys.*, 2016, **18**, 10906–10917.
290 V. J. Cybulskis, B. C. Bukowski, H.-T. Tseng, J. R. Gallagher, Z. Wu, E. Wegener, A. J. Kropf, B. Ravel, F. H. Ribeiro, J. Greeley and J. T. Miller, *ACS Catal.*, 2017, **7**, 4173–4181.
291 J. Ko, J. A. Muhlenkamp, Y. Bonita, N. J. LiBretto, J. T. Miller, J. C. Hicks and W. F. Schneider, *Ind. Eng. Chem. Res.*, 2020, **59**, 12666–12676.
292 J. Wu, Z. Peng and A. T. Bell, *J. Catal.*, 2014, **311**, 161–168.
293 C. Batiot and B. K. Hodnett, *Appl. Catal., A*, 1996, **137**, 179–191.
294 C.-C. Liao, C.-C. Chang, Y. Choi and M.-K. Tsai, *Surf. Sci.*, 2018, **674**, 45–50.
295 G.-L. Dai, Z.-P. Liu, W.-N. Wang, J. Lu and K.-N. Fan, *J. Phys. Chem. C*, 2008, **112**, 3719–3725.
296 D. Melzer, P. Xu, D. Hartmann, Y. Zhu, N. D. Browning, M. Sanchez-Sanchez and J. A. Lercher, *Angew. Chem., Int. Ed.*, 2016, **55**, 8873–8877.
297 V. Fung, F. Tao and D.-E. Jiang, *Catal.: Sci. Technol.*, 2016, **6**, 6861–6869.
298 X. Lin, Y. Xi and J. Sun, *J. Phys. Chem. C*, 2012, **116**, 3503–3516.
299 Y. Bian, M. Kim, T. Li, A. Asthagiri and J. F. Weaver, *J. Am. Chem. Soc.*, 2018, **140**, 2665–2672.
300 M. Banares, M. Martınez-Huerta, X. Gao, J. Fierro and I. Wachs, *Catal. Today*, 2000, **61**, 295–301.
301 J. A. Lercher and F. N. Naraschewski, *Nanostructured Catalysts: Selective Oxidations*, The Royal Society of Chemistry, 2011, pp. 5–32, DOI: 10.1039/9781847559876-00005.
302 M. D. Argyle, K. Chen, A. T. Bell and E. Iglesia, *J. Phys. Chem. B*, 2002, **106**, 5421–5427.
303 H. Fu, Z. P. Liu, Z. H. Li, W. N. Wang and K. N. Fan, *J. Am. Chem. Soc.*, 2006, **128**, 11114–11123.
304 S. P. Sun, J. L. Zhu, S. Gu, X. P. Li, W. N. Lei, Y. Jiang, D. Q. Yi and G. H. Chen, *Appl. Surf. Sci.*, 2019, **467–468**, 753–759.
305 R. Yao, J. E. Herrera, L. Chen and Y.-H. C. Chin, *ACS Catal.*, 2020, **10**, 6952–6968.
306 Y. V. Kolen'ko, W. Zhang, R. N. d'Alnoncourt, F. Girgsdies, T. W. Hansen, T. Wolfram, R. Schlögl and A. Trunschke, *ChemCatChem*, 2011, **3**, 1597–1606.
307 D. Vitry, Y. Morikawa, J. L. Dubois and W. Ueda, *Top. Catal.*, 2003, **23**, 47–53.
308 N. R. Shiju, X. Liang, A. W. Weimer, C. Liang, S. Dai and V. V. Guliants, *J. Am. Chem. Soc.*, 2008, **130**, 5850–5851.
309 A. Celaya Sanfiz, T. W. Hansen, A. Sakthivel, A. Trunschke, R. Schlögl, A. Knoester, H. H. Brongersma, M. H. Looi and S. B. A. Hamid, *J. Catal.*, 2008, **258**, 35–43.
310 R. Schlögl, *Top. Catal.*, 2011, **54**, 627–638.
311 K. Muthukumar, J. Yu, Y. Xu and V. V. Guliants, *Top. Catal.*, 2011, **54**, 605–613.
312 L. Annamalai, Y. Liu, S. Ezenwa, Y. Dang, S. L. Suib and P. Deshlahra, *ACS Catal.*, 2018, **8**, 7051–7067.
313 Y. Liu, L. Annamalai and P. Deshlahra, *J. Phys. Chem. C*, 2019, **123**, 28168–28191.
314 S. Zhang, J.-j. Shan, Y. Zhu, A. I. Frenkel, A. Patlolla, W. Huang, S. J. Yoon, L. Wang, H. Yoshida, S. Takeda and F. Tao, *J. Am. Chem. Soc.*, 2013, **135**, 8283–8293.
315 D.-e. Jiang and S. Dai, *Phys. Chem. Chem. Phys.*, 2011, **13**, 978–984.
316 V. Fung, F. Tao and D. E. Jiang, *ChemCatChem*, 2018, **10**, 244–249.
317 H. Zhu, D. C. Rosenfeld, M. Harb, D. H. Anjum, M. N. Hedhili, S. Ould-Chikh and J.-M. Basset, *ACS Catal.*, 2016, **6**, 2852–2866.
318 X. Sun, B. Li and H. Metiu, *J. Phys. Chem. C*, 2013, **117**, 23597–23608.
319 B. Savova, S. Loridant, D. Filkova and J. Millet, *Appl. Catal., A*, 2010, **390**, 148–157.
320 H. Zhu, S. Ould-Chikh, D. H. Anjum, M. Sun, G. Biausque, J.-M. Basset and V. Caps, *J. Catal.*, 2012, **285**, 292–303.
321 T. L. M. Pham, S. Nachimuthu, J.-L. Kuo and J.-C. Jiang, *Appl. Catal., A*, 2017, **541**, 8–14.

322 T. A. Bugrova, V. V. Dutov, V. A. Svetlichnyi, V. Cortés Corberán and G. V. Mamontov, *Catal. Today*, 2019, **333**, 71–80.
323 M. Myint, B. Yan, J. Wan, S. Zhao and J. G. Chen, *J. Catal.*, 2016, **343**, 168–177.
324 B. Yan, S. Yao, S. Kattel, Q. Wu, Z. Xie, E. Gomez, P. Liu, D. Su and J. G. Chen, *Proc. Natl. Acad. Sci. U. S. A.*, 2018, **115**, 8278–8283.
325 M. D. Porosoff, M. N. Z. Myint, S. Kattel, Z. Xie, E. Gomez, P. Liu and J. G. Chen, *Angew. Chem.*, 2015, **127**, 15721–15725.
326 S. Yao, B. Yan, Z. Jiang, Z. Liu, Q. Wu, J. H. Lee and J. G. Chen, *ACS Catal.*, 2018, **8**, 5374–5381.
327 E. Gomez, S. Kattel, B. Yan, S. Yao, P. Liu and J. G. Chen, *Nat. Commun.*, 2018, **9**, 1398–1403.
328 F. Jalid, T. S. Khan and M. A. Haider, *Catal.: Sci. Technol.*, 2021, **11**, 97–115.
329 O. O. James, S. Mandal, N. Alele, B. Chowdhury and S. Maity, *Fuel Process. Technol.*, 2016, **149**, 239–255.
330 Y. He, Y. J. Song, D. A. Cullen and S. Laursen, *J. Am. Chem. Soc.*, 2018, **140**, 14010–14014.
331 L. Xiao, F. Ma, Y.-A. Zhu, Z.-J. Sui, J.-H. Zhou, X.-G. Zhou, D. Chen and W.-K. Yuan, *Chem. Eng. J.*, 2019, **377**, 120049.
332 J. Im and M. Choi, *ACS Catal.*, 2016, **6**, 2819–2826.
333 J. J. H. B. Sattler, I. D. Gonzalez-Jimenez, L. Luo, B. A. Stears, A. Malek, D. G. Barton, B. A. Kilos, M. P. Kaminsky, T. W. G. M. Verhoeven, E. J. Koers, M. Baldus and B. M. Weckhuysen, *Angew. Chem., Int. Ed.*, 2014, **53**, 9251–9256.
334 N. Kaylor and R. J. Davis, *J. Catal.*, 2018, **367**, 181–193.
335 R. Grabowski and J. Słoczyński, *Chem. Eng. Process.*, 2005, **44**, 1082–1093.
336 M. M. Hossain, *Ind. Eng. Chem. Res.*, 2017, **56**, 4309–4318.
337 J. Baek, H. J. Yun, D. Yun, Y. Choi and J. Yi, *ACS Catal.*, 2012, **2**, 1893–1903.
338 F. Cavani, N. Ballarini and A. Cericola, *Catal. Today*, 2007, **127**, 113–131.
339 K. Chen, A. T. Bell and E. Iglesia, *J. Phys. Chem. B*, 2000, **104**, 1292–1299.
340 S. Saerens, M. K. Sabbe, V. V. Galvita, E. A. Redekop, M.-F. Reyniers and G. B. Marin, *ACS Catal.*, 2017, **7**, 7495–7508.
341 Y. J. Wang, Y. M. Wang, S. R. Wang, X. Z. Guo, S. M. Zhang, W. P. Huang and S. H. Wu, *Catal. Lett.*, 2009, **132**, 472–479.
342 A. Iglesias-Juez, A. M. Beale, K. Maaijen, T. C. Weng, P. Glatzel and B. M. Weckhuysen, *J. Catal.*, 2010, **276**, 268–279.
343 P. Sun, G. Siddiqi, W. C. Vining, M. Chi and A. T. Bell, *J. Catal.*, 2011, **282**, 165–174.
344 J. C. Li, J. M. Li, Z. Zhao, X. Q. Fan, J. Liu, Y. C. Wei, A. J. Duan, Z. Xie and Q. L. Liu, *J. Catal.*, 2017, **352**, 361–370.
345 S. Zha, G. Sun, T. Wu, J. Zhao, Z.-J. Zhao and J. Gong, *Chem. Sci.*, 2018, **9**, 3925–3931.
346 C. Yang, Z. Wu, G. Zhang, H. Sheng, J. Tian, Z. Duan, H. Sohn, A. J. Kropf, T. Wu, T. R. Krause and J. T. Miller, *Catal. Today*, 2019, **323**, 123–128.
347 M.-L. Yang, Y.-A. Zhu, C. Fan, Z.-J. Sui, D. Chen and X.-G. Zhou, *Phys. Chem. Chem. Phys.*, 2011, **13**, 3257–3267.
348 M.-L. Yang, Y.-A. Zhu, X.-G. Zhou, Z.-J. Sui and D. Chen, *ACS Catal.*, 2012, **2**, 1247–1258.
349 M.-L. Yang, Y.-A. Zhu, C. Fan, Z.-J. Sui, D. Chen and X.-G. Zhou, *J. Mol. Catal. A: Chem.*, 2010, **321**, 42–49.
350 L. Nykänen and K. Honkala, *J. Phys. Chem. C*, 2011, **115**, 9578–9586.
351 T. Saelee, S. Namuangruk, N. Kungwan and A. Junkaew, *J. Phys. Chem. C*, 2018, **122**, 14678–14690.
352 X. Cao, *RSC Adv.*, 2016, **6**, 65524–65532.
353 Z. Lian, S. Ali, T. Liu, C. Si, B. Li and D. S. Su, *ACS Catal.*, 2018, **8**, 4694–4704.
354 J. Zhu, M.-L. Yang, Y. Yu, Y.-A. Zhu, Z. J. Sui, X. Zhou, A. Holmen and D. Chen, *ACS Catal.*, 2015, **5**, 6310–6319.
355 Z.-J. Sui, Y.-A. Zhu, P. Li, X.-G. Zhou and D. Chen, in *Advances in Chemical Engineering*, ed. G. B. Marin, Academic Press, 2014, vol. 44, pp. 61–125.
356 A. Valcárcel, J. M. Ricart, A. Clotet, A. Markovits, C. Minot and F. Illas, *Surf. Sci.*, 2002, **519**, 250–258.
357 M.-L. Yang, J. Zhu, Y.-A. Zhu, Z.-J. Sui, Y.-D. Yu, X.-G. Zhou and D. Chen, *J. Mol. Catal., A*, 2014, **395**, 329–336.
358 F. Ma, Q.-Y. Chang, Q. Yin, Z.-J. Sui, X.-G. Zhou, D. Chen and Y.-A. Zhu, *Catal.: Sci. Technol.*, 2020, **10**, 4938–4951.
359 A. Valcárcel, J. M. Ricart, A. Clotet, F. Illas, A. Markovits and C. Minot, *J. Catal.*, 2006, **241**, 115–122.
360 A. Valcárcel, A. Gil, J. M. Ricart and A. Clotet, *Chem. Phys. Lett.*, 2004, **399**, 295–299.
361 L. Shi, G. M. Deng, W. C. Li, S. Miao, Q. N. Wang, W. P. Zhang and A. H. Lu, *Angew. Chem., Int. Ed.*, 2015, **54**, 13994–13998.
362 L. Rochlitz, K. Searles, J. Alfke, D. Zemlyanov, O. V. Safonova and C. Copéret, *Chem. Sci.*, 2020, **11**, 1549–1555.
363 J. R. Gallagher, D. J. Childers, H. Zhao, R. E. Winans, R. J. Meyer and J. T. Miller, *Phys. Chem. Chem. Phys.*, 2015, **17**, 28144–28153.
364 X. Cao, Y. Ji and Y. Luo, *J. Phys. Chem. C*, 2015, **119**, 1016–1023.
365 L. Xiao, Y.-L. Shan, Z.-J. Sui, D. Chen, X.-G. Zhou, W.-K. Yuan and Y.-A. Zhu, *ACS Catal.*, 2020, **10**, 14887–14902.
366 M. Heinritz-Adrian, S. Wenzel and F. Youssef, *Pet. Technol. Quart.*, 2008, **13**, 83–92.
367 Y. Zhu, Z. An, H. Song, X. Xiang, W. Yan and J. He, *ACS Catal.*, 2017, **7**, 6973–6978.
368 C.-c. Chiu, A. Genest and N. Rösch, *ChemCatChem*, 2013, **5**, 3299–3308.
369 M.-L. Yang, C. Fan, Y.-A. Zhu, Z.-J. Sui, X.-G. Zhou and D. Chen, *J. Phys. Chem. C*, 2015, **119**, 21386–21394.
370 L. G. Cesar, C. Yang, Z. Lu, Y. Ren, G. Zhang and J. T. Miller, *ACS Catal.*, 2019, **9**, 5231–5244.
371 M. S. Kumar, D. Chen, J. C. Walmsley and A. Holmen, *Catal. Commun.*, 2008, **9**, 747–750.
372 T. Bauer, S. Maisel, D. Blaumeiser, J. Vecchietti, N. Taccardi, P. Wasserscheid, A. Bonivardi, A. Gorling and J. Libuda, *ACS Catal.*, 2019, **9**, 2842–2853.
373 O. A. Bariås, A. Holmen and E. A. Blekkan, *J. Catal.*, 1996, **158**, 1–12.

374 Z. Han, S. Li, F. Jiang, T. Wang, X. Ma and J. Gong, *Nanoscale*, 2014, **6**, 10000–10008.
375 K. Xia, W.-Z. Lang, P.-P. Li, X. Yan and Y.-J. Guo, *J. Catal.*, 2016, **338**, 104–114.
376 T. Wang, F. Jiang, G. Liu, L. Zeng, Z. J. Zhao and J. Gong, *AIChE J.*, 2016, **62**, 4365–4376.
377 S. Furukawa and T. Komatsu, *ACS Catal.*, 2016, **7**, 735–765.
378 B. Hammer and J. K. Nørskov, *Adv. Catal.*, 2000, **45**, 71–129.
379 L. Nykänen and K. Honkala, *ACS Catal.*, 2013, **3**, 3026–3030.
380 M.-H. Lee, B. M. Nagaraja, P. Natarajan, N. T. Truong, K. Y. Lee, S. Yoon and K.-D. Jung, *Res. Chem. Intermed.*, 2016, **42**, 123–140.
381 H. N. Pham, J. J. H. B. Sattler, B. M. Weckhuysen and A. K. Datye, *ACS Catal.*, 2016, **6**, 2257–2264.
382 Z. Li, L. Yu, C. Milligan, T. Ma, L. Zhou, Y. Cui, Z. Qi, N. Libretto, B. Xu, J. Luo, E. Shi, Z. Wu, H. Xin, W. N. Delgass, J. T. Miller and Y. Wu, *Nat. Commun.*, 2018, **9**, 5258–5265.
383 B. K. Vu, M. B. Song, I. Y. Ahn, Y.-W. Suh, D. J. Suh, J. S. Kim and E. W. Shin, *J. Ind. Eng. Chem.*, 2011, **17**, 71–76.
384 Y. Zhang, M. Xue, Y. Zhou, H. Zhang, W. Wang, Q. Wang and X. Sheng, *RSC Adv.*, 2016, **6**, 29410–29422.
385 G. Sun, Z.-J. Zhao, R. Mu, S. Zha, L. Li, S. Chen, K. Zang, J. Luo, Z. Li, S. C. Purdy, A. J. Kropf, J. T. Miller, L. Zeng and J. Gong, *Nat. Commun.*, 2018, **9**, 4454.
386 C. C. Chang, C. Y. Liu, S. Y. Wu and M. K. Tsai, *Phys. Chem. Chem. Phys.*, 2017, **19**, 4989–4996.
387 K. Xia, W.-Z. Lang, P.-P. Li, L.-L. Long, X. Yan and Y.-J. Guo, *Chem. Eng. J.*, 2016, **284**, 1068–1079.
388 J. Liu, Y. Yue, H. Liu, Z. Da, C. Liu, A. Ma, J. Rong, D. Su, X. Bao and H. Zheng, *ACS Catal.*, 2017, **7**, 3349–3355.
389 F. Jiang, L. Zeng, S. Li, G. Liu, S. Wang and J. Gong, *ACS Catal.*, 2015, **5**, 438–447.
390 M. M. Bhasin, J. H. McCain, B. V. Vora, T. Imai and P. R. Pujado, *Appl. Catal., A*, 2001, **221**, 397–419.
391 J. Zhang, R.-J. Zhou, Q.-Y. Chang, Z.-J. Sui, X.-G. Zhou, D. Chen and Y.-A. Zhu, *Catal. Today*, 2020, DOI: 10.1016/j.cattod.2020.02.023.
392 C. Coperet, *Chem. Rev.*, 2010, **110**, 656–680.
393 J. Védrine, *Catalysts*, 2017, **7**, 341–365.
394 G. Liu, Z. J. Zhao, T. F. Wu, L. Zeng and J. L. Gong, *ACS Catal.*, 2016, **6**, 5207–5214.
395 A. H. Elbadawi, M. S. Ba-Shammakh, S. Al-Ghamdi, S. A. Razzak and M. M. Hossain, *Chem. Eng. J.*, 2016, **284**, 448–457.
396 S. Barman, N. Maity, K. Bhatte, S. Ould-Chikh, O. Dachwald, C. Haeßner, Y. Saih, E. Abou-Hamad, I. Llorens, J.-L. Hazemann, K. Köhler, V. D' Elia and J.-M. Basset, *ACS Catal.*, 2016, **6**, 5908–5921.
397 Y. Gambo, A. A. Jalil, S. Triwahyono and A. A. Abdulrasheed, *J. Ind. Eng. Chem.*, 2018, **59**, 218–229.
398 P. Gandeepan, T. Müller, D. Zell, G. Cera, S. Warratz and L. Ackermann, *Chem. Rev.*, 2019, **119**, 2192–2452.
399 F. Gilardoni, A. T. Bell, A. Chakraborty and P. Boulet, *J. Phys. Chem. B*, 2000, **104**, 12250–12255.
400 G. Fu, X. Xu, X. Lu and H. Wan, *J. Phys. Chem. B*, 2005, **109**, 6416–6421.
401 R. m. F. Xavier Rozanska and J. Sauer, *J. Phys. Chem. C*, 2007, **111**, 6041–6050.
402 Y. Liu, Z. H. Li, J. Lu and K. N. Fan, *J. Phys. Chem. C*, 2008, **112**, 20382–20392.
403 K. Alexopoulos, M.-F. Reyniers and G. B. Marin, *J. Catal.*, 2012, **289**, 127–139.
404 C. Xiong, S. Chen, P. Yang, S. Zha, Z.-J. Zhao and J. Gong, *ACS Catal.*, 2019, **9**, 5816–5827.
405 Q.-Y. Chang, Q. Yin, F. Ma, Y.-A. Zhu, Z.-J. Sui, X.-G. Zhou, D. Chen and W.-K. Yuan, *Ind. Eng. Chem. Res.*, 2019, **58**, 10199–10209.
406 M. Hus, D. Kopac and B. Likozar, *J. Catal.*, 2020, **386**, 126–138.
407 A. Kämper, A. Auroux and M. Baerns, *Phys. Chem. Chem. Phys.*, 2000, **2**, 1069–1075.
408 M. V. Ganduglia-Pirovano and J. Sauer, *J. Phys. Chem. B*, 2005, **109**, 374–380.
409 P. C. Redfern, P. Zapol, M. Sternberg, S. P. Adiga, S. A. Zygmunt and L. A. Curtiss, *J. Phys. Chem. B*, 2006, **110**, 8363–8371.
410 M. Engeser, M. Schlangen, D. Schröder, H. Schwarz, T. Yumura and K. Yoshizawa, *Organometallics*, 2003, **22**, 3933–3943.
411 S. Feyel, D. Schroder, X. Rozanska, J. Sauer and H. Schwarz, *Angew. Chem., Int. Ed.*, 2006, **45**, 4677–4681.
412 J. Scholz, A. Walter and T. Ressler, *J. Catal.*, 2014, **309**, 105–114.
413 J. Gong, *Angew. Chem., Int. Ed.*, 2020, **59**, 22072–22079.
414 Y.-J. Du, Z. H. Li and K.-N. Fan, *J. Mol. Catal., A*, 2013, **379**, 122–138.
415 X. Rozanska, R. Fortrie and J. Sauer, *J. Am. Chem. Soc.*, 2014, **136**, 7751–7761.
416 J.-L. Sánchez-García, B. E. Handy, I. N. Ávila-Hernández, A. G. Rodríguez and R. García-Alamilla, *Catalysts*, 2020, **10**, 550.
417 H. Kazerooni, J. T. Darian, Y. Mortazavi, A. A. Khadadadi and R. Asadi, *Catal. Lett.*, 2020, **150**, 2807–2822.
418 X. Wu, Z. Chen, X. Yu, Z. Huang, H. Shen and G. Jing, *Chem. Eng. J.*, 2020, 125629.
419 Q.-X. Luo, X.-K. Zhang, B.-L. Hou, J.-G. Chen, C. Zhu, Z.-W. Liu, Z.-T. Liu and J. Lu, *Catal.: Sci. Technol.*, 2018, **8**, 4864–4876.
420 L. Cheng, G. A. Ferguson, S. A. Zygmunt and L. A. Curtiss, *J. Catal.*, 2013, **302**, 31–36.
421 Y. Hinuma, T. Toyao, T. Kamachi, Z. Maeno, S. Takakusagi, S. Furukawa, I. Takigawa and K.-I. Shimizu, *J. Phys. Chem. C*, 2018, **122**, 29435–29444.
422 Y. Li, W. Cheng, Z.-J. Sui, X.-G. Zhou, D. Chen, W.-K. Yuan and Y.-A. Zhu, *J. Phys. Chem. C*, 2019, **123**, 28275–28283.
423 J. Sauer and J. Dobler, *Dalton Trans.*, 2004, 3116–3121, DOI: 10.1039/b402873b.
424 G.-L. Dai, Z.-H. Li, J. Lu, W.-N. Wang and K.-N. Fan, *J. Phys. Chem. C*, 2012, **116**, 807–817.
425 H.-S. Kim, S. A. Zygmunt, P. C. Stair, P. Zapol and L. A. Curtiss, *J. Phys. Chem. C*, 2009, **113**, 8836–8843.
426 Y. Y. Zhang, Y. Zhao, T. Otroshchenko, H. Lund, M. M. Pohl, U. Rodemerck, D. Linke, H. J. Jiao, G. Y. Jiang and E. V. Kondratenko, *Nat. Commun.*, 2018, **9**, 3794–3803.

427 K. Chen, A. Khodakov, J. Yang, A. T. Bell and E. Iglesia, *J. Catal.*, 1999, **186**, 325–333.
428 K. Chen, E. Iglesia and A. T. Bell, *J. Phys. Chem. B*, 2001, **105**, 646–653.
429 S. Chakraborty, S. C. Nayak and G. Deo, *Catal. Today*, 2015, **254**, 62–71.
430 M. De and D. Kunzru, *Catal. Lett.*, 2005, **102**, 237–246.
431 S. N. Koc, G. Gurdag, S. Geissler, M. Guraya, M. Orbay and M. Muhler, *J. Mol. Catal., A*, 2005, **225**, 197–202.
432 A. Held, J. Kowalska-Kuś, K. Nowińska and K. Góra-Marek, *J. Catal.*, 2017, **347**, 21–35.
433 Z.-J. Zhao, T. Wu, C. Xiong, G. Sun, R. Mu, L. Zeng and J. Gong, *Angew. Chem., Int. Ed.*, 2018, **57**, 6791–6795.
434 Z. Bai, P. Li, L. Liu and G. Xiong, *ChemCatChem*, 2012, **4**, 260–264.
435 G. Wu, F. Hei, N. Guan and L. Li, *Catal.: Sci. Technol.*, 2013, **3**, 1333.
436 M. J. Cheng and W. A. Goddard, 3rd, *J. Am. Chem. Soc.*, 2015, **137**, 13224–13227.
437 M. Aly, E. L. Fornero, A. R. Leon-Garzon, V. V. Galvita and M. Saeys, *ACS Catal.*, 2020, **10**, 5208–5216.
438 K. Chen, A. T. Bell and E. Iglesia, *J. Catal.*, 2002, **209**, 35–42.
439 Q.-Y. Chang, K.-Q. Wang, P. Hu, Z.-J. Sui, X.-G. Zhou, D. Chen, W.-K. Yuan and Y.-A. Zhu, *AIChE J.*, 2020, **66**, 16232.
440 T. Shishido, K. Shimamura, K. Teramura and T. Tanaka, *Catal. Today*, 2012, **185**, 151–156.
441 H. M. Wang, Y. Chen, X. Yan, W. Z. Lang and Y. J. Guo, *Microporous Mesoporous Mater.*, 2019, **284**, 69–77.
442 M. A. Atanga, F. Rezaei, A. Jawad, M. Fitch and A. A. Rownaghi, *Appl. Catal., B*, 2018, **220**, 429–445.
443 L. Wang, L. Huang, F. Liang, S. Liu, Y. Wang and H. Zhang, *Chin. J. Catal.*, 2017, **38**, 1528–1539.
444 J. Y. Liu, *ACS Catal.*, 2017, **7**, 34–59.
445 N. J. O'Connor, A. S. M. Jonayat, M. J. Janik and T. P. Senftle, *Nat. Catal.*, 2018, **1**, 531–539.
446 X. F. Yang, A. Wang, B. Qiao, J. Li, J. Liu and T. Zhang, *Acc. Chem. Res.*, 2013, **46**, 1740–1748.
447 X.-K. Gu, B. Qiao, C.-Q. Huang, W.-C. Ding, K. Sun, E. Zhan, T. Zhang, J. Liu and W.-X. Li, *ACS Catal.*, 2014, **4**, 3886–3890.
448 C. Riley, S. Zhou, D. Kunwar, A. De La Riva, E. Peterson, R. Payne, L. Gao, S. Lin, H. Guo and A. Datye, *J. Am. Chem. Soc.*, 2018, **140**, 12964–12973.
449 Z. K. Han and Y. Gao, *Chem. – Eur. J.*, 2016, **22**, 2092–2099.
450 R. Lang, W. Xi, J. C. Liu, Y. T. Cui, T. Li, A. F. Lee, F. Chen, Y. Chen, L. Li, L. Li, J. Lin, S. Miao, X. Liu, A. Q. Wang, X. Wang, J. Luo, B. Qiao, J. Li and T. Zhang, *Nat. Commun.*, 2019, **10**, 234.
451 H. Xiong, S. Lin, J. Goetze, P. Pletcher, H. Guo, L. Kovarik, K. Artyushkova, B. M. Weckhuysen and A. K. Datye, *Angew. Chem., Int. Ed.*, 2017, **56**, 8986–8991.
452 X. Sun, P. Han, B. Li and Z. Zhao, *J. Phys. Chem. C*, 2018, **122**, 1570–1576.
453 X. Y. Sun, M. J. Liu, Y. Y. Huang, B. Li and Z. Zhao, *Chin. J. Catal.*, 2019, **40**, 819–825.
454 N. Kong, X. Fan, F. Liu, L. Wang, H. Lin, Y. Li and S.-T. Lee, *ACS Nano*, 2020, **14**, 5772–5779.
455 W. Zhang, H. Wang, J. Jiang, Z. Sui, Y. Zhu, D. Chen and X. Zhou, *ACS Catal.*, 2020, **10**, 12932–12942.
456 G. Liu, L. Zeng, Z.-J. Zhao, H. Tian, T. Wu and J. Gong, *ACS Catal.*, 2016, **6**, 2158–2162.
457 J. K. Nørskov, F. Studt, F. Abild-Pedersen and T. Bligaard, *Fundamental concepts in heterogeneous catalysis*, John Wiley & Sons, 2014.
458 B. Hammer and J. K. Norskov, *Nature*, 1995, **376**, 238–240.

